Solutions for Cell and Gene Therapy

PerkinElmer®
For the Better

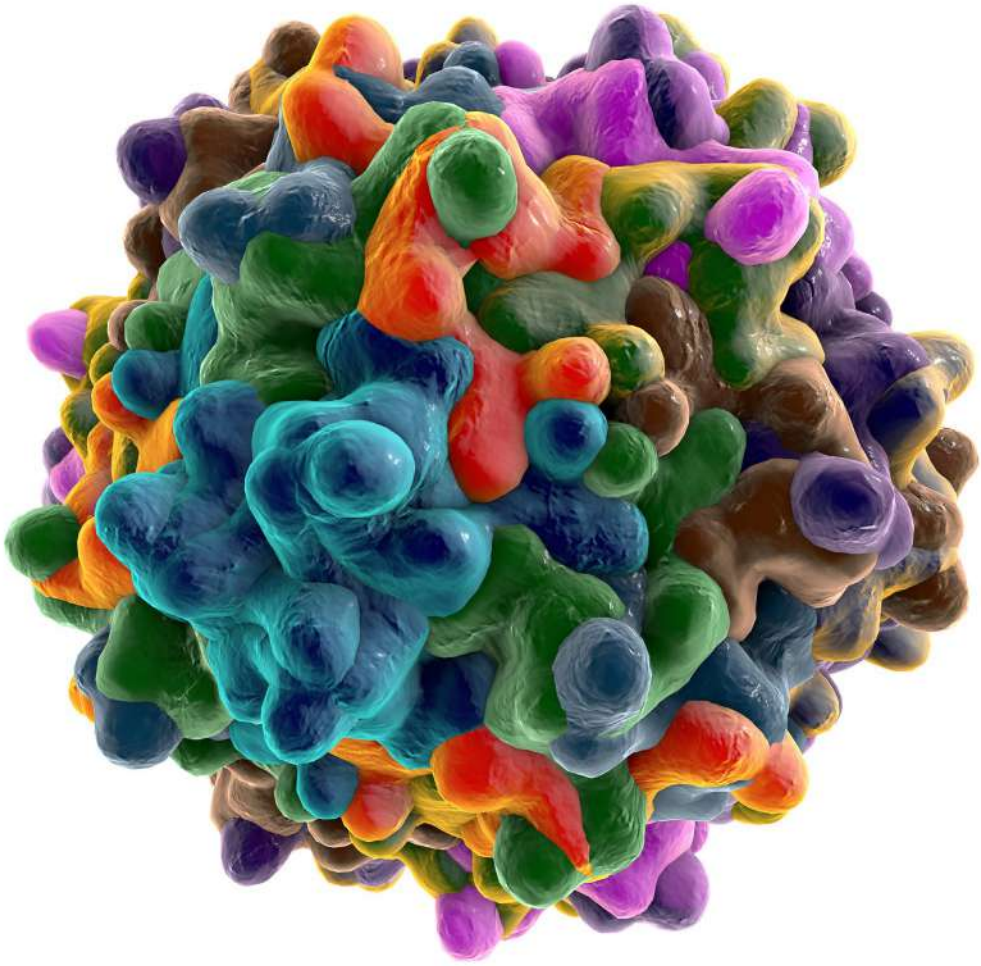

INTRODUCTION

We are excited to spotlight a collection of application notes wherein we demonstrate how we have supported scientists in the early phase of their cellular and gene therapy discovery. The collection focuses on how we can quickly analyze cellular images through machine assisted learning and characterize, profile and test for efficacy of the delivery vehicle and transgene using our latest technologies.

TABLE OF CONTENTS

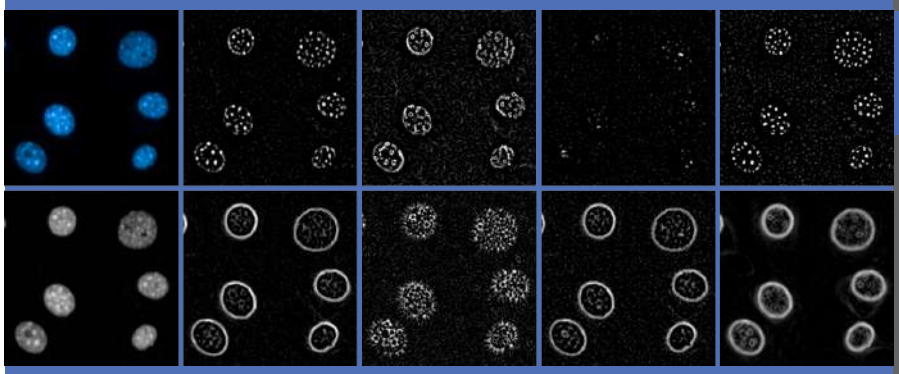

APPLICATION NOTE

High-Content Screening

Authors:

Alexander Schreiner
Mandy Malle
Karin Böttcher

PerkinElmer, Inc.
Hamburg, Germany

Distinguishing Cell Types by Phenotypic Profiling of the Nucleus

Key Points:

- Distinguish cell types based exclusively on nuclear staining
- Generate detailed phenotypic profiles using texture and advanced morphology parameters
- Leverage easy to use supervised machine learning tools to accurately classify cell types in co-cultures
- See how texture and advanced morphology parameters feed into Principal Component Analyses for separating more complex data sets

Introduction

The promise of high-content screening is the acceleration of discovery by extracting as much relevant information as possible from cells. Nevertheless, a large percentage of high-content screens analyze only a small number of image-based properties.[1] As a result, valuable information from precious cells and disease models is not utilized. As nearly all screening approaches require a nuclear counterstain such as Hoechst to facilitate segmentation, phenotypic profiling of the nuclei can offer new and additional perspectives on assays at no extra cost. Hoechst "total sum intensity" distribution is sometimes used to analyze cell cycle distribution, in particular G0/G1, S and G2/M populations. However, besides cell cycle analysis, more information can be retrieved from the nuclear "counterstain". Using Harmony® high-content imaging and analysis software, this study shows how a single nuclear stain enables phenotypic profiling and how phenotypic profiles can be used to distinguish cell types within co-cultures or even within seven different cell types without any further staining or additional phenotypic markers.

For research use only. Not for use in diagnostic procedures.

PerkinElmer® For the Better

Co-cultured Cells Can Be Distinguished Based on Hoechst Nucleus Staining Only

To maintain primary cells *in vitro,* they are often co-cultured with other cells which provide pro-survival signals in the form of trophic factors and cell-cell interactions. Typical examples are primary hepatocytes co-cultured with fibroblasts or primary neurons co-cultured with astrocytes. Besides this, co-cultures are also used to study the interaction between cell types, e.g. cancer cells with tumor-derived fibroblasts, or epithelial cells with lymphocytes. In the typical direct co-culture setup, cell types are mixed within the same well, posing challenges to analyze them separately. To show how nuclear counterstaining, which is normally only used for cell segmentation, can also be used for cell classification, human hepatocytes (HepG2) and mouse fibroblasts (NIH/3T3) were co-cultured and analyzed.

Application

HepG2 liver and NIH/3T3 fibroblast cells were seeded into a CellCarrier-384 Ultra microplate (PerkinElmer, # 6057300) either alone or as co-culture at different ratios (2:1, 1:1, 1:2). Prior to mixing, HepG2 cells were stained with CellTracker Green CMFDA (Thermofisher, # C2925) and NIH/3T3 cells with CellTracker Red CMTPX (Thermofisher, # C34552) to enable validation of the accuracy of the phenotypic classification. For each individual cell type, 96 wells, and for each co-culture condition, 64 wells, were used. The next day, the cells were fixed, stained with Hoechst 33342 (Thermofisher, # H3570) and single plane images were acquired on an Opera Phenix™ high-content screening system using a 20x water immersion objective in confocal mode. A total of 9 fields per well were acquired corresponding to approximately 1100 cells. Figure 1 shows example images of individual cultures and co-cultures.

Image Analysis

To classify individual cells based on Hoechst nuclear staining as either HepG2 or NIH/3T3, images were analyzed using Harmony software. As a first step, nuclei were segmented using the *Find Nuclei* building block and basic morphology (i.e. area, roundness, width, length) and intensity (i.e. mean, max, sum) properties were calculated using the *Calculate Morphology Properties* and *Calculate Intensity Properties* building blocks. Border objects were removed using the *Select Population* building block which was followed by another *Select Population* building block to remove mitotic cells based on the previous calculated morphology and intensity properties. Mitotic cells were eliminated from further analysis based on the assumption that these nuclei should have less distinctive texture features than G0/G1, S and G2 nuclei. To calculate detailed phenotypic profiles, SER texture (Spots, Edges and Ridges) and advanced STAR morphology (Symmetry, Threshold compactness, Axial or Radial) parameters were calculated using *Calculate Texture Properties* and *Calculate Morphology Properties* building blocks. SER texture quantifies the occurrence of eight characteristic intensity patterns such as spots, edges and ridges within the image (see Figure 2 for visualizations). To capture texture structures with different sizes, three independent *Calculate Texture Properties* building blocks were used with different settings for the scale parameter (0, 1 and 2px). STAR morphology parameters are a set of properties that quantify the distribution of either texture features or fluorescence intensities inside a region of interest. They also include profiles in which the distribution of texture features or fluorescence intensity distributions are weighted depending on their localization inside the region of interest. In the case of the nuclear analysis used here, two profiles exist. Profile 1/2 starts at the nuclear membrane and weighting factors decrease towards the nuclear center. This parameter is very sensitive to phenotypic

GLOSSARY OF TERMS

Phenotype: The collection of observable traits of an organism, e.g. at the minimal level of a cell, properties such as size, shape or molecular content. Due to interaction and alteration with, or of the environment, these characteristics can change, e.g. cells passing through cell cycle.

Phenotypic Marker: A marker that allows the identification of a specific phenotype, e.g. phospho-histone H3 is a marker for mitotic cells.

Phenotypic Profiling: Extraction of a large number of quantitative features from microscopy images of cells to identify biologically relevant similarities or differences among samples based on these profiles.[2]

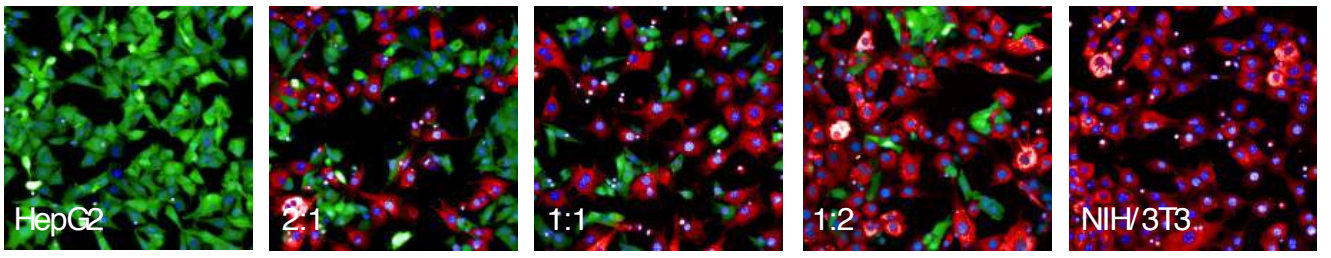

Figure 1. Representative images from wells containing either HepG2 or NIH/3T3 alone or co-cultures of HepG2 and NIH/3T3 cells mixed at ratios 2:1, 1:1 and 1:2 respectively. HepG2 cells are stained with Hoechst 33342 and CellTracker Green CMFDA. NIH/3T3 cells are stained with Hoechst 33342 and CellTracker Red CMTPX. Images were acquired on the Opera Phenix system in confocal mode using a 20x water immersion objective.

changes within this outer region of the nucleus. Profile 2/2 has the highest weight factor in the nuclear center and decreases towards the nuclear membrane. Therefore, this parameter sensitively captures changes within the inner region of the nucleus. STAR morphology properties also include a sliding parabola filter that can be used to remove smooth and continuous background from the image. Example images showing profiles, SER texture and sliding parabola filtered images of NIH/3T3 nuclei are shown in Figure 2.

Using PhenoLOGIC Machine-learning to Select the Best Parameters for Distinguishing Cell Types

A total of 230 parameters were calculated for every nucleus. The PhenoLOGIC machine-learning option in Harmony was then used to select the parameters best suited to discriminate between the two cell types. PhenoLOGIC requires the user to supervise training by simply clicking on about 100 representative objects per class to train the software to distinguish different phenotypes (Figure 3). After training, the software performs a linear discriminant analysis (LDA)[3] to create a linear combination of the most relevant parameters that is then applied to untrained sample wells to classify cells either as HepG2 or NIH/3T3.

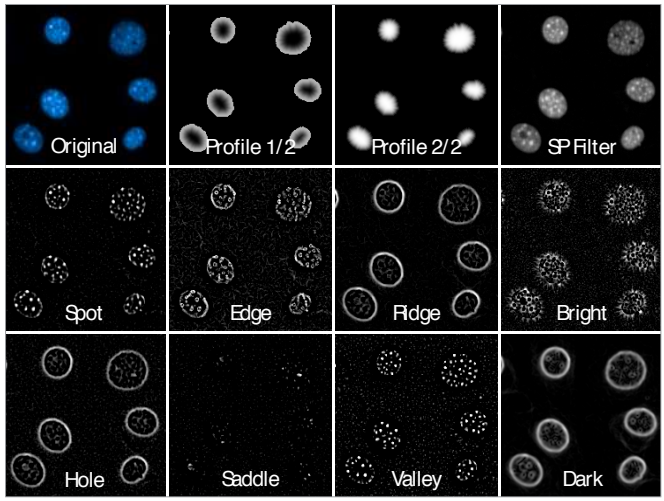

Figure 2. SER texture and STAR morphology properties are key parameters for phenotypic profiling within Harmony software. Original input image, profile images (Profile 1/2 and Profile 2/2), sliding parabola filtered (SP Filter) image and SER texture filtered (Spot, Edge, Ridge, Bright, Hole, Saddle, Valley and Dark) images of the same NIH/3T3 nuclei.

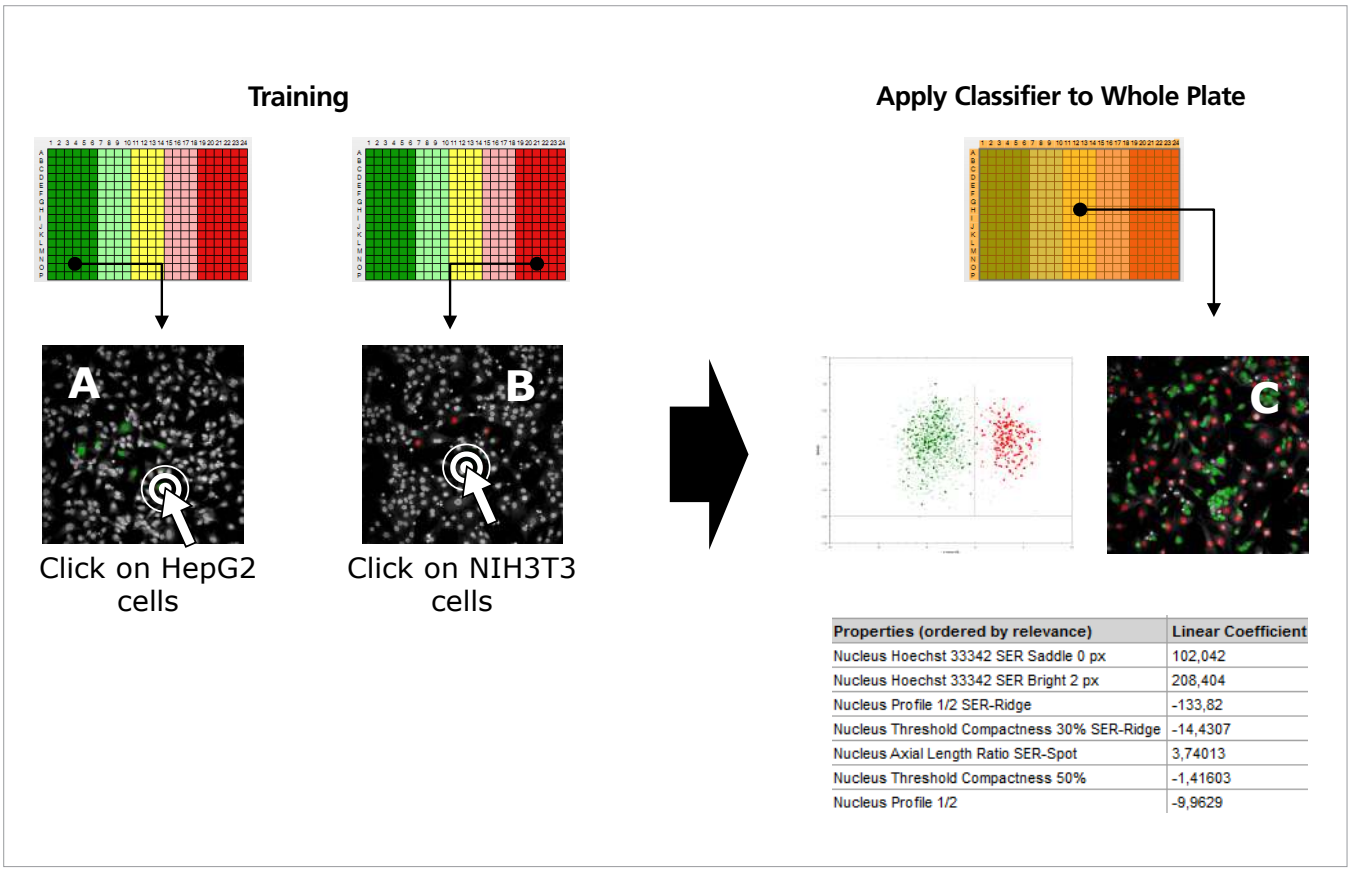

Properties (ordered by relevance)	Linear Coefficient
Nucleus Hoechst 33342 SER Saddle 0 px	102,042
Nucleus Hoechst 33342 SER Bright 2 px	208,404
Nucleus Profile 1/2 SER-Ridge	-133,82
Nucleus Threshold Compactness 30% SER-Ridge	-14,4307
Nucleus Axial Length Ratio SER-Spot	3,74013
Nucleus Threshold Compactness 50%	-1,41603
Nucleus Profile 1/2	-9,9629

Figure 3. Identifying cellular phenotypes using PhenoLOGIC machine learning. In "Training" mode, about 100 single cells within different wells were selected to teach the software to identify the different cell types in "mono cultures" (A and B). Once cells for each class were marked, the resulting classifier was applied to the whole data set. PhenoLOGIC combines the most meaningful parameters, to achieve accurate classification of the two cell types (panel C). In this case, seven properties were chosen to distinguish HepG2 from NIH/3T3 (properties shown in table below the scatter plot). Note how advanced SER (first 2) and STAR (position 3 to 7) properties dominate the selection.

To check the accuracy of the classification, the CellTracker intensity in a perinuclear region was calculated. If a cell was classified as one cell type but the respective CellTracker intensity was below a defined threshold, the cell was counted as a "falsely classified" cell. For this purpose, it was important to calculate CellTracker intensities after the PhenoLOGIC *Select Population* building block to avoid including this information in the classifier.

In mono cultures, 97.5 – 97.8% of the cells are classified correctly. Incorrectly classified cells, i.e. NIH/3T3 in pure HepG2 cultures are identified as false positive based on the CellTracker staining (Figure 4C, first red and light red column on the left). In addition a negligible number of HepG2 cells (0.01%, Figure 4B, first light green column on the left) is identified as false positive in pure HepG2 cultures. These represent cells that did not take up sufficient CellTracker during staining. The same is true for HepG2 cells identified in pure NIH/3T3 cells. All falsely classified cells are identified by CellTracker staining (Figure 4B, last green and light green columns on the right) and a very low and negligible number of NIH/3T3 cells (0.01%, Figure 4C, last light red column on the right) are identified as false positives based on the insufficient CellTracker staining. The percentage of falsely classified cells decreases in the co-cultures. In a 1:1 co-culture, the percentage of false positives drops to 0.34 – 0.65% of all cells (Figure 4). This verification clearly shows that the advanced texture and STAR morphology properties, together with the PhenoLOGIC™ machine learning option, all built-in to Harmony high-content imaging and analysis software, allow the phenotypic differentiation of cell types in co-cultures based on Hoechst nuclear staining alone.

Phenotypic Profiling of the Nucleus Allows Distinguishing of Seven Different Cell Types

The PhenoLOGIC-based classification of HepG2 and NIH/3T3 cells in co-cultures showed that the features used to distinguish the two cell types were all SER and STAR morphology properties. This prompted an assessment of whether these properties alone would be sufficient to separate even more cell types from one another. Therefore, seven different cell lines, mouse fibroblasts (NIH/3T3), canine kidney epithelial cells (MDCK), human breast adenocarcinoma (MCF7), human lung carcinoma (A549), human hepatocellular carcinoma (HepG2) and human fibrosarcoma (HT1080) were seeded into a CellCarrier-384 Ultra microplate (three columns = 48 wells per cell type). The following day the cells were fixed and stained with Hoechst 33342 only. This time, single plane images were acquired on the Operetta CLS high-content analysis system using a 20x water immersion objective in confocal mode. A total of nine fields per well were acquired. Example images of the different cell types are shown in Figure 5.

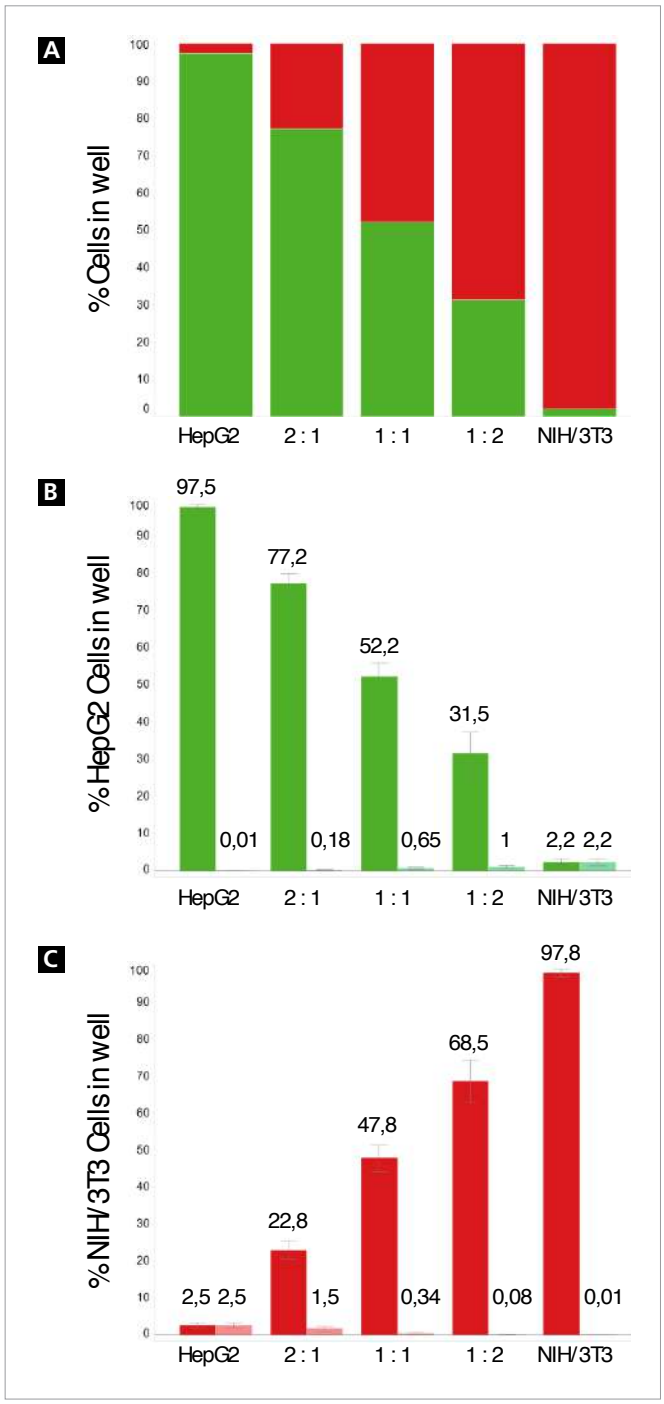

Figure 4. Results of linear classification for HepG2 and NIH/3T3 cells. HepG2 (green bars) and NIH/3T3 (red bars) cells were either cultured individually or as co-cultures at different ratios. (A) The graph shows the percentage of cells that were classified as either HepG2 or NIH/3T3 by PhenoLOGIC. (B) The percentage of cells classified as HepG2 (green) are plotted next to the percentage of cells falsely classified as HepG2 (light green) identified based on the CellTracker staining. The percentage of false positive cells ranges between 0.01 – 2.2%. (C) The percentage of cells classified as NIH/3T3 (red) are plotted next to the percentage of cells falsely classified as NIH/3T3 (light red) identified based on the CellTracker staining. The percentage of false positive cells ranges between 0.01 – 2.5%. HepG2 = only HepG2, 2:1 = 2x HepG2 in co-culture with 1x NIH/3T3 , 1:1 = 1x HepG2 in co-culture with 1x NIH/3T3, 1:2 = 1x HepG2 in co-culture with 2x NIH/3T3, NIH/3T3 = only NIH/3T3, n=96 wells for mono cultures, n=64 wells for co-cultures, error bars represent ± one standard deviation.

Image analysis was performed as for the co-culture experiment. However, this time only advanced SER texture and STAR morphology properties were calculated, not basic features such as intensity and classic morphology. As PhenoLOGIC can only distinguish up to six different classes, the SER and STAR morphology parameters were subjected to unsupervised principle component analysis (PCA) using High Content Profiler™ secondary data analysis software. Principal component analysis is a visualization method especially suited for multiparametric datasets like phenotypic profiles. It reduces the dimensionality of data sets allowing visualization of the similarities or differences among samples. As can be seen in Figure 6A, the seven cell lines form seven different well separated clusters. Each spot in the PCA corresponds to one well. When the plate layout information is used for annotation it becomes visible that each cluster is formed by wells from one cell line only (Figure 6B).

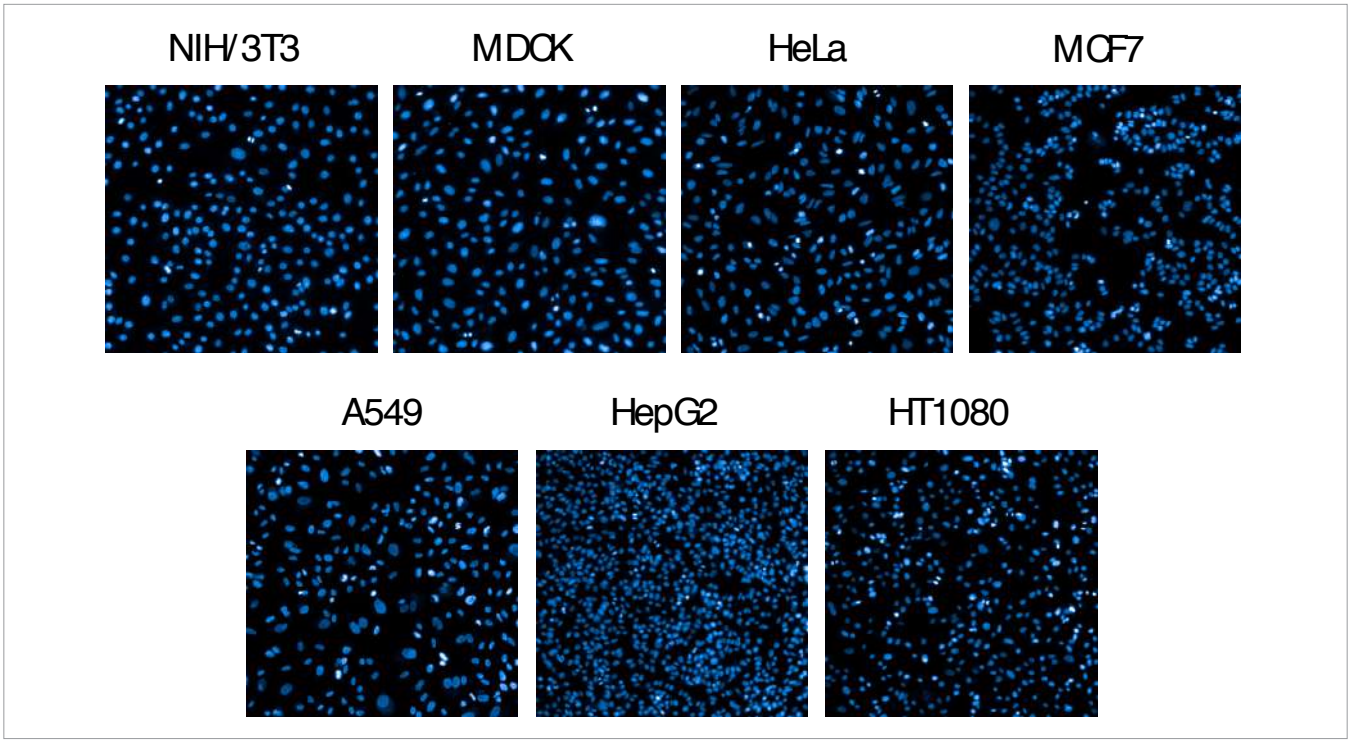

Figure 5. Nuclear phenotypes of seven different cell lines. Cells were stained with Hoechst and imaged on an Operetta CLS high-content analysis system using a 20x water immersion objective.

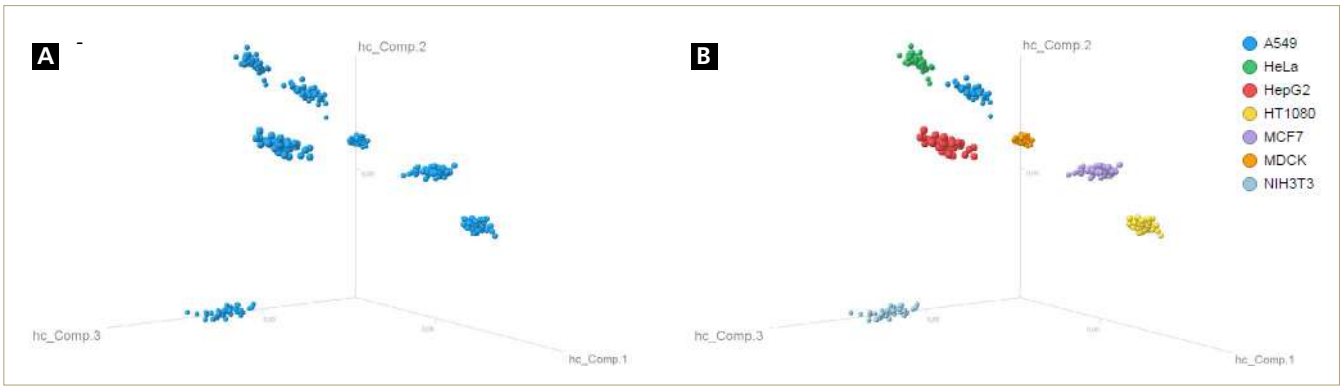

Figure 6. Three-dimensional Principle Component Analysis (PCA) of phenotypic profiles from seven different cell lines. The set of SER texture and STAR morphology parameters calculated in Harmony was subjected to PCA within High Content Profiler software. As can be seen in (A), seven distinct clusters are formed. If the plate layout information is used for annotation, it becomes visible that these clusters represent the seven different cell lines (B). Each spot represents one well. This clearly shows that SER texture and STAR morphology properties of the Hoechst nuclear staining are sufficient to distinguish seven different cell lines from one another.

Conclusions

The Hoechst staining of cell nuclei contains a plethora of information that can be used for much more than just aiding in segmentation during image analysis. As we have shown here, phenotypic profiling of the nucleus enables distinguishing of cells in co-cultures. Even up to seven individual cell lines can be separated by leveraging the Hoechst nucleus staining. This type of phenotypic analysis can be directly applied to other cell types such as primary cells co-cultured with feeder cells and furthermore, phenotypic profiling is not limited to the nucleus. Applying it to other fluorescent labels or even cells labeled by the more broad cell painting approach[2], opens up new horizons for unbiased drug discovery and disease research. The prerequisites for this type of phenotypic analysis are high-quality images, software for image segmentation and generation of phenotypic profiles and a solution to help with processing complex multiparametric datasets (reduction of dimensionality, hit selection). PerkinElmer offers a complete solution for phenotypic profiling applications. Imaging on either the Opera Phenix or Operetta CLS High Content Screening systems allows users to generate the high quality images required. Harmony software enables primary image analysis with accurate image segmentation and advanced morphology and texture quantification methods to generate highly descriptive phenotypic profiles. With PhenoLOGIC, Harmony software also provides an easy to use machine learning-based classifier that helps with dimensionality reduction. Further secondary analysis tools for data exploration and analysis are available in High Content Profiler. PerkinElmer's suite of products for phenotypic profiling enables you to leverage the real "content" of your high-content screening applications.

References

1. Shantanu Singh, Anne E. Carpenter and Auguste Genovesio Increasing the Content of High-Content Screening J Biomol Screen. 2014 Jun; 19(5): 640–650.
2. Bray, M.-A., Singh, S., Han, H., Davis, C. T., Borgeson, B., Hartland, C., Kost-Alimova, M., Gustafsdottir S. M., Gibson, C. C, Carpenter, A. E. (2016). Cell Painting, a high-content image-based assay for morphological profiling using multiplexed fluorescent dyes. Nature Protocols, 11(9), 1757–1774. doi:10.1038/nprot.2016.105.
3. Fisher, R. A. (1936) The use of multiple measurements in taxonomic problems. Annals of Eugenics, 7: 179-188 DOI: 10.1111/j.1469-1809.1936.tb02137.x.

PerkinElmer, Inc.
940 Winter Street
Waltham, MA 02451 USA
P: (800) 762-4000 or
(+1) 203-925-4602
www.perkinelmer.com

PerkinElmer®

For a complete listing of our global offices, visit www.perkinelmer.com/ContactUs

Copyright ©2017, PerkinElmer, Inc. All rights reserved. PerkinElmer® is a registered trademark of PerkinElmer, Inc. All other trademarks are the property of their respective owners.

013615_01 PKI

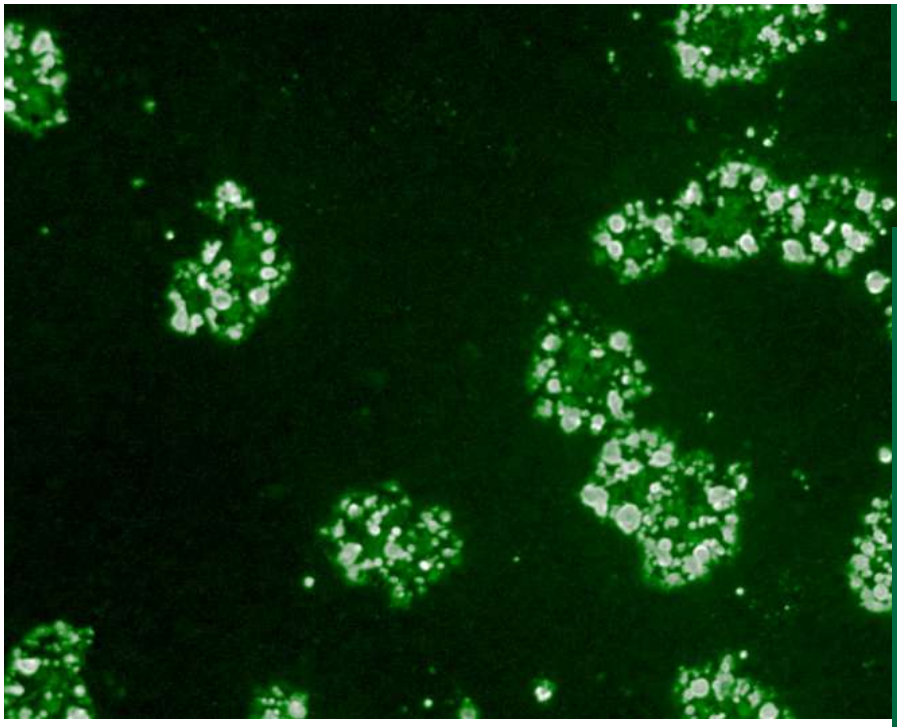

TECHNICAL NOTE

Multimode Detection

Authors:

Zhiyun Wen[1]
Daniel J. DiStefano[1]
Frauke Haenel[2]
Norbert Garbow[2]
Paul Fletcher[3]

[1]Merck Research Laboratories
West Point, PA, USA

[2]PerkinElmer, Inc.
Hamburg, Germany

[3]PerkinElmer, Inc.
Hopkinton, MA

Increased Throughput and Reduced Variability of Virus Plaque Assays with Automated Imaging and Analysis

Introduction

Plaque Assays are a standard method utilized by virologists to determine the concentration of viruses in solution. In contrast to PCR and immunofluorescent methods, which detect only the presence of virus particles, the plaque assay also identifies the amount of infectious virus particles or plaque forming units (PFU).

In plaque assays, a cell monolayer is incubated with a virus solution. If the virus is infectious, the cells usually detach or even lyse so that the monolayer becomes perforated. The infected cells and holes (plaques) are counted and represent the amount of infectious virus particles in solution.

In many laboratories, counting the plaques is performed manually in 6-, 12- or 24-well plates either by visual inspection or using a microscope. This is cumbersome, error prone and very time-consuming. Automated imaging and plaque analysis is rarely used.

In this note we show how the plaque imaging and analysis process can be automated to facilitate virologists in their daily workflow and throughput, using the EnSight™ Multimode Reader and its Kaleido™ Data Acquisition and Analysis Software. Using 96-well microplates further enhances the time saving benefit and qualifies this method for high-throughput screening (HTS) applications. Together with the EnSight's stacker system it is used routinely in compound screening with typically 20-40 plates daily.

For research use only. Not for use in diagnostic procedures.

PerkinElmer®
For the Better

Materials and Methods

Plaque Assay Principle

Adherent cells appropriate for virus growth are seeded in a 96-well microplate (for example: CellCarrier™-96, PerkinElmer) to result in approximately 90% confluency on the day of virus infection. 1:10 serial dilutions of virus are added in culture medium to the wells. The plates are incubated for one hour to allow the virus to infect the cells. After incubation, the virus dilutions are removed from the cell monolayer. 1% agarose is added to the monolayer to prevent further indiscriminate spreading of the virus by diffusion and thus ensures that virus infection is only transmitted between neighboring cells. The cell monolayers are incubated at room temperature until plaques are visible, after 3-10 days.

Plaque Staining

Plaques are stained after removing the agarose cover following standard staining protocols. In this technical note viruses were immuno-stained using specific primary antibodies and Alexa Fluor™ 488 labeled secondary antibodies.

Image Acquisition and Evaluation

For comparison purposes, plaque assays were evaluated manually as well as automatically after three days of incubation, which proved to be optimal for manual counting of this assay. Images were acquired using the EnSight Multimode Plate Reader equipped with imaging module. Manual plaque analysis was performed on these images by counting the plaques by eye. For the automated approach the EnSight system's Data Acquisition and Analysis Software Kaleido was used. The custom assay specific analysis method "Virus Plaque Analysis for Kaleido 2.0" was employed to evaluate the images. With this, the PFUs for each virus dilution were defined, which are utilized to calculate the amount of infectious virus particles in stock solutions.

Assay-specific analysis methods can be easily enabled by selecting a custom analysis file in Kaleido. This file is provided upon request by local PerkinElmer specialists.

Results

Image Evaluation of Lytic and Non-lytic Plaques

After infection, viruses induce structural changes in host cells, also called the cytopathic effect (CPE). These can be morphological alterations such as cell detachment (non-lytic plaques) or even cell lysis leading to holes in the monolayer (lytic plaques) as shown in Figure 1. Both types of plaque can be automatically analyzed by the patent pending approach used in the assay specific analysis method "Virus Plaque Analysis for Kaleido 2.0". This technical note focuses mainly on lytic plaque analysis.

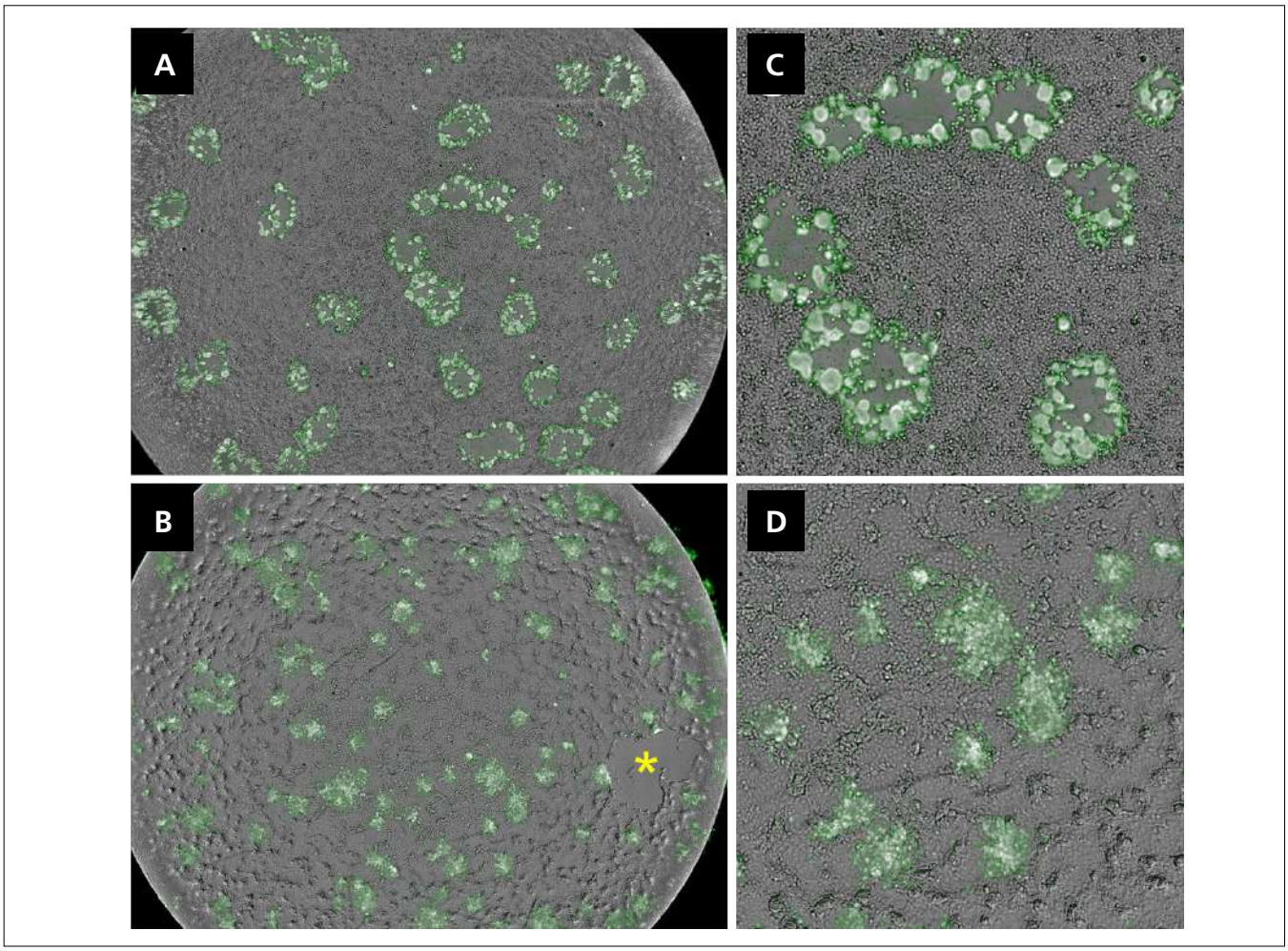

Figure 1. Well overview (left) and detail (right) showing cytopathic effects on the host cell caused by viral infection. The immuno-stained virus is shown by green fluorescence and overlaid with a brightfield image. Lytic plaques (A, C) are formed if the virus causes lysis of the host cell leading to holes in the monolayer. Non-lytic plaques (B, D) are formed if cells are infected and detach from the surface. The yellow asterisk marks a damaged region in the cell monolayer.

For lytic plaque type the image analysis requires a brightfield image, which is used to detect the cell layer. A cell layer in plaque assays can show cell-free centers of lytic plaques, but also damaged regions (see Figure 1B, yellow asterisk). The differentiation between damaged regions and lytic plaques is performed on a virus-specific fluorescence image: infection-specific fluorescence around cell-free regions is used to identify lytic plaques. In addition, non-lytic plaques are detected by searching for fluorescent regions that do not belong to lytic plaques (see Figure 2).

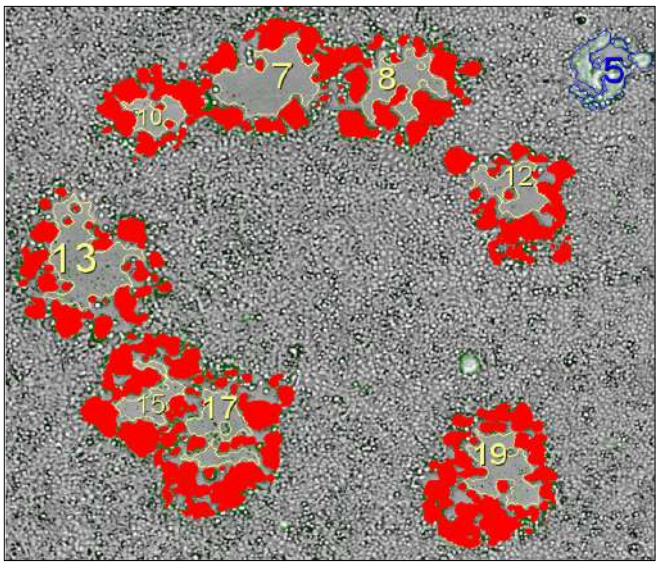

Figure 2. Image analysis mask shown on the brightfield/Alexa Fluor™ 488 overlay image of Figure 1, C. Cell-free regions in the cell layer that are surrounded by virus specific fluorescence (red mask) are defined as lytic-plaques (yellow mask with numbers). Fluorescent regions without any or with a too small cell-free center region are identified as non-lytic plaques (blue mask with number).

The plaque detection analysis method can be fine-tuned by means of several input parameters such as adjustment of texture and signal thresholds or defining minimum and maximum plaque size. This enables precise cell layer and plaque detection under several assay conditions.

The most important information obtained from a plaque assay is the number of plaques. This number is used to determine the concentration of PFUs in stock solution or to verify the impact of compounds on the virulence of viruses. As plaques often fuse at higher concentrations the analysis provides an estimated number of plaques taking also the plaque sizes into account. Of course, the number of actually counted plaques is available as well. Further parameters characterizing the fluorescence signal of infected cells or the background can be used for assay development, quality control or troubleshooting. Cell handling errors are indicated by the parameter "Area Fraction of Invalid Regions [%]" that determines the fraction of damaged regions in the cell layer, which can occur during seeding or pipetting. More parameters can be extracted from the analysis method, but the main output parameters are the ones shown in Table 1.

Table 1. Overview of image requirements and main output parameters of the assay specific analysis method "Virus Plaque Analysis for Kaleido 2.0".

Image Requirements
Brightfield Image for Cell Layer Detection (Optional for non-lytic plaque assays)
Virus Specific Fluorescence Image for Detection of Virus Infected Cell Regions
Main Output Parameters
Estimated Plaque Number (Weighted by Area)
Counted Number of Plaques
Counted Number of Non-lytic Plaques
Median Size of Plaques [µm²]
Fluorescence Signal of Infected Parts of Plaques
Median Fluorescence Signal Outside of the Plaques
Area Fraction of Invalid Regions [%]

Comparison of Automated and Manual Plaque Count

Several experiments were performed to assess the functionality and precision of the image analysis method "Virus Plaque Analysis for Kaleido 2.0" compared to manual plaque counting. The assay plates were imaged on the EnSight multimode reader. The images have been analyzed automatically during the measurement, manual plaque counting has been performed on these images by three persons (Analysts 1-3). A plate overview of Experiment 1 using 1:10 serial virus dilutions is shown in Figure 3.

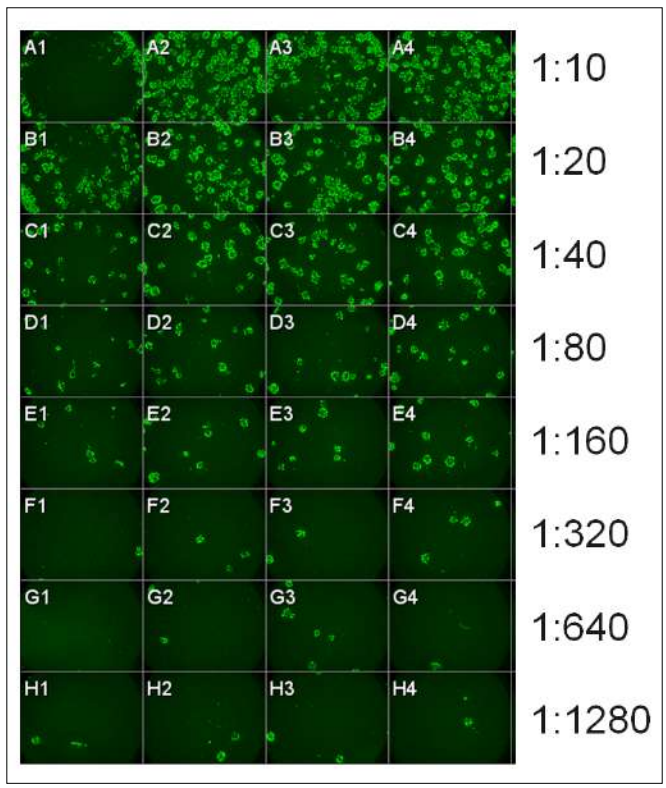

Figure 3. Overview of a plaque assay plate from experiment 1 showing 1:10 serial virus dilutions from top to bottom (A-H) in 4 replicates (1-4). The virus specific Alexa Fluor™ 488 fluorescence is shown in green. Well A1 was excluded as the image analysis reveals a very large "Area Fraction of Invalid Regions", which indicates potential issues in the sample preparation.

The number of counted plaques on the assay plate shown in Figure 3 correlates well with the applied virus dilution (Figure 4). Both automated and manual counting (analyst 1-3) result in very good linear regression and very similar R square values. In contrast, manual counting could not be performed for the two dilution steps 1:10 and 1:20 due to the high plaque density, which leads to merged plaques and makes it difficult to distinguish individual plaques from each other by eye. The automated approach, however, still properly detects individual plaques for both dilutions. The error bar of the lowest, 1:10, dilution is much higher than for other dilutions. Visual inspection of the images and analysis masks revealed that the plaques were counted and estimated correctly, but a varying number of plaques were formed in these wells (see also row A in Figure 3).

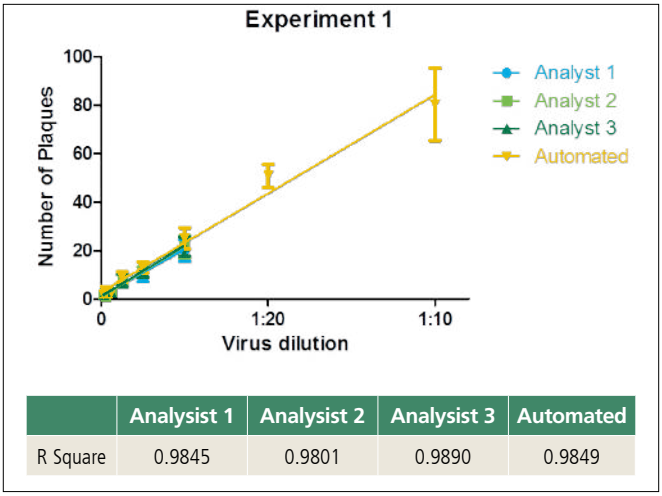

	Analysist 1	Analysist 2	Analysist 3	Automated
R Square	0.9845	0.9801	0.9890	0.9849

Figure 4. Linear correlation between virus dilution and number of plaques that were counted either manually by three different analysts or using the automated approach of the EnSight Multimode Reader. For the automated approach the output parameter "Estimated Plaque Number (Weighted by Area)" was used. Error bars indicate the standard deviation of four replicates.

Apart from the two dilutions, 1:10 and 1:20, that were not counted manually, experiment 1 resulted in very consistent plaque counts between all three analysts and the automated approach (Figure 5). However, this was not always the case. As a second experiment in Figure 5 indicates, three different analysts interpret plaques differently: whereas Analyst 1 and Analyst 3 count similar numbers of plaques as the automated approach, Analyst 2 overestimates the number of plaques especially for the 1:160 and 1:620 dilutions. This illustrates that manual counting underlies variations only because each person counts differently and does not define plaques in the same way. In contrast, the automated approach always evaluates plaque characteristics in the same way and is less susceptible to variations from experiment to experiment.

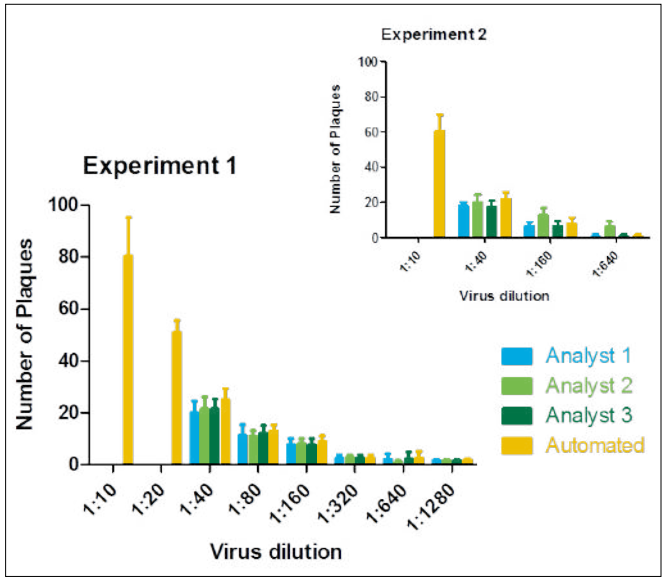

Figure 5. Number of plaques of two independent experiments showing consistent (Experiment 1), but also inconsistent plaque counts between the analysts (Experiment 2, dilution 1:160 and 1:620). For the automated approach the output parameter "Estimated Plaque Number (Weighted by Area)" was used. Error bars indicate the standard deviation of four replicates.

Conclusion

Automated plaque imaging and analysis using the EnSight Multimode Plate Reader enables rapid determination of the concentrations of virus solutions with higher precision and less effort.

- The assay specific analysis method "Virus Plaque Analysis for Kaleido 2.0" detects plaques even at high concentrations, which are difficult to count manually.
- Different CPEs, such as lytic and non-lytic plaques, that are formed by different types of viruses can be detected and analyzed.
- The image analysis method provides many additional output parameters that help with troubleshooting or uncover details of the cell layer that are not usually observed by a person focusing on counting plaques.
- The automated analysis is less error-prone, because it is independent of user specific plaque counts.
- Plaque assays are often performed in six-well plates, which are easier to count manually. However, using 96-well plates and automated analysis increases throughput and saves expensive working time.

PerkinElmer, Inc.
940 Winter Street
Waltham, MA 02451 USA
P: (800) 762-4000 or
(+1) 203-925-4602
www.perkinelmer.com

PerkinElmer

For a complete listing of our global offices, visit www.perkinelmer.com/ContactUs

Copyright ©2018, PerkinElmer, Inc. All rights reserved. PerkinElmer® is a registered trademark of PerkinElmer, Inc. All other trademarks are the property of their respective owners.

014015_01 PKI

APPLICATION NOTE

AlphaLISA/ELISA Technology

Author:
Adam Carlson

PerkinElmer, Inc.
Hopkinton, MA

A Comparative Study of Two Immunoassay Platforms to Determine Lentivirus Titer for CAR-T Development

Introduction

Lentiviral transduction is an effective method of gene transfer used to generate cell lines expressing a gene of interest. Lentivirus can infect both dividing and non-dividing cells, which makes it a useful tool for difficult to transfect cell lines and provides long-term stable expression of a transgene.[1] One commonly utilized lentiviral vector backbone originates from human immunodeficiency virus (HIV). In order to use the HIV as a vector, essential genetic and respective phenotypic components are critical to combine with supporting elements from packaging and envelope plasmids. Splitting the HIV sequence across multiple vectors followed by co-transfection minimizes the likelihood of a single replication competent, pathogenic lentivirus, enabling safer production and handling in the laboratory. The p24 capsid protein of HIV remains on the lentivirus vector which facilitates viral titer determination via an immunoassay such as an ELISA (enzyme-linked immunosorbent assay). Lentivirus can be generated by transiently transfecting the helper plasmids along with the gene of interest into a packaging cell line (typically 293T cells) and harvesting the cell supernatant which contains the lentivirus product.[2,3]

For research use only. Not for use in diagnostic procedures.

PerkinElmer®
For the Better

Lentivirus is frequently used to deliver DNA to T-cells to generate CAR-T cell (chimeric antigen receptor T-cell) products.[4] CAR-T cells are one approach to immunotherapy wherein T-cells are removed from a patient and then genetically modified to contain CARs to target surface antigens on tumors for eradication. CAR-T cells are expanded *ex vivo* before injecting back into the patient for treatment. CAR design consists of an extracellular domain, typically a scFv from a monoclonal antibody to recognize the tumor antigen, and a linker or spacer followed by a transmembrane domain (ex CD3ζ) and an intracellular signaling domain that acts in a stimulatory fashion to the T-cells (ex CD28, or 4-1BB) to facilitate destruction of the cancer cells.[5]

When producing lentivirus, measurement of the viral titer enables the determination of the efficiency of the transient co-transfection as well as normalization of the amount of lentivirus used across experiments. The p24 protein pool that is quantified contains a variable amount of free p24 as well as p24 from non-functional vector particles.[2] The Alliance HIV-1 p24 Antigen ELISA kit (for Research Use Only, PerkinElmer, Inc.) is a commonly used p24 immunoassay in the HIV field[6,7] to determine viral titer.[8,9,10] An ELISA is a sandwich immunoassay designed to detect the presence of a target ligand (generally a protein) in a liquid sample (Figure 1). In the Alliance HIV-1 p24 ELISA, an antibody specific for HIV-1 p24 is coated on the assay plate and used to capture the p24 present in the sample. After incubation with the sample and multiple wash steps, a second biotinylated antibody against HIV-1 p24 is added for detection. Excess unbound antibody is washed away and then streptavidin conjugated to horseradish peroxidase (HRP) binds the biotin of the secondary detection antibody. After additional washing, the HRP is treated with an ortho-phenylenediamine-HCl (OPD) substrate to produce a color change. In the termination step facilitated by the addition of acid, the amount of target in the sample can be quantified by absorbance (optical density, OD) as determined from the standard curve.

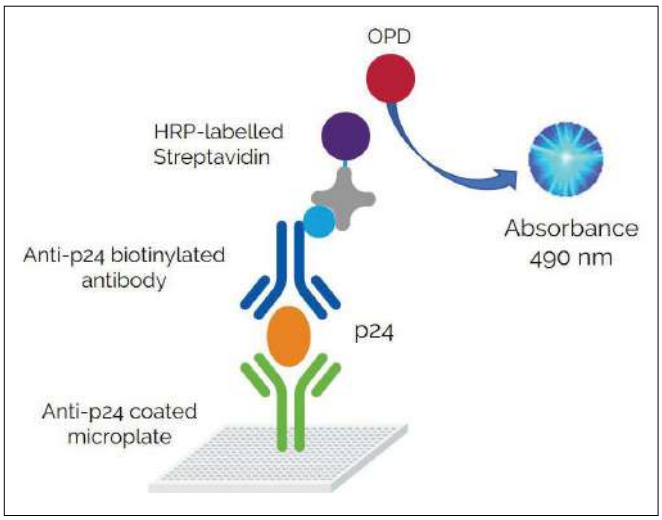

Figure 1. Alliance HIV-1 p24 Antigen ELISA assay principle. Refer to text for details.

The AlphaLISA® (PerkinElmer, Inc.) bead-based sandwich immunoassay (similar to ELISA) is used to study biomolecular interactions in a microplate format (Figure 2). Alpha technology offers flexibility as well as higher throughput capability since it utilizes a higher density microplate format and is automation friendly. The technology was originally developed for drug discovery screeners and has been adopted as an immunoassay alternative. The acronym "Alpha" stands for Amplified Luminescent Proximity Homogeneous Assay. Binding of antibodies captured on donor and acceptor beads and subsequent binding to the analyte form a complex. Excitation of the donor results in energy transfer from the donor bead to the acceptor bead in the complex producing a luminescent/fluorescent signal. The AlphaLISA HIV-1 p24 detection assay (for Research Use Only, PerkinElmer, Inc.) can also be used to assess viral titers in a high throughput format. In this study, we demonstrate a comparative quantification of the p24 titer in a GFP control lentiviral sample using both the Alliance HIV-1 p24 Antigen ELISA and the p24 AlphaLISA assay platforms.

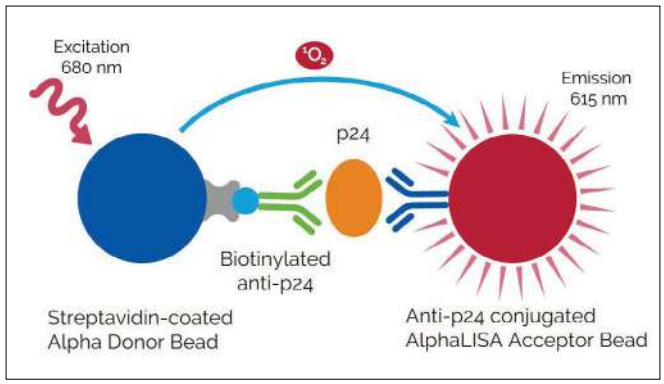

Figure 2. AlphaLISA p24 Assay Principle. A biotinylated anti-p24 antibody is bound by the Streptavidin-coated AlphaLISA Donor beads, while another anti-p24 antibody is directly conjugated to AlphaLISA Acceptor beads. In the presence of p24, the donor and acceptor beads both bind the target and come into proximity. Excitation of the donor beads at 680 nm provokes the release of singlet oxygen molecules that trigger a cascade of chemical reactions in the acceptor beads in proximity, resulting in maximum emission at 615 nm. AlphaLISA signal is proportional to the amount of p24 present in the sample.

Materials and Methods

Reagents and Consumables

- GFP control Lentivirus (Genecopoeia, #L303-100)
- AlphaPlate-384, light gray (PerkinElmer, #6005350)
- AlphaLISA kit – p24 High Sensitivity (PerkinElmer, #AL291C)
- Alliance HIV-1 p24 Antigen ELISA (PerkinElmer, #NEK050001KT)
- Fetal bovine serum (FBS), heat inactivated (Thermo Fisher, #10082-147)
- Dulbecco's Modified Eagle's Medium, DMEM (ATCC, #30-2002)

Data Collection and Analysis

Control GFP lentivirus was thawed from an aliquot on each day of testing and carefully diluted into cell culture media (DMEM + 10% FBS) to simulate lentivirus production from 293T cells. Serial dilutions of the mock lentivirus were generated across a wide span of concentrations for testing.

The AlphaLISA p24 assay was performed following PerkinElmer's recommended protocol. Each assay required 5 µL of test sample in a 50 µL reaction. AlphaLISA signal was measured on a PerkinElmer EnVision® 2105 Multilabel plate reader using default values for Alpha detection of the luminescent/fluorescent label. MyAssays Desktop® software was used to graph the standard curve and interpolate the unknown values using a four-parameter logistic curve with $1/y^2$ weighting.

The Alliance HIV-1 p24 Antigen ELISA was performed following PerkinElmer's recommended protocol. The assay required 200 µL of test sample. Absorbance at 490 nm was measured on a PerkinElmer EnVision 2105 Multilabel plate reader using the appropriate settings. MyAssays Desktop® was used to graph the standard curve and interpolate the unknown values using linear regression curve fitting.

Results

In order to determine a viral titer, the amount of p24 in the lentiviral stock is quantified. To do this, standard curves using purified p24 are tested to determine the reference signal at each concentration in each assay. Standard curves were run for both the AlphaLISA p24 and Alliance p24 ELISA assays using the purified p24 protein included in each kit (Figure 3). The first assay tested with lentivirus samples was the AlphaLISA due to the simple, rapid assay workflow and generally wide dynamic range of the technology. Figure 3 compares the standard curve from each assay technology and demonstrates the broader dynamic range of the AlphaLISA assay relative to the ELISA assay.

A very broad initial dilution series of the GFP lentivirus (4-fold to 50,000-fold) was generated for the initial AlphaLISA assessment due to the unknown titer of the concentrated GFP control lentiviral stock. Figure 4 shows the average AlphaLISA signal of each dilution point. There is a clear hook effect from high titer of p24 present in the first four dilution points in the series due to an excess of target molecules oversaturating the Donor and the Acceptor beads, which inhibits their association.

The AlphaLISA assay was repeated and run in parallel with the Alliance p24 ELISA using a starting dilution of 1000-fold with serial 2-fold dilutions to fall within the linear range of both assays. All 12 AlphaLISA dilutions were linear and the interpolated concentration of p24 (pg/mL) is shown in Figure 5. The average p24 titer of the GFP lentiviral stock as determined by AlphaLISA assay (correcting for dilution factor) was 6.14 x 10^6 pg/mL.

For the Alliance p24 ELISA, only dilutions 5 through 12 were tested in the assay with results plotted along with the AlphaLISA data in Figure 5. The top two dilutions and bottom three dilutions were outside the dynamic range. Therefore, only three data points fell within the linear range of the ELISA assay. For best accuracy when performing an ELISA, the OD of the unknown samples should fall within the dynamic range of the standard curve. The average p24 titer of the GFP lentiviral stock as determined by the samples within the standard curve range (correcting for dilution factor) using the Alliance HIV-1 p24 Antigen ELISA was 5.32 x 10^6 pg/mL. The quantified p24 for both assays correlate well, showing the utility and accuracy of both methods for determining viral titer.

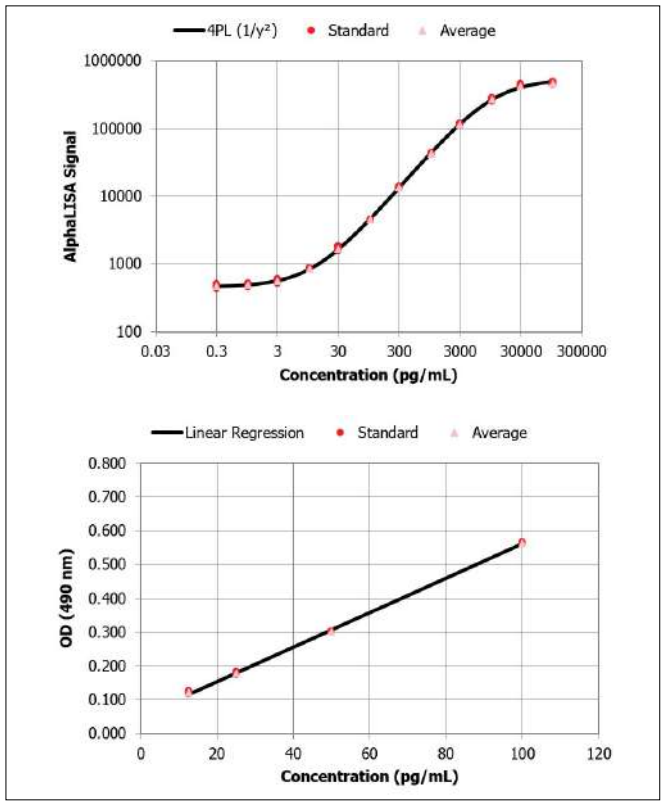

Figure 3. p24 Standard Curve from each assay technology. (Top) AlphaLISA standard curve provides ~ 4 logs of dynamic range (Bottom) ELISA standard curve provides ~2 logs of dynamic range.

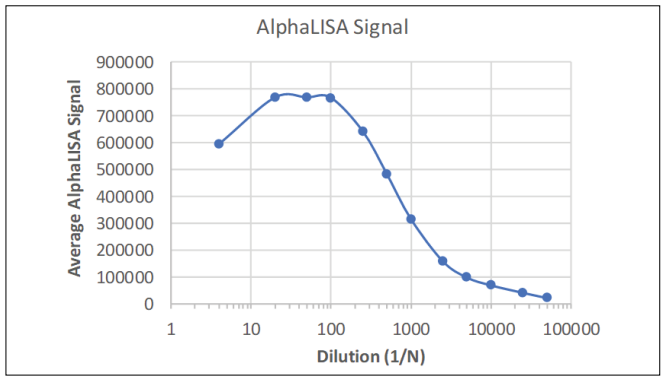

Figure 4. Average p24 AlphaLISA counts at each dilution point. Dilution point #1 equals 4-fold whereas dilution point #12 equals 50,000-fold from the stock GFP Lentivirus. The AlphaLISA signal of dilutions #2 through #4 are above the top values of the standard curve that was run in parallel and should not be used. Dilution #1 (4-fold) is a hooked data point which also should not be factored when interpolating the unknown viral titer.

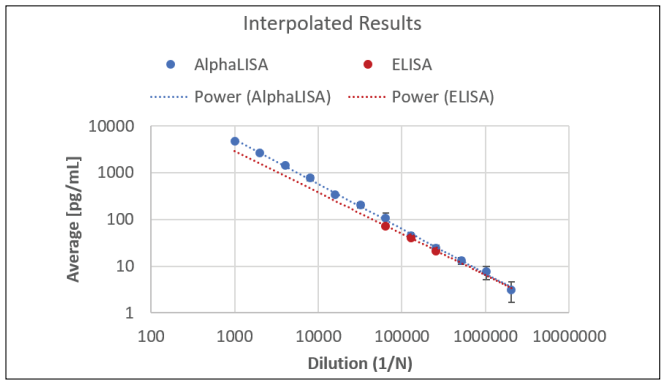

Figure 5. p24 AlphaLISA and ELISA assay results. Interpolated pg/mL of p24 from unknown samples within the linear range of each assay. R^2 for AlphaLISA is 0.998 and for ELISA is 0.998.

Conclusion

As stated above, determination and control of the viral titer is a critical step during the use of viral vectors for cell and gene therapy applications. When using lentiviruses, for example HIV based constructs, the capsid protein p24 is an important marker for measurement of the titer using immunoassays. In the current study, we demonstrated the use of two immunoassay platforms to determine the viral titer by quantitation of p24. The Alliance HIV-1 p24 ELISA kit (Research Use Only, PerkinElmer, Inc.) is widely cited and is considered to be a standard for lentiviral titer.[8,9,10] The AlphaLISA HIV-1 p24 detection assay (Research Use Only, PerkinElmer, Inc.) is an ELISA alternative technology and uses a platform originally developed for drug discovery screeners. The two immunoassay platforms were used to measure p24 concentration from a mock lentiviral supernatant (concentrated lentivirus control stock diluted into cell culture media). Based on the laboratory infrastructure and workflow volumes, two immunoassay platform options are now available to measure p24 as a titer marker for lentivirus driven CAR-T generation.

References

1. Morgan and Boyerinas (2016). Genetic modification of T Cells. *Biomedicines,* 4, 9.
2. Geraerts M, et al. (2006). Comparison of lentiviral titration methods. *BMC Biotechnology,* 6:34.
3. Merten OW, et al. (2016). Production of lentiviral vectors. *Molecular Therapy – Methods and Clinical Development,* 3, 16017.
4. Picanço-Castro V, et al. (2020) Establishment of a simple and efficient platform for CAR-T cell generation and expansion: from lentiviral production to *in vivo* studies. *Hematology, Transfusion and Cell Therapy,* 42(2) 150-158.
5. Androulla and Lefkothea (2018). CAR T-cell Therapy. A New Era in Cancer Immunotherapy. *Current Pharmaceutical Biotechnology,* 19, 5-18.
6. Torimiro JN, et al. (2013). Evaluation of Virologic Methods for Early Detection of HIV-1 in a Resource-limited Setting: Performance and Cost Analysis. *Health Sciences and Diseases:* Vol. 14 (3).
7. Patton JC, et al. (2006). Ultrasensitive Human Immunodeficiency Virus Type 1 p24 Antigen Assay Modified for Use on Dried Whole-Blood Spots as a Reliable, Affordable Test for Infant Diagnosis. *Clinical and Vaccine Immunology,* Vol. 3 (1) 152–155.
8. Valkama A, et al. (2018). Optimization of lentiviral vector production for scale-up in fixed-bed bioreactor. *Gene Therapy,* 25, 39-46.
9. Majdoul S, et al. (2017). Peptides derived from evolutionarily conserved domains in Beclin-1 and Beclin-2 enhance the entry of lentiviral vectors into human cells. *Journal of Biological Chemistry,* 292(45):18672-18681.
10. Lesch H, et al. (2011). Production and purification of lentiviral vectors generated in 293T suspension cells with baculoviral vectors. *Gene Therapy,* 18, 531-538.

PerkinElmer, Inc.
940 Winter Street
Waltham, MA 02451 USA
P: (800) 762-4000 or
(+1) 203-925-4602
www.perkinelmer.com

PerkinElmer®

For a complete listing of our global offices, visit www.perkinelmer.com/ContactUs

Copyright ©2020, PerkinElmer, Inc. All rights reserved. PerkinElmer® is a registered trademark of PerkinElmer, Inc. All other trademarks are the property of their respective owners.

129332 PKI

APPLIED GENOMICS

APPLICATION NOTE

Rapid Characterization of AAV Capsid Proteins by Microfluidic CE-SDS:

A Quantitative Reproducible Alternative to Gel Electrophoresis

LabChip® GXII Touch™ Protein Characterization System

Introduction

Adeno-associated virus (AAV) particles are used extensively in R&D and clinical applications, such as gene therapy, due to their low immunogenicity in humans. AAV consists of a protein shell which encapsulates a small genome roughly 4.7 kb in size and is dependent on co-infection with helper viruses to replicate. The AAV genome contains *Rep* (replication), *Cap* (capsid), and assembly genes. The *Rep* gene encodes four proteins which are required for genome replication and packaging. The *Cap* gene produces three viral proteins (VP) known as VP1, VP2, and VP3 which form the protective outer shell of the capsid and perform host cell binding.

To visualize VP1, VP2, and VP3, SDS-PAGE with silver stain, a labor and time intensive process, is used to yield qualitative data with poor reproducibility. This procedure can take even the most experienced user hours to complete and many sources of error include: gel overheating, overloading, and inadequate standardization of stain/destaining. A rapid, quantitative, and reproducible alternative utilizes the LabChip® GXII Touch™ HT system[1,2] (Figure 1). This system is a high throughput instrument for the analysis of glycoproteins and nucleic acids via microfluidic capillary electrophoresis in the presence of SDS (CE-SDS). The ProteinEXact™ assay for the LabChip® GXII Touch™ system utilizes an on-system calibration step to enable high precision reproducibility along with improved sensitivity and broad sizing range. Sample analysis is completed in 65 seconds.

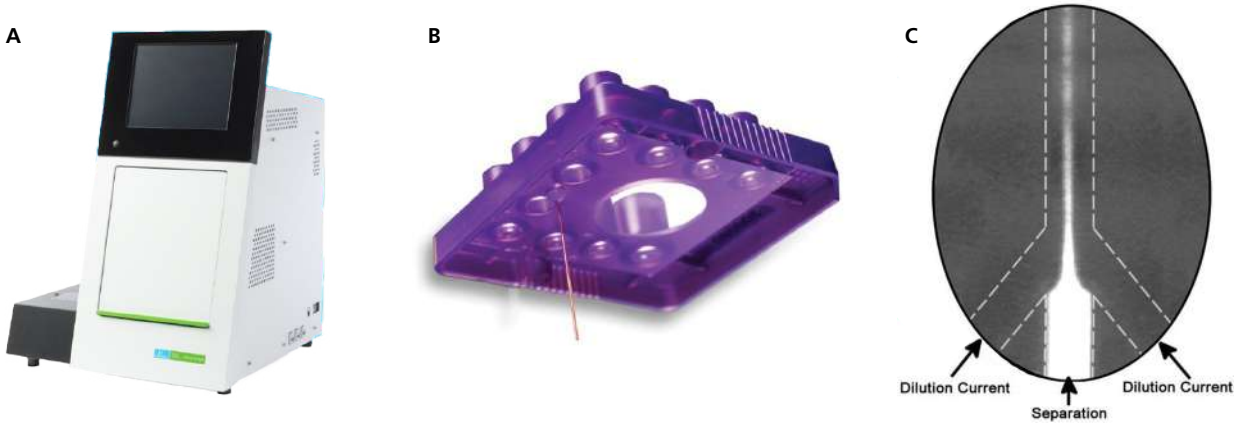

Figure 1: The LabChip® GXII Touch™ instrument (A) uses a quartz sipper chip (B) which allows for testing of up to 400 samples. (C) the fluorescent image shows how proteins are separated and destained in the microfluidic channels.

For research use only. Not for use in diagnostic procedures.

PerkinElmer®
For the Better

Methods

AAV serotype 8 (AAV8) was purchased from a commercial provider (catalog #A81000, Welgen Inc., Worcester MA). Material was generated in HEK-293 cells, was reported to contain at least 5 x 10^{12} genome copies (GC)/mL, and was supplied in 10% glycerol in PBS.

In accordance with the protocol for the ProteinEXact™ assay[3]:

- In a hardshell 96 well V-bottom SBS plate (catalog #6008870, PerkinElmer, Waltham MA) 2.5 µL of sample was added to 18 µL of nonreducing sample buffer in each well to be tested.
- The plate was sealed, heated at 70°C for 10 minutes, and cooled to room temperature.
- 35 µL of Milli-Q® water (Millipore, Bedford MA), was added to each well and mixed.
- The plate was spun at 1200 RCF at room temperature to remove bubbles and then submitted to analysis on the LabChip® GXII Touch™ HT system.

The thermal stability of AAVs is reported to vary with serotype. The melting temperatures of multiple AAV serotypes have been measured and exhibited a range from 66°C to 90°C[4]. The host cell in which the AAVs were generated and the degree of DNA packing (the empty/full ratio) should also be considered as variables. For these reasons, serotype-specific methods for denaturation of the AAV particles are recommended prior to routine analysis. We suggest that AAV samples be heated in a stepwise manner (2°C steps) from 60°C to 95°C to determine the optimal temperature for complete denaturation without destruction. Heating for 10 minutes has been adequate (data not shown) although we advise that a range from 5 to 15 minutes be explored during method development. Alternatively, the denaturation method that has worked well for SDS-PAGE can be adopted.

Results

The output of the ProteinEXact™ assay run on the LabChip® Reviewer software is a relative electropherogram (egram) with quantitative analysis of size, concentration, and percent contribution of each individual protein relative to the total protein in the sample; those proteins include VP1, VP2, VP3, and substantial protein impurities. The electropherogram along with an in-silico silver stain gel view is provided in Figure 2.

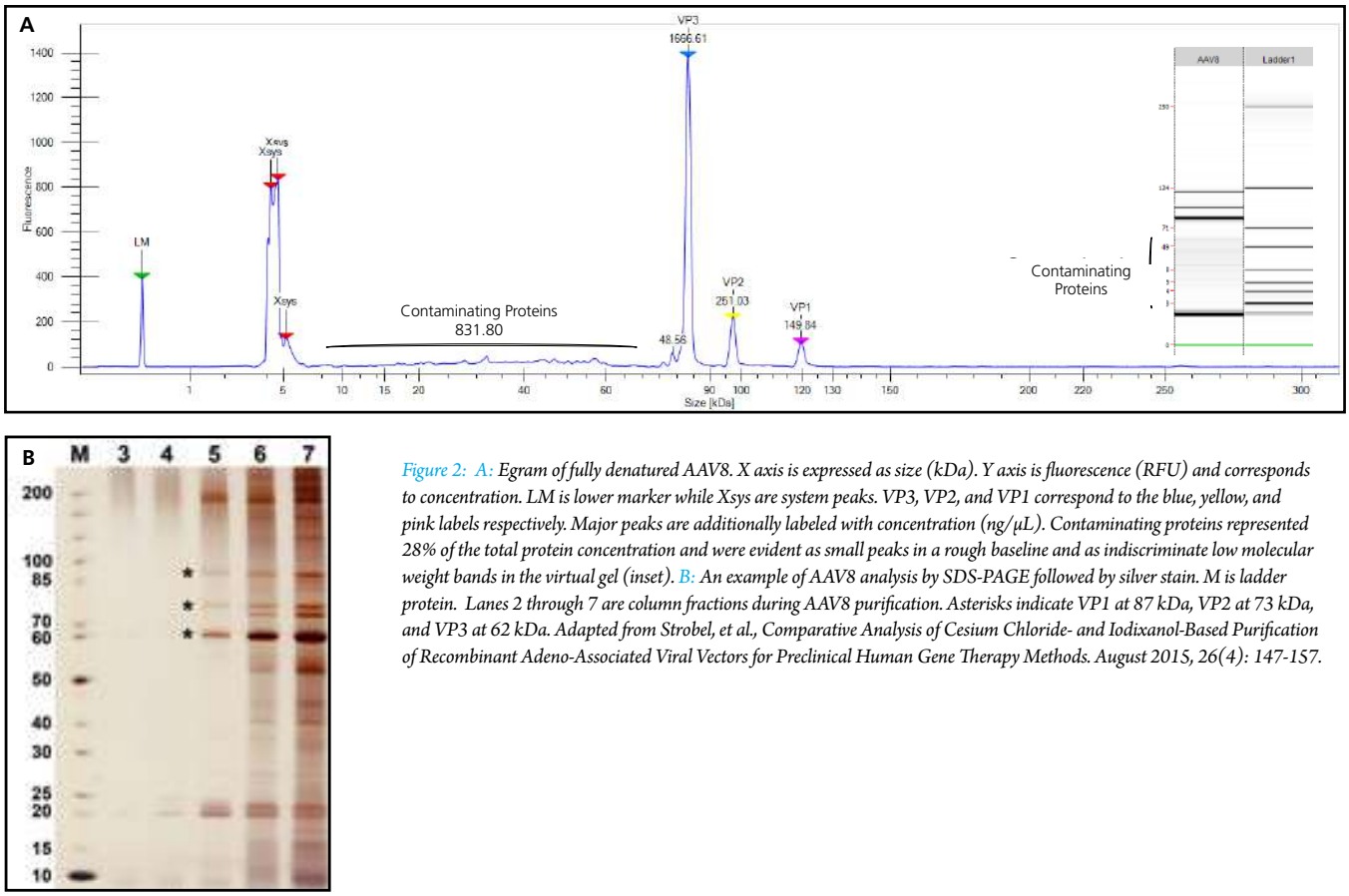

Figure 2: A: Egram of fully denatured AAV8. X axis is expressed as size (kDa). Y axis is fluorescence (RFU) and corresponds to concentration. LM is lower marker while Xsys are system peaks. VP3, VP2, and VP1 correspond to the blue, yellow, and pink labels respectively. Major peaks are additionally labeled with concentration (ng/µL). Contaminating proteins represented 28% of the total protein concentration and were evident as small peaks in a rough baseline and as indiscriminate low molecular weight bands in the virtual gel (inset). B: An example of AAV8 analysis by SDS-PAGE followed by silver stain. M is ladder protein. Lanes 2 through 7 are column fractions during AAV8 purification. Asterisks indicate VP1 at 87 kDa, VP2 at 73 kDa, and VP3 at 62 kDa. Adapted from Strobel, et al., Comparative Analysis of Cesium Chloride- and Iodixanol-Based Purification of Recombinant Adeno-Associated Viral Vectors for Preclinical Human Gene Therapy Methods. August 2015, 26(4): 147-157.

The corrected area under the curve (AUC) for each protein was automatically calculated by the LabChip® Reviewer software. The AUCs correspond to concentration (ng/µL) and were used to determine the ratio of the VPs within the sample. The reproducibility of the assay (Figure 3) was demonstrated by the overlay of twelve egrams.

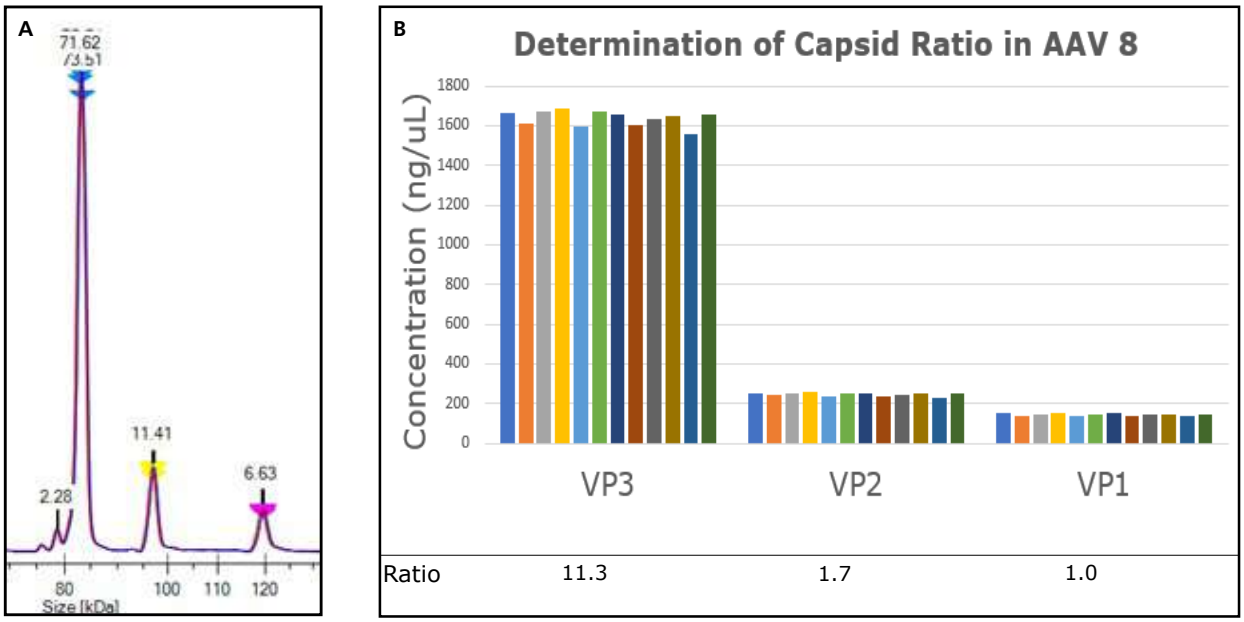

Figure 3: A: Twelve egrams were overlaid to demonstrate reproducibility of the assay of the fully denatured AAV8. X axis is expressed as size (kDa). Y axis is fluorescence (RFU) and corresponds to concentration. VP3, VP2, and VP1 correspond to the blue, yellow, and pink labels respectively. Peaks are labelled with their % contribution to the total protein in the sample. A small peak at 79 kDa represents 2.3% of the total protein. The identity of this fourth peak is not known. B: The calculated ratio of VP3 to VP2 to VP1 was based on the average concentration for each peak, normalized to VP1. The ratio of VP3 to VP2 to VP1 was equal to 11.3 to 1.7 to 1.0.

Discussion

Denaturation of AAV8 and subsequent analysis by microfluidic CE-SDS resulted in a rapid, reproducible, and quantitative measure of VP1, VP2, VP3, along with measurable evidence of contaminating proteins. VP ratios were similar to what was expected (1:1:10). The molecular weights of denatured VP1, VP2, and VP3 were determined to be 119, 97, and 83 kDa respectively as compared to the reported values of 87, 73, and 62 kDa[5]. The apparent MWs between methods can differ, a phenomenon that is routinely observed with monoclonal antibody analysis: mAbs are reported to be 150 kDa by SDS-PAGE but more typically run at 160-170 kDa on any CE-SDS platform. Researchers may want to run each VP individually on both platforms to verify results.

Conclusion

Denaturation of AAV8 and subsequent analysis by microfluidic CE-SDS resulted in a rapid, reproducible, and quantitative measure of VP1, VP2, VP3, along with measurable evidence of contaminating proteins. The ProteinEXact™ assay delivered rapid, reproducible, quantitative results of AAV8 capsid proteins when run on the LabChip® GXII Touch™ HT system. The method is a quantitative alternative to qualitative interpretation of SDS-PAGE. The LabChip® GXII Touch™ HT system aids researchers in studying AAVs, allowing for correlations to be made between *in vitro* and *in vivo* measurements of purity and capsid ratios to *in vivo* observations.

References

1. Smith, MT, *et al.* Establishment and Validation of a Microfluidic Capillary Gel Electrophoresis Platform Method for Purity Analysis of Therapeutic Monoclonal Antibodies. Electrophoresis. 2017 May 38 (9-10):1353-1365.
2. Chunk, WK, *et al.* Effects of Antibody Disulfide Bond Reduction on Purification Process Performance and Final Drug Substance Stability. Biotechnol Bioeng. 2017 Jun;114(6):1264-1274.
3. PerkinElmer. ProteinExact™ HR Assay User Guide, For LabChip® GXII Touch. www.perkinelmer.com/lab-solutions/resources/docs/GDE_ProteinEXact_HR_User_Guide.pdf. Accessed 9-5-2019.
4. Bennett, A. *et al.* Thermal Stability as a Determinant of AAV Serotype Identity. Molecular Therapy: Methods and Clinical Development. 2017, 6:171-182.
5. Backovic, A. *et al*. Capsid Protein Expression and Adeno-Associated Virus Like Particles Assembly in *Saccharomyces cerevisiae.* Microb Cell Fact. 2012; 11: 124.

For more information about the LabChip® GXII Touch™ workstation visit:

perkinelmer-appliedgenomics.com/labchip-gxii

PerkinElmer, Inc.
940 Winter Street
Waltham, MA 02451 USA
P: (800) 762-4000 or
(+1) 203-925-4602
www.perkinelmer.com

PerkinElmer®

To learn more, visit www.perkinelmer-appliedgenomics.com

Copyright ©2019, PerkinElmer, Inc. All rights reserved. PerkinElmer® is a registered trademark of PerkinElmer, Inc. All other trademarks are the property of their respective owners.

AG011909_11_AP PKI

APPLICATION NOTE

Pre-clinical *in vivo* imaging

Authors

Jean-Baptiste Gossart
Valérie Kédinger
Géraldine Guérin-Peyrou
Patrick Erbacher
Anne-Laure Bolcato-Bellemin

Polyplus-transfection SA
Illkirch, France

Bioimaging of Gene Delivery with *In Vivo*-jetPEI®

Introduction

The delivery of nucleic acids into cells is essential for basic research as well as medical applications such as gene therapy. Viral vectors are efficient carriers, but their use is limited because of their safety (induction of immune response, virus-associated pathogenicity). These concerns have increased the interest of non-viral methods for *in vivo* gene delivery. Second generation of non-viral vectors offers improved performance and safety, potentially providing an alternative to viral gene delivery.

One of the most promising non-viral vectors is the cationic polymer polyethylenimine (*in vivo*-jetPEI®). It offers high performance in terms of efficiency, reproducibility and robustness. Thanks to its high cationic charge density potential, *in vivo*-jetPEI® can condense DNA to form stable complexes termed polyplexes and promote gene transfer into cells.[1] It is the most widely used technology to deliver gene in animals.[2,3,4]

PerkinElmer imaging systems offer unique opportunities for *in vivo* bioluminescent imaging. This technique allows the non-invasive detection and quantification of plasmid biodistribution in different organs, and can be used to detect luciferase encoding plasmids delivered with *in vivo*-jetPEI®. We took the benefice of this system to determine the essential parameters for efficient gene delivery using *in vivo*-jetPEI® in mice. This application note illustrates the use of the non-invasive whole animal IVIS® imaging system to detect and quantify transgene expression, following *in vivo*-jetPEI® mediated plasmid DNA delivery.

PerkinElmer®
For the Better

Effect of Nitrogen Over Phosphate (N/P) Ratio on Delivery Efficiency

Only positively charged complexes can bind the cell surface via interaction with negatively charged syndecans.[5] The overall charge of the *in vivo*-jetPEI®/DNA complexes is crucial for efficient delivery. It is determined by the DNA to reagent ratio. This ratio which represents the ionic balance within the complexes is classically defined as the N/P ratio, referring to the number of nitrogen residues (N) in the *in vivo*-jetPEI® per phosphate (P) of DNA. *In vivo*-jetPEI®/DNA complexes become positively charged when excess nitrogen residues are present versus phosphate residues of DNA. An N/P > 3 is required.

Examples of complex charge and size at different N/P ratio are showed in Figure 1A. Moderate particle charge is necessary for the colloidal stability of the formulation since strong repulsive forces between the particles prevent aggregation. The charges of complexes obtained with the N/P ratio of 6, 8 and 10 have a good stability for *in vivo* applications whereas the complexes formed at the N/P ratio of 3 are too weak. Higher N/P ratios (6, 8 and 10) give particles of small size, comprised between 43 and 48 nm (Figure 1A) perfectly suitable for *in vivo* application.

The non-invasive IVIS100 system from PerkinElmer was used to follow the luciferase plasmid expression upon systemic delivery with *in vivo*-jetPEI® through retro-orbital injection of the venous sinus. One day post-injection the luciferase signal could only be detected in the lungs and only for N/P ratio > 3 (Figure 1B). The level of luciferase expression in the lung was similar at N/P ratios of 6, 8 and 10 (respectively 6.4 x 10^4, 5.0 x 10^4 and 3.9 x 10^4 photons/s) (Figure 1B). After imaging, different organs, including lungs, were dissected, homogenized and the organ extracts were assayed for luciferase expression. The luciferase signal was measured with a luminometer and expressed as relative light unit (RLU) per mg of protein. As shown in Figure 1C, a good correlation was observed between bioluminescent imaging in whole animal and luciferase assay in lung extract. However, the luciferase assay performed on organ extracts was able to detect much lower levels of luciferase expression that were not detected by whole animal imaging. As shown in Figure 1D, upon organ dissection and homogenization, luciferase expression was determined in spleen, liver, kidney and heart extracts using a luciferase assay. In the spleen, kidney and heart, the N/P ratios of 8 and 10 seem to give higher luciferase expression than the N/P ratio of 6. In the liver, the N/P of 8 is slightly better than the other N/P ratios. Hence the DNA to *in vivo*-jetPEI® ratio and the injection conditions should be adapted to the targeted organ. Collectively, these data show that the IVIS100 imaging system is able to detect 99% of the emitted luciferase signal, while the remaining 1% can be determined with a luciferase assay performed on organ extracts.

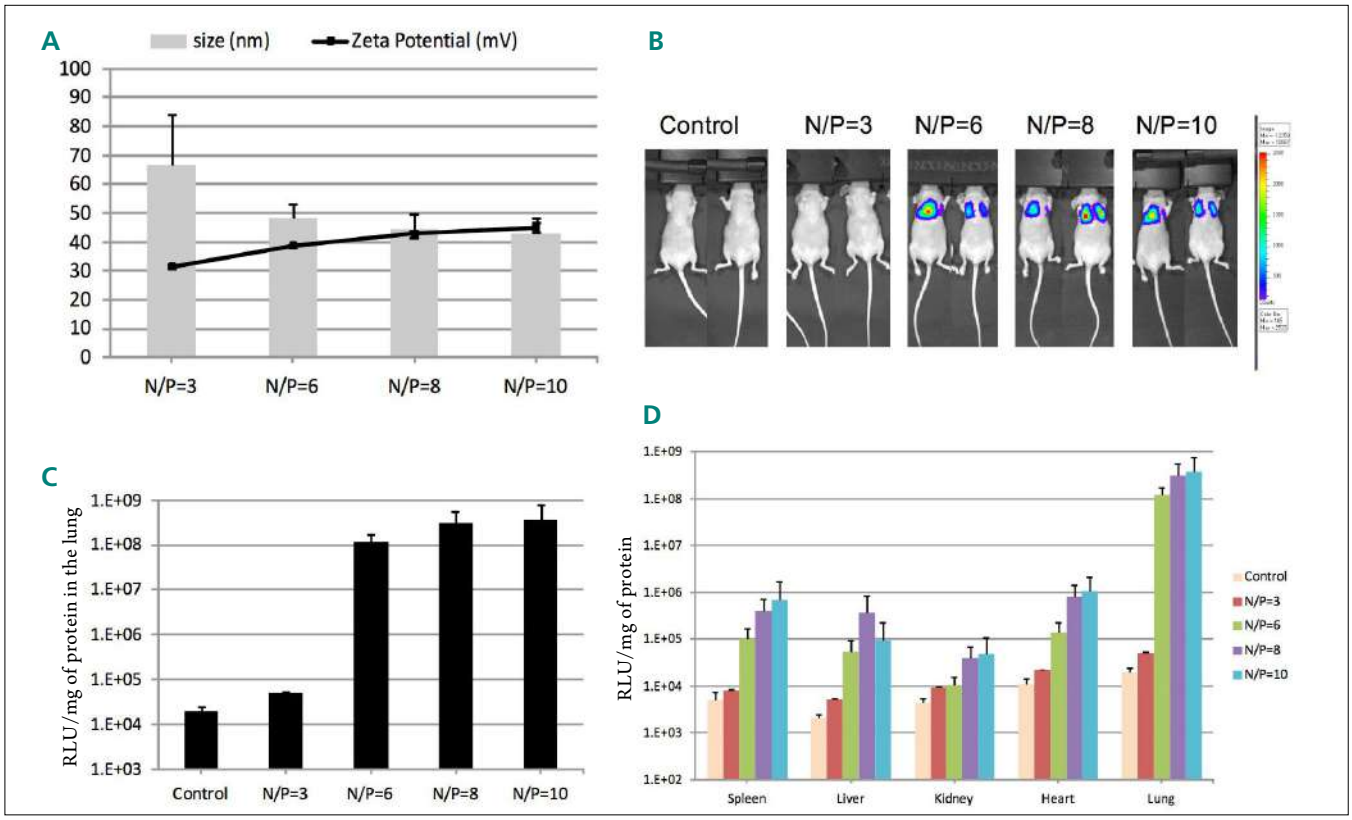

Figure 1. **Effect of nitrogen over phosphate ratio on delivery efficiency.** Forty micrograms of pCMVLuc plasmid were complexed with *in vivo*-jetPEI® at N/P ratio of 0 (control), 3, 6, 8 and 10. Thirty minutes after complexation, particle charge and zeta potential were measured using a zeta sizer (a). Complexes were injected retro-orbitally and mice were imaged with the IVIS100 imaging system 24 h after injection (exposition time 5 s) (b). After imaging, organs were removed and the luciferase level in each organ was analyzed in organ extracts using a luciferase assay and expressed relative to the amount of proteins (c and d), n=6.

Luciferase Expression Time Course in Lungs After Complex Injection

Once bound on the cell surface via interaction with the syndecan, *in vivo*-jetPEI®/DNA complexes are endocytosed into intracellular vesicles.[6] There, *in vivo*-jetPEI® acts as a "proton sponge" in the acidic environment of the lumen of endosomes.[1,7] Multiple protonations of *in vivo*-jetPEI® induce osmotic swelling followed by endosome rupture, leading to plasmid release into the cytoplasm.[8,9] *In vivo*-jetPEI® protects DNA against nucleases present in blood and serum.[10,11,12] Upon intravenous injection (tail vein or retro-orbital), the plasmid is quickly delivered in organs and expressed in cells. We investigated the time course of the luciferase expression in lungs using the PerkinElmer bioimaging system. As shown in Figure 2A, bioimaging of whole animals shows lung luciferase expression as early as 12 h after retro-orbital injection. In lungs, maximum expression is observed between 12 and 24 h after systemic injection (respectively 6.9 x 10^5 and 9.1 x 10^5 photons/s) (Figure 2A). Lungs were dissected after imaging, and the lung extracts were assayed for luciferase expression (Figure 2B). Again a good correlation was observed between the two techniques for detection of luciferase expression. The luciferase protein is not very stable and its life time is quite short.[13] Using a different reporter protein, such as eGFP or delivering a plasmid without CpG motives in order to avoid the silencing of gene expression over time[14] can increase transgene expression duration.

Complex Stability and Storage Temperature

We previously showed that *in vivo*-jetPEI® protects DNA from degradation by serum and blood nucleases.[10,11,12] As shown before, a small size of complexes is essential to promote efficient gene delivery *in vivo* (Figure 1). The complexes can be formed and then stored for many hours before their use if they are stable in size and do not form aggregates. We measured *in vivo*-jetPEI®/DNA complex sizes after 30 min complexation time or when stored 24 h at different temperatures (room temperature, 4 °C and 37 °C) by Dynamic Light Scattering. Figure 3A shows that *in vivo*-jetPEI®/DNA complexes are stable for at least 24 h at 4 °C, RT and 37 °C, as no variation of complex size was observed. Luciferase expression in the lungs was determined by bioimaging after storage of the complexes at 4 °C for 24 h and compared with complexes after 30 min complexation time. No significant variation of luciferase expression level was observed after 24 h storage (Figure 3B). Imaging was confirmed by luciferase assay in lung extracts (Figure 3C).

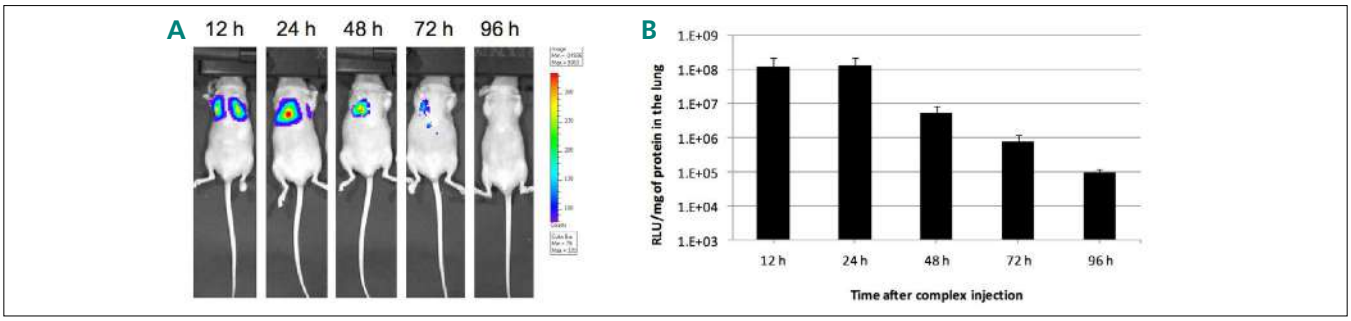

Figure 2. **Luciferase expression time course after *in vivo*-jetPEI®/DNA complex injection.** Forty micrograms of pCMVLuc complexed with *in vivo*-jetPEI® (N/P=8) were injected through the retro-orbital sinus. Mice were imaged 12, 24, 48, 72 and 96 h after complex injection using the IVIS100 imaging system (exposition time 10 s) (a). After injection, lungs were removed and luciferase expression was assayed in lung extracts (Figure 2b, luciferase expression in the lung), n=6.

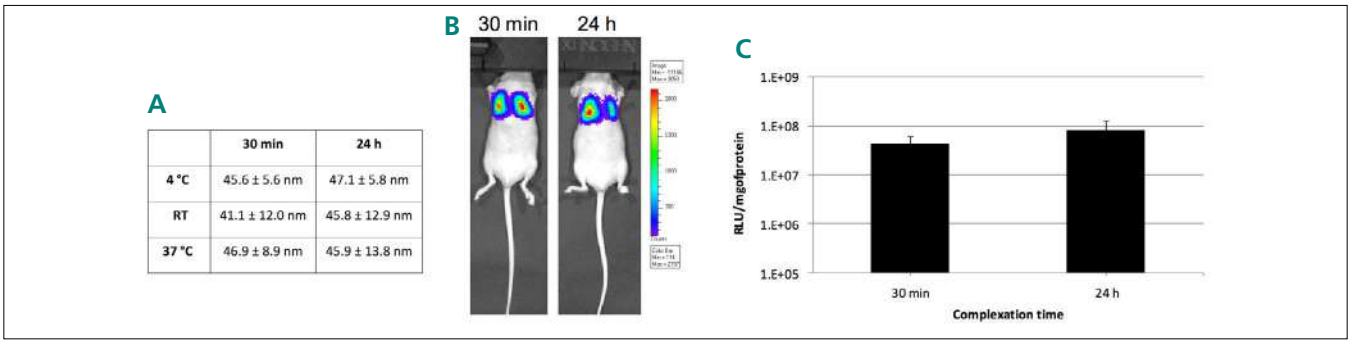

	30 min	24 h
4 °C	45.6 ± 5.6 nm	47.1 ± 5.8 nm
RT	41.1 ± 12.0 nm	45.8 ± 12.9 nm
37 °C	46.9 ± 8.9 nm	45.9 ± 13.8 nm

Figure 3. **Complex stability at different storage temperatures.** Forty micrograms of pCMVLuc were complexed with *in vivo*-jetPEI® (N/P=8). Complex size was determined after 30 min and 24 h storage at RT, 4 °C and 37 °C by Dynamic Light Scattering using a zeta sizer (a). For *in vivo* imaging, complexes incubated 30 min or stored 24 h at 4 °C were injected through the retro-orbital sinus. The animals were imaged with the IVIS100 imaging system 24 h after injection (exposition time 5 s) (b). After imaging, lungs were removed, luciferase expression in lung extracts was quantified and expressed relative to the amount of proteins (n = 6), Figure 3c.

Conclusion

In vivo-jetPEI®-mediated gene delivery is a very useful and easy-to-develop technology. Here we have shown that bioimaging is a perfectly complimentary tool to follow reporter gene expression, and improve gene delivery parameters in mice. The *in vivo* bioluminescence imaging systems developed by PerkinElmer are particularly suitable to follow plasmid expression upon delivery with *in vivo*-jetPEI®. This delivery technology can be adapted to target different organs using various routes of administration including systemic injection or local delivery routes like intra-tumoral, intra-thecal or subcutaneous.[2,10,14,15] Taken together our data showed, that *in vivo*-jetPEI® is a potent reagent for functional and therapeutic studies in animal models. As it is validated for non-viral gene therapy in humans, it is also a good candidate for human therapeutics.

Materials and Methods

Instrumentation

IVIS100 Xenogen system (PerkinElmer).

Reagents

Plasmid: pCMVLuc (Promega)

Transfection reagent: *in vivo*-jetPEI® (Polyplus-transfection)

Buffer: Glucose 10% (Polyplus-transfection)
D-luciferin potassium salt (PerkinElmer)

Table 1. **Complex preparation and injection.**

N/P	Volume of *in vivo*-jetPEI®
3	2.4 µL
6	4.8 µL
8	6.4 µL
10	8 µL

Complexes were prepared in 200 µL of glucose 5% final concentration. 40 µg DNA were diluted in 100 µL (final volume) of glucose 5% and mix by pipetting up and down. The appropriate amount of *in vivo*-jetPEI® (Table 1) was diluted in 100 µL (final volume) of glucose 5% and mix by vortexing. The diluted *in vivo*-jetPEI® solution was added to the diluted nucleic acid solution, mixed by vortexing and left for 30 min at RT before injection. For the complex stability experiments, the complexes were stored at different temperatures at this stage. Complexes were injected through the retro-orbital sinus within 2s.

NMRI Nude female 5-weeks old were obtained from Elevage Janvier and subjected to a week quarantine and acclimation period before use. Animals were maintained under conventional housing conditions (12 h light/12 h night, 22 °C). All animal studies were conducted in accordance to the French Animal Care guidelines and the protocols were approved by the Direction des Services Vétérinaires.

Bioluminescence imaging

For *in vivo* bioluminescence imaging, 150 mg/kg of D-luciferin potassium salt were injected i.p. to the mice. Mice were anesthetized 10 min after injection with isoflurane and imaged with an IVIS100 Xenogen system (PerkinElmer).

Complex charge and Zeta potential determination

Particle size and zeta potential were determined by Dynamic Light Scattering using a ZetaSizer Nano-ZS (Malvern Instrument) with the following specifications: medium viscosity, 1.036 centipoise (cP); refractive index (RI) medium, 1.337; RI particle, 1.47; Dielectric constant, 78.5; temperature, 25 °C.

Luciferase assay in organ extracts

For luciferase analysis in organ extracts, mice were sacrificed; organs were removed and quickly frozen. Organs were then homogenized with an ultra-thurax in appropriate volume (Table 2) of 1x lysis buffer (Promega) and frozen O/N at -80 °C. Lysates were centrifuged at 15,000 g for 5 min and luciferase activity was assessed by using 5 µL of lysate after addition of 100 µL of luciferin solution (Promega). Luciferase activity was normalized per mg of protein by using the BCA assay (Pierce).

Table 2.

Organ	Volume of Lysis Buffer (mL)
Spleen	1
Liver	2
Kidney	1
Heart	1
Lung	2

References

1. Boussif, O., Lezoualc'h, F., Zanta, M.A., Mergny, M.D., Scherman, D., Demeneix, B., and Behr, J.P. 1995. A versatile vector for gene and oligonucleotide transfer into cells in culture and in vivo: polyethylenimine. *Proc Natl Acad Sci USA* 92:7297-7301.

2. Demeneix, B., Behr, J., Boussif, O., Zanta, M.A., Abdallah, B., and Remy, J. 1998. Gene transfer with lipospermines and polyethylenimines. *Adv Drug Deliv Rev* 30:85-95.

3. Wightman, L., Kircheis, R., Rossler, V., Carotta, S., Ruzicka, R., Kursa, M., and Wagner, E. 2001. Different behavior of branched and linear polyethylenimine for gene delivery in vitro and in vivo. *J Gene Med* 3:362-372.

4. Wiseman, J.W., Goddard, C.A., McLelland, D., and Colledge, W.H. 2003. A comparison of linear and branched polyethylenimine (PEI) with DCChol/DOPE liposomes for gene delivery to epithelial cells in vitro and in vivo. *Gene Ther* 10:1654-1662.

5. Labat-Moleur, F., Steffan, A.M., Brisson, C., Perron, H., Feugeas, O., Furstenberger, P., Oberling, F., Brambilla, E., and Behr, J.P. 1996. An electron microscopy study into the mechanism of gene transfer with lipopolyamines. *Gene Ther* 3:1010-1017.

6. Kopatz, I., Remy, J.S., and Behr, J.P. 2004. A model for non-viral gene delivery: through syndecan adhesion molecules and powered by actin. *J Gene Med* 6:769-776.

7. Behr, J.P. 1996. [Gene transfer with amino lipids and amino polymers]. *C R Seances Soc Biol Fil* 190:33-38.

8. Kichler, A., Leborgne, C., Coeytaux, E., and Danos, O. 2001. Polyethylenimine-mediated gene delivery: a mechanistic study. *J Gene Med* 3:135-144.

9. Akinc, A., Thomas, M., Klibanov, A.M., and Langer, R. 2005. Exploring polyethylenimine-mediated DNA transfection and the proton sponge hypothesis. *J Gene Med* 7:657-663.

10. Lechardeur, D., Sohn, K.J., Haardt, M., Joshi, P.B., Monck, M., Graham, R.W., Beatty, B., Squire, J., O'Brodovich, H., and Lukacs, G.L. 1999. Metabolic instability of plasmid DNA in the cytosol: a potential barrier to gene transfer. *Gene Ther* 6:482-497.

11. Pollard, H., Remy, J.S., Loussouarn, G., Demolombe, S., Behr, J.P., and Escande, D. 1998. Polyethylenimine but not cationic lipids promotes transgene delivery to the nucleus in mammalian cells. *J Biol Chem* 273:7507-7511.

12. Pollard, H., Toumaniantz, G., Amos, J.L., Avet-Loiseau, H., Guihard, G., Behr, J.P., and Escande, D. 2001. Ca2+-sensitive cytosolic nucleases prevent efficient delivery to the nucleus of injected plasmids. *J Gene Med* 3:153-164.

13. Alvarado, M.C., Zsigmond, L.M., Kovacs, I., Cseplo, A., Koncz, C., and Szabados, L.M. 2004. Gene trapping with firefly luciferase in Arabidopsis. Tagging of stress-responsive genes. *Plant Physiol* 134:18-27.

14. de Wolf, H.K., Johansson, N., Thong, A.T., Snel, C.J., Mastrobattista, E., Hennink, W.E., and Storm, G. 2008. Plasmid CpG depletion improves degree and duration of tumor gene expression after intravenous administration of polyplexes. *Pharm Res* 25:1654-1662.

PerkinElmer, Inc.
940 Winter Street
Waltham, MA 02451 USA
P: (800) 762-4000 or
(+1) 203-925-4602
www.perkinelmer.com

PerkinElmer®

For a complete listing of our global offices, visit www.perkinelmer.com/ContactUs

Copyright ©2013, PerkinElmer, Inc. All rights reserved. PerkinElmer® is a registered trademark of PerkinElmer, Inc. All other trademarks are the property of their respective owners.

010877_01

APPLICATION NOTE

Stem Cells for Pre-clinical Imaging

Author

Vivek ShindePatil, Ph.D
Director, Technical Applications
In Vivo Imaging

PerkinElmer, Inc.
68 Elm Street
Hopkinton, MA USA

Stem Cell Research and Regenerative Medicine

Introduction

With the potential to treat a wide range of disease, from organ damage to congenital defects, stem cell research and tissue engineering form the underlying basis of regenerative medicine. Significant advances in the science of skin regeneration, for example, have now made it possible to develop and grow artificial skin grafts in a lab for treatment of burn victims. Other therapeutic applications include the use of stem cells to treat and repair central nervous system diseases such as ischemia and cerebral palsy, cardiovascular diseases, as well as autoimmune diseases including type I diabetes. However, critical research addressing safety concerns, exploring therapeutic function, and assessing mechanisms of action must be completed prior to human adoption. IVIS® technology is being widely used to explore stem cell research outcomes in preclinical small animal models, which serve as key test pre-cursors to human clinical trials.

PerkinElmer®
For the Better

Role for Optical Imaging

Optical imaging technology has emerged as an established tool to assess efficacy and treatment outcomes of cellbased therapeutics in preclinical models. The IVIS technology provides vital clues into the viability and behavior of stem cells post transplantation, aiding the prediction of how these cells might behave in humans. A representative sample of stem cell applications, out of more than 250 peer-reviewed citations, is outlined in the following pages. Below is a table showing the various stem cell and progenitor populations that have been imaged on the IVIS imaging system.

Different Stem Cell Types (Murine/Human)

- Embryonic Stem Cells[1, 2, 11-56]
- Neural Stem Cells[17, 18, 57-62]
- Mesenchymal Stem Cells[4, 5, 63-10]
- Hematopoietic Stem Cells[102-108]
- Muscle Stem Cells[19,109-111]
- Adipose-derived Stem Cells[96, 112, 113]

Progenitor Populations

- Different Stem Cell Types (Murine/Human)
- Embryonic Stem Cells[1, 2, 11-56]
- Neural Stem Cells[17, 18, 57-62]
- Mesenchymal Stem Cells[4, 5, 63-101]
- Hematopoietic Stem Cells[102-108]
- Cancer Stem Cells[126-138]

Labeling Strategies

Stem cells are required to be labeled with appropriate bioluminescent or fluorescent reporters to be imaged noninvasively in vivo. The following strategies for labeling stem cells with proteins and/or chemical conjugate dyes have previously been used with great success.

Applications

Characterization of stem cell behavior and homing patterns.

Stem cell therapies have been proposed as a putative treatment for arthritis, evidenced by clinical trials currently underway. Pre-clinical models often serve as a 'go' or 'no go' decision point, as potential therapies are often validated and characterized in murine models of disease prior to testing them in human subjects. Two critical points of characterization are their route of administration and their subsequent homing and localization into diseased tissue.

In this study by Sutton et al, featured in the Optics Express, December 2009 issue6, mesenchymal stem cells labeled with a fluorescent dye (DiD) were intra-peritoneally injected into athymic polyarthritic rats and shown to preferentially accumulate within arthritic ankle joints in vivo. The IVIS has served as a vital tool for imaging stem cell viability, migration and targeting of diseased tissue in various models[6, 29, 60, 72, 139, 140].

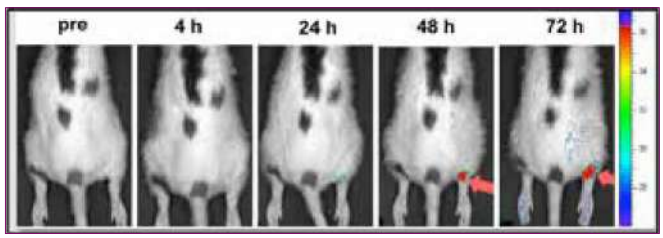

Figure 1. Imaging the accumulation if fluorescent mesenchymal stem cells in arthritic ankle joints (Sutton et al, Opt. Express, 17, p24403, 2009).

Assessment of safety and therapeutic potential in pre-clinical models

In 2009, the FDA cleared the way for the world's first clinical trial for embryonic stem cells in the context of spinal cord injury in the US141. Since then numerous such trials have been undertaken in other parts of the world with varying degrees of success. Due to the controversy widely surrounding embryonic stem cells, a new class of reprogrammed cells called 'induced pluripotent stem cells" (IPS) have received considerable attention in the past few years since they are derived from adult cell populations and known to retain stem cell properties and function. However, prior to their adoption in human therapy, rigorous testing of their therapeutic efficacy and safety in pre-clinical mouse models is warranted. The IVIS plays a key role in such pre-clinical evaluations of IPS and numerous other stem cell types[11, 13, 24, 37, 54, 58, 72, 78, 81, 96, 117, 121, 142-148].

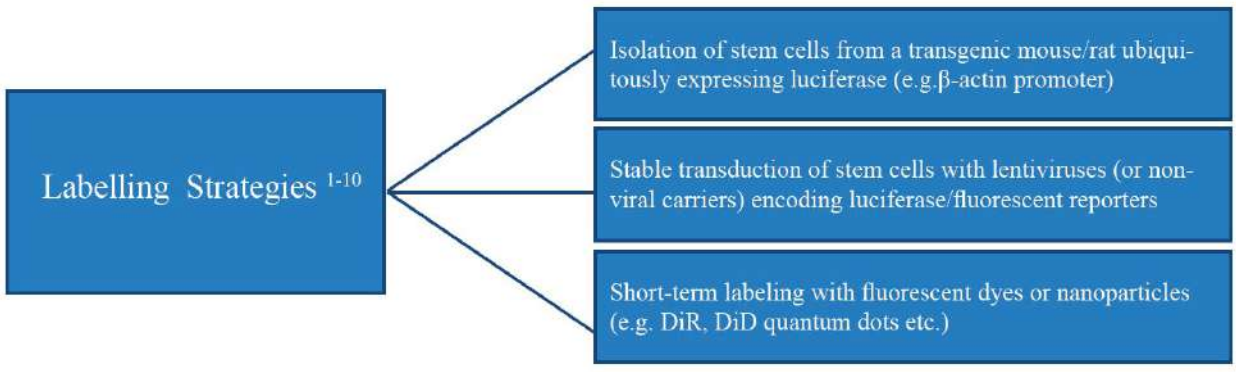

The example below is a 2010 report published by Tsuji et al in PNAS147 The researchers used IVIS to monitor the viability and therapeutic potential of IPS-derived neurospheres in a mouse model of spinal cord injury, suggesting that IPS can 'safely' promote locomotor function recovery in injured mouse models.

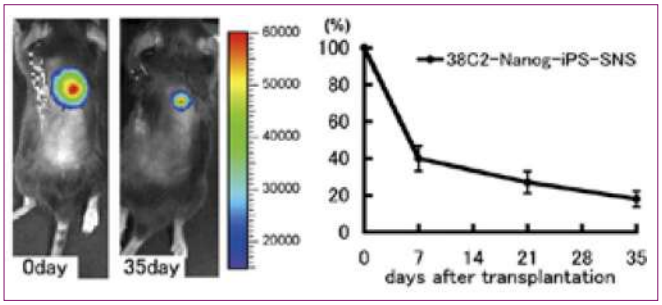

Figure 2. Imaging survival/viability of bioluminescent IPS-derived neurospheres in a mouse Model of spinal cord injury (Tsuji etal, PNAS. 107, p12704, 2010).

Exploration of molecular pathways and mechanisms of action.

Basic research that outlines key pathways and mechanisms by which stem cells survive, differentiate, migrate, and function are fundamental to our understanding of these cells14, 149, 150. The combination of novel optical reporters, creative molecular biology, and imaging with IVIS technology has facilitated such comprehensive insight into these questions. One vital aspect of hematopoietic stem cell research is identification and definition of their 'niche,' a bone marrow microenvironment that both houses and regulates these cells (and their fate).

In a fascinating 2009 report published in Nature, Xie et al9 used ex vivo high-resolution microscopy alongside non-invasive (IVIS) imaging to identify and further characterize the stem cell 'niche,' its function, and HSC recruitment.

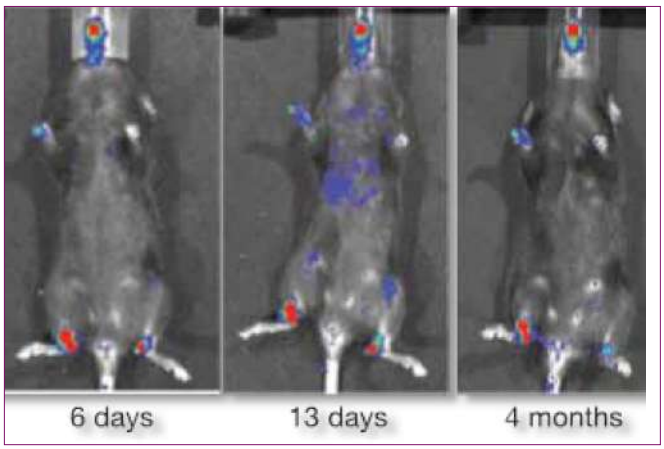

Figure 3. Bioluminescence imaging of hematopoietic stem cell recruitment to their niche in vivo, (Xie et al, Nature, 457, p97, 2009.

Identification and validation of complementary stem cell research technologies.

Several research areas including nanotechnology, biomaterials, and cell and tissue engineering complement stem cell research, and are equally invested in the promise of regenerative medicine. Collaborative developments in these fields have yielded biocompatible and biodegradable materials that coupled with growth factors and relevant biomolecules, provide the right 'scaffold' or environment to guide stem cells to form functional desired tissues or organs in vivo. Often, the survival and function of seeded cells, as well as interactions between the biomatrices and host tissues can be explored using the IVIS system [113, 116, 144, 151-156].

In a 2008 report published in PNAS154, Jennifer Elisseeff's group at Johns Hopkins University used a combination of chondrocyte-secreted morphogenetic factors and hydrogels to commit mesenchymal stem cells (derived from human embryonic stem cells) into a chrondrogenic lineage and eventually form cartilaginous tissue in mice. As seen in the figure below, they relied on IVIS imaging to validate the survival, viability and differentiation of MSCs seeded on a biodegradable polyester scaffold containing hydroxyapatite.

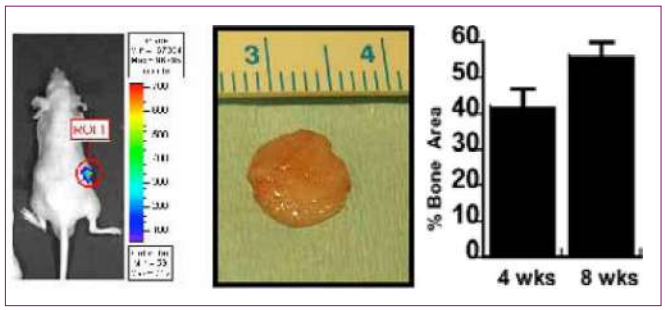

Figure 4. Imaging viability of bioluminescent mesenchymal stem cells seeded on a biodegradable scaffold (Hwang et al, PNAS, 105, p20641, 2008).

Conclusion

In summary, the IVIS is a valuable tool for stem cell research as it enables spatiotemporal and longitudinal monitoring of stem cell processes, cell viability and homing patterns, and therapeutic function in living animals. These preclinical readouts provide insightful cues to clinicians on the safety and efficacy of stem cell and regenerative medicine therapies to treat human disease.

References

1. Cao F, Drukker M, Lin S, Sheikh AY, Xie X, Li Z, Connolly AJ, Weissman IL, Wu JC. Molecular imaging of embryonic stem cell misbehavior and suicide gene ablation. Cloning and stem cells. 2007;9:107-117
2. Cao F, Lin S, Xie X, Ray P, Patel M, Zhang X, Drukker M, Dylla SJ, Connolly AJ, Chen X, Weissman IL, Gambhir SS, Wu JC. In vivo visualization of embryonic stem cell survival, proliferation, and migration after cardiac delivery. Circulation. 2006;113:1005-1014
3. Duda J, Karimi M, Negrin RS, Contag CH. Methods for imaging cell fates in hematopoiesis. Methods in molecular medicine. 2007;134:17-34
4. Spaeth EL, Dembinski JL, Sasser AK, Watson K, Klopp A, Hall B, Andreeff M, Marini F. Mesenchymal stem cell transition to tumor-associated fibroblasts contributes to fibrovascular network expansion and tumor progression. PLoS ONE. 2009;4:e4992
5. Spaeth EL, Marini FC. Dissecting mesenchymal stem cell movement: Migration assays for tracing and deducing cell migration. Methods in molecular biology. 2011;750:241-259
6. Sutton EJ, Boddington SE, Nedopil AJ, Henning TD, Demos SG, Baehner R, Sennino B, Lu Y, Daldrup-Link HE. An optical imaging method to monitor stem cell migration in a model of immune-mediated arthritis. Optics express. 2009;17:24403-24413

7. Sutton EJ, Henning TD, Pichler BJ, Bremer C, Daldrup-Link HE. Cell tracking with optical imaging. European radiology. 2008;18:2021-2032

8. Tolar J, Osborn M, Bell S, McElmurry R, Xia L, Riddle M, Panoskaltsis-Mortari A, Jiang Y, McIvor RS, Contag CH. Real-time in vivo imaging of stem cells following transgenesis by transposition. Molecular Therapy. 2005;12:42-48

9. Xie Y, Yin T, Wiegraebe W, He XC, Miller D, Stark D, Perko K, Alexander R, Schwartz J, Grindley JC, Park J, Haug JS, Wunderlich JP, Li H, Zhang S, Johnson T, Feldman RA, Li L. Detection of functional haematopoietic stem cell niche using real-time imaging. Nature. 2009;457:97-101

10. U shiki T, Kizaka-Kondoh S, Ashihara E, Tanaka S, Masuko M, Hirai H, Kimura S, Aizawa Y, Maekawa T, Hiraoka M. Noninvasive tracking of donor cell homing by near-infrared fluorescence imaging shortly after bone marrow transplantation. PLoS ONE. 2010;5

11. Barberi T, Bradbury M, Dincer Z, Panagiotakos G, Socci ND, Studer L. Derivation of engraftable skeletal myoblasts from human embryonic stem cells. Nat Med. 2007;13:642-648

12. Boddington SE, Henning TD, Jha P, Schlieve CR, Mandrussow L, DeNardo D, Bernstein HS, Ritner C, Golovko D, Lu Y, Zhao S, Daldrup-Link HE. Labeling human embryonic stem cell-derived cardiomyocytes with indocyanine green for noninvasive tracking with optical imaging: An fdacompatible alternative to firefly luciferase. Cell transplantation. 2010;19:55-65

13. Cao F, van der Bogt K, Sadrzadeh A, Xie X, Sheikh A, Wang H,Connolly A, Robbins R, Wu J. Spatial and temporal kinetics of teratoma formation from murine embryonic stem cell transplantation. Stem cells and development. 2007;16:883-892

14. Cao F, Wagner RA, Wilson KD, Xie X, Fu JD, Drukker M, Lee A, Li RA, Gambhir SS, Weissman IL, Robbins RC, Wu JC. Transcriptional and functional profiling of human embryonic stem cell-derived cardiomyocytes. PLoS ONE. 2008;3

15. Cao F, Xie X, Gollan T, Zhao L, Narsinh K, Lee RJ, Wu JC. Comparison of gene-transfer efficiency in human embryonic stem cells. Mol Imaging Biol. 2009

16. Chan KM, Raikwar SP, Zavazava N. Strategies for differentiating embryonic stem cells (esc) into insulin-producing cells and development of non-invasive imaging techniques using bioluminescence. Immunologic research. 2007;39:261-270

17. D aadi MM, Li Z, Arac A, Grueter BA, Sofilos M, Malenka RC, Wu JC, Steinberg GK. Molecular and magnetic resonance imaging of human embryonic stem cell-derived neural stem cell grafts in ischemic rat brain. Molecular therapy : the journal of the American Society of Gene Therapy. 2009;17:1282-1291

18. D aadi MM, Li Z, Arac A, Grueter BA, Sofilos M, Malenka RC, Wu JC, Steinberg GK. Molecular and magnetic resonance imaging of human embryonic stem cell–derived neural stem cell grafts in ischemic rat brain. Mol Ther. 2009;17:1282-1291

19. D arabi R, Santos FN, Filareto A, Pan W, Koene R, Rudnicki MA, Kyba M, Perlingeiro RC. Assessment of the myogenic stem cell compartment following transplantation of pax3/pax7-induced embryonic stem cell derived progenitors. Stem cells. 2011;29:777-790

20. D uan Y, Catana A, Meng Y, Yamamoto N, He S, Gupta S, Gambhir SS, Zern MA. Differentiation and enrichment of hepatocyte-like cells from human embryonic stem cells in vitro and in vivo. Stem Cells. 2007;25:3058-3068

21. E vseenko D, Schenke-Layland K, Dravid G, Zhu Y, Hao QL, Scholes J, Wang XC, Maclellan WR, Crooks GM. Identification of the critical extracellular matrix proteins that promote human embryonic stem cell assembly. Stem cells and development. 2009;18:919-928

22. Hendry SL, 2nd, van der Bogt KE, Sheikh AY, Arai T, Dylla SJ, Drukker M, McConnell MV, Kutschka I, Hoyt G, Cao F, Weissman IL, Connolly AJ, Pelletier MP, Wu JC, Robbins RC, Yang PC. Multimodal evaluation of in vivo magnetic resonance imaging of myocardial restoration by mouse embryonic stem cells. The Journal of thoracic and cardiovascular surgery. 2008;136:1028-1037 e1021

23. Huang NF, Niiyama H, De A, Gambhir SS, Cooke JP. Embryonic stem cell-derived endothelial cells for treatment of hindlimb ischemia. J Vis Exp. 2009

24. Huang NF, Niiyama H, Peter C, De A, Natkunam Y, Fleissner F, Li Z, Rollins MD, Wu JC, Gambhir SS, Cooke JP. Embryonic stem cell-derived endothelial cells engraft into the ischemic hindlimb and restore perfusion. Arteriosclerosis, thrombosis, and vascular biology. 2010;30:984-991

25. Hwang NS, Varghese S, Lee HJ, Zhang Z, Ye Z, Bae J, Cheng L, Elisseeff J. In vivo commitment and functional tissue regeneration using human embryonic stem cell-derived mesenchymal cells. Proceedings of the National Academy of Sciences of the United States of America. 2008;105:20641-20646

26. Kodama M, Tsukamoto K, Yoshida K, Aoki K, Kanegasaki S, Quinn G. Embryonic stem cell transplantation correlates with endogenous neurogenin 3 expression and pancreas regeneration in streptozotocin-injured mice. J Histochem Cytochem. 2009;57:1149-1158

27. Le U, Bom H, Moon S, Park K, Han H, Lee H, Song H, Min J. In vivo imaging of embryonic stem cell implantation into rat corpus caverno sum by using optical imaging system. J Nucl Med. 2007;48:327P

28. Lee AS, Tang C, Cao F, Xie X, van der Bogt K, Hwang A, Connolly AJ, Robbins RC, Wu JC. Effects of cell number on teratoma formation by human embryonic stem cells. Cell cycle (Georgetown, Tex. 2009; 8:2608-2612

29. Lee AS, Wu JC. Imaging of embryonic stem cell migration in vivo. Methods in molecular biology. 2011;750:101-114

30. Li Z, Suzuki Y, Huang M, Cao F, Xie X, Connolly AJ, Yang PC, Wu JC. Comparison of reporter gene and iron particle labeling for tracking fate of human embryonic stem cells and differentiated endothelial cells in living subjects. Stem Cells. 2008

31. Li Z, Wilson KD, Smith B, Kraft DL, Jia F, Huang M, Xie X, Robbins RC, Gambhir SS, Weissman IL, Wu JC. Functional and transcriptional characterization of human embryonic stem cell-derived endothelial cells for treatment of myocardial infarction. PLoS ONE. 2009;4

32. Li Z, Wu JC, Sheikh AY, Kraft D, Cao F, Xie X, Patel M, Gambhir SS, Robbins RC, Cooke JP, Wu JC. Differentiation, survival, and function of embryonic stem cell derived endothelial cells for ischemic heart disease. Circulation. 2007;116:I46-54

33. Linehan JL, Tian X, Morris JK, Kaufman DS. Improved analysis of hematopoietic engraftment by non-invasive in vivo bioluminescent imaging of transplanted human embryonic stem cell-derived hematopoietic cells. Blood. 2005;106:370A

34. Moon SH, Kim JS, Park SJ, Lee HJ, Do JT, Chung HM. A system for treating ischemic disease using human embryonic stem cell-derived endothelial cells without direct incorporation. Biomaterials. 2011;32:6445-6455

35. Narsinh KH, Cao F, Wu JC. Application of reporter gene imaging for studying human embryonic stem cells in living subjects. Viral applications of green fluorescent protein. 2009:13-32.

36. Priddle H, Grabowska A, Morris T, Clarke PA, McKenzie AJ, Sottile V, Denning C, Young L, Watson S. Bioluminescence imaging of human embryonic stem cells transplanted in vivo in murine and chick models. Cloning and stem cells. 2009;11:259-267

37. Raikwar SP, Zavazava N. Spontaneous in vivo differentiation of embryonic stem cell-derived pancreatic endoderm-like cells corrects hyperglycemia in diabetic mice. Transplantation. 2011;91:11-20

38. Sun N, Lee A, Wu JC. Long term non-invasive imaging of embryonic stem cells using reporter genes. Nature protocols. 2009;4:1192-1201

39. Suzuki Y, Zhang S, Kundu P, Yeung A, Robbins R, Yang P. In vitro comparison of the biological effects of three transfection methods for magnetically labeling mouse embryonic stem cells with ferumoxides. Magnetic Resonance in Medicine. 2007;57:1173-1179

40. Swijnenburg RJ, Schrepfer S, Cao F, Pearl JI, Xie X, Connolly AJ, Robbins RC, Wu JC. In vivo imaging of embryonic stem cells reveals patterns of survival and immune rejection following transplantation. Stem cells and development. 2008;17:1023-1029

41. Swijnenburg RJ, Schrepfer S, Govaert JA, Cao F, Ransohoff K, Sheikh AY, Haddad M, Connolly AJ, Davis MM, Robbins RC, Wu JC. Immunosuppressive therapy mitigates immunological rejection of human embryonic stem cell xenografts. Proceedings of the National Academy of Sciences of the United States of America. 2008;105:12991-12996

42. Takeshita F, Kodama M, Yamamoto H, Ikarashi Y, Ueda S, Teratani T, Yamamoto Y, Tamatani T, Kanegasaki S, Ochiya T, Quinn G. Streptozotocin- induced partial beta cell depletion in nude mice with out hyperglycaemia induces pancreatic morphogenesis in transplanted embryonic stem cells. Diabetologia. 2006;49:2948-2958

43. Teratani T, Yamamoto H, Aoyagi K, Sasaki H, Asari A, Quinn G, Terada M, Ochiya T. Direct hepatic fate specification from mouse embryonic stem cells. Hepatology (Baltimore, Md. 2005;41:836-846

44. Tian X, Hexum MK, Penchev VR, Taylor RJ, Shultz LD, Kaufman DS. Bioluminescent imaging demonstrates transplanted human embryonic stem cell-derived cd34(+) cells preferentially develop into endothelial cells. Stem Cells. 2009

45. Tian X, Woll PS, Morris JK, Linehan JL, Kaufman DS. Hematopoietic engraftment of human embryonic stem cell-derived cells is regulated by recipient innate immunity. Stem Cells. 2006:2005-0340

46. Wang S, Hu C, Zhu J. Transcriptional silencing of a novel htert reporter locus during in vitro differentiation of mouse embryonic stem cells Molecular Biology of the Cell. 2007;18:669-677

47. Wilber A, Linehan JL, Tian X, Woll PS, Morris JK, Belur LR, McIvor RS, Kaufman DS. Efficient and stable transgene expression in human embryonic stem cells using transposon-mediated gene transfer. Stem Cells. 2007;25:2919-2927

48. Wilson K, Yu J, Lee A, Wu JC. In vitro and in vivo bioluminescence reporter gene imaging of human embryonic stem cells. J Vis Exp. 2008

49. Wilson KD, Huang M, Wu JC. Bioluminescence reporter gene imaging of human embryonic stem cell survival, proliferation, and fate. Methods in molecular biology (Clifton, N.J. 2009;574:87-103

50. Woll PS, Grzywacz B, Tian X, Marcus RK, Knorr DA, Verneris MR, Kaufman DS. Human embryonic stem cells differentiate into a homogeneous population of natural killer cells with potent in vivo antitumor activity. Blood. 2009;113:6094-6101

51. Wu J, Spin J, Cao F, Lin S, Xie X, Gheysens O, Chen I, Sheikh A, Robbins R, Tsalenko A. Transcriptional profiling of reporter genes used for molecular imaging of embryonic stem cell transplantation. Physiological genomics. 2006;25:29

52. Wu JC, Li Z, Xu L, Giffard RG, Wu J, Cooke JP. Transplantation of embryonic stem cell derived endothelial cells promote functional recovery after cerebral ischemia. Circulation. 2006;114:627

53. Wu JC FCSDXXEKNCSGSMAJCMBEWW. Proteomic analysis of reporter genes for molecular imaging of transplanted embryonic stem cells. PROTEOMICS. 2006;9999:NA

54. Xie X, Cao F, Sheikh AY, Li Z, Connolly AJ, Pei X, Li RK, Robbins RC, Wu JC. Genetic modification of embryonic stem cells with vegf enhances cell survival and improves cardiac function. Cloning and stem cells. 2007;9:549-563

55. Yamada M, Gurney P, Chung J, Kundu P, Drukker M, Smith A, Weissman I, Nishimura D, Robbins R, Yang P. Manganese guided cellular mri of human embryonic stem cell and human bone marrow stromal cell viability. Magnetic Resonance in Medicine. 2009;62:1047-1054

56. Yu J, Huang NF, Wilson KD, Velotta JB, Huang M, Li Z, Lee A, Robbins RC, Cooke JP, Wu JC. Nachrs mediate human embryonic stem cell derived endothelial cells: Proliferation, apoptosis, and angiogenesis. PLoS ONE. 2009;4:e7040

57. Chen H, Ma H, Sytwu H, Wang H, Chen C, Liu S, Chen C, Chen H, Wang C. Neural stem cells secrete factors that promote auditory cell proliferation via a leukemia inhibitory factor signaling pathway. Journal of Neuroscience Research. 2010;88:3308-3318

58. D aadi MM, Davis AS, Arac A, Li Z, Maag AL, Bhatnagar R, Jiang K, Sun G, Wu JC, Steinberg GK. Human neural stem cell grafts modify microglial response and enhance axonal sprouting in neonatal hypoxic-ischemic brain injury. Stroke; a journal of cerebral circulation. 2010;41:516-523

59. Okada S, Ishii K, Yamane J, Iwanami A, Ikegami T, Katoh H, Iwamoto Y, Nakamura M, Miyoshi H, Okano HJ, Contag CH, Toyama Y, Okano H. In vivo imaging of engrafted neural stem cells: Its application in evaluating the optimal timing of transplantation for spinal cord injury. Faseb J. 2005

60. Pendharkar AV, Chua JY, Andres RH, Wang N, Gaeta X, Wang H, De A, Choi R, Chen S, Rutt BK, Gambhir SS, Guzman R. Biodistribution of neural stem cells after intravascular therapy for hypoxic-ischemia. Stroke; a journal of cerebral circulation. 2010;41:2064-2070

61. Sher F, van Dam G, Boddeke E, Copray S. Bioluminescence imaging of olig2-neural stem cells reveals improved engraftment in a demyelination mouse model. Stem Cells. 2009;27:1582-1591

62. Zhao D, Najbauer J, Garcia E, Metz MZ, Glackin CA, Kim SU, Aboody KS. Novel neural stem cell-mediated tumor selective gene therapy for breast cancer metastases. Molecular Therapy. 2009;17:S137

63. Andreeff M, Dembinski J, Hall BM, Studeny M, Ling X, Cabreira-Hansen M, Kate Sasser A, McQueen T, Lang F, Marini FC. Mesenchymal stem cells selectively engraft into tumor stroma and produce potent antitumor proteins in situ. Blood. 2006;108:109A

64. Battula V, Evans K, Hollier B, Shi Y, Marini F, Ayyanan A, Wang R, Brisken C, Guerra R, Andreeff M. Epithelial mesenchymal transition derived cells exhibit multi lineage differentiation potential similar to mesenchymal stem cells. Stem Cells. 2010;28:1435-1445

65. Beksac M, Kuzu I, Ozdemir M, Ayten M, Dalva K, Ucnullkan D,Kilicnull E, Attar A, Kanpolat Y. Tracking of donor type gren fluorescent and luciferase positive marrow mononuclear or mesenchymal stem cells in postmortem spinal cord histopathological sections for determination of regeneration in a spinal cord injury model. Haematologica. 2009;94:66

66. Cao XC, Wang B, Cong Y, Yan F. Human umbilical cord mesenchymal stem cell transplantation ameliorates inflammation in a mouse model of colitis. Gastroenterology. 2009;136:A406-A407

67. Chan J, Kumar S, Fisk NM. First trimester embryo-fetoscopic and ultra sound-guided fetal blood sampling for ex vivo viral transduction of cultured human fetal mesenchymal stem cells. Human reproduction (Oxford, England). 2008;23:2427-2437

68. Chanda D, Isayeva T, Kumar S, Hensel JA, Sawant A, Ramaswamy G, Siegal GP, Beatty MS, Ponnazhagan S. Therapeutic potential of adult bone marrow-derived mesenchymal stem cells in prostate cancer bone metastasis. Clin Cancer Res. 2009;15:7175-7185

69. Chen WH, Liu HY, Lo WC, Wu SC, Chi CH, Chang HY, Hsiao SH, Wu CH, Chiu WT, Chen BJ, Deng WP. Intervertebral disc regeneration in an ex vivo culture system using mesenchymal stem cells and platelet-rich plasma. Biomaterials. 2009;30:5523-5533

70. D euse T, Peter C, Fedak PW, Doyle T, Reichenspurner H, Zimmermann WH, Eschenhagen T, Stein W, Wu JC, Robbins RC, Schrepfer S. Hepatocyte growth factor or vascular endothelial growth factor gene transfer maximizes mesenchymal stem cell-based myocardial salvage after acute myocardial infarction. Circulation. 2009;120:S247-254

71. G erdoni E, Gallo B, Casazza S, Musio S, Bonanni I, Pedemonte E, Mantegazza R, Frassoni F, Mancardi G, Pedotti R, Uccelli A. Mesenchymal stem cells effectively modulate pathogenic immune response in experimental autoimmune encephalomyelitis. Annals of neurology. 2007;61:219-227

72. G ranero-Molto F, Weis JA, Miga MI, Landis B, Myers TJ, O'Rear L, Longobardi L, Jansen ED, Mortlock DP, Spagnoli A. Regenerative effects of transplanted mesenchymal stem cells in fracture healing. Stem Cells. 2009

73. G uillot P, Abass O, Bassett J, Shefelbine S, Bou-Gharios G, Chan J, Kurata H, Williams G, Polak J, Fisk N. Intrauterine transplantation of human fetal mesenchymal stem cells from first-trimester blood repairs bone and reduces fractures in osteogenesis imperfecta mice. Blood. 2008;111:1717

74. G uillot P, Cook H, Pusey C, Fisk N, Harten S, Moss J, Shore I, Bou-Gharios G. Transplantation of human fetal mesenchymal stem cells improves glomerulopathy in a collagen type ialpha2-deficient mouse. The Journal of pathology. 2008;214:627-636

75. Hakkarainen T, Särkioja M, Lehenkari P, Miettinen S, Ylikomi T, Suuronen R, Desmond R, Kanerva A, Hemminki A. Human mesenchymal stem cells lack tumor tropism but enhance the antitumor activity of oncolytic adenoviruses in orthotopic lung and breast tumors. Human Gene Therapy. 2007;18:627-641

76. Hata N, Shinojima N, Gumin J, Yong R, Marini F, Andreeff M, Lang FF. Platelet-derived growth factor bb mediates the tropism of human mesenchymal stem cells for malignant gliomas. Neurosurgery. 2010;66:144-156; discussion 156-147

77. Joo SY, Cho KA, Jung YJ, Kim HS, Park SY, Choi YB, Hong KM, Woo SY, Seoh JY, Ryu KH. Bioimaging to monitor the in vivo distribution of infused mesenchymal stem cells: In a mouse model of graft versus host disease. Cell Biology International. 2010

78. Kanazawa H, Fujimoto Y, Teratani T, Iwasaki J, Kasahara N, Negishi K, Tsuruyama T, Uemoto S, Kobayashi E. Bone marrow-derived mesenchymal stem cells ameliorate hepatic ischemia reperfusion injury in a rat model. PLoS ONE. 2011;6:e19195

79. Kidd S, Spaeth E, Dembinski JL, Dietrich M, Watson K, Klopp A, Battula L, Weil M, Andreeff M, Marini FC. Direct evidence of mesenchymal stem cell tropism for tumor and wounding microenvironments using in vivo bioluminescence imaging. Stem Cells. 2009

80. Klopp AH, Spaeth EL, Dembinski JL, Woodward WA, Munshi A, Meyn RE, Cox JD, Andreeff M, Marini FC. Tumor irradiation increases the recruitment of circulating mesenchymal stem cells into the tumor microenvironment. Cancer research. 2007;67:11687-11695

81. Kumar S, Wan C, Ramaswamy G, Clemens TL, Ponnazhagan S. Mesenchymal stem cells expressing osteogenic and angiogenic factors synergistically enhance bone formation in a mouse model of segmental bone defect. Mol Ther. 2010

82. Lien CY, Chih-Yuan Ho K, Lee OK, Blunn GW, Su Y. Restoration of bone mass and strength in glucocorticoid-treated mice by systemic transplantation of cxcr4 and cbfa-1 co-expressing mesenchymal stem cells. J Bone Miner Res. 2009;24:837-848

83. Ling X, Marini F, Konopleva M, Schober W, Shi Y, Burks J, Clise-Dwyer K, Wang R, Zhang W, Yuan X. Mesenchymal stem cells overexpressing ifn-inhibit breast cancer growth and metastases through stat3 signaling in a syngeneic tumor model. Cancer Microenvironment. 2010;3:1-13

84. Love Z, Wang F, Dennis J, Awadallah A, Salem N, Lin Y, Weisenberger A, Majewski S, Gerson S, Lee Z. Imaging of mesenchymal stem cell transplant by bioluminescence and pet. J Nucl Med. 2007; 48:2011-2020

85. Mader EK, Maeyama Y, Lin Y, Butler GW, Russell HM, Galanis E, Russell SJ, Dietz AB, Peng KW. Mesenchymal stem cell carriers protect oncolytic measles viruses from antibody neutralization in an orthotopic ovarian cancer therapy model. Clin Cancer Res. 2009;15:7246-7255

86. Marini F, Dembinski J, Studeny M, Zompetta C, Andreeff M. Mesenchymal stem cells as delivery systems for cancer therapy: Evaluation of tropism and efficacy. Molecular Therapy. 2005;11:S173

87. Marini FC, Dembinski JL, Studery M, Ling X, Zompetta C, Andreeff M. Mesenchymal stem cells selectively engraft into tumor stroma and confer potent antitumor activity. Cytotherapy. 2006;8:282

88. Martiniello-Wilks R, Larsen SR, Tiffen JC, Bailey CG, Rasko JEJ. Mesenchymal stem cells as suicide gene therapy vehicles for organ-confined and metastatic prostate cancer (pca). Blood. 2007;110:369B

89. Min JJ AY, Moon S, Kim YS, Park JE, Kim SM, Le UN, Wu JC, Joo SY, Hong MH, Yang DH, Jeong MH, Song CH, Jeong YH, Yoo KY, Kang KS, Bom HS. In vivo bioluminescence imaging of cord blood derived mesenchymal stem cell transplantation into rat myocardium. Annals of Nuclear Medicine. 2006;20:165-170

90. Morikawa S, Mabuchi Y, Kubota Y, Nagai Y, Niibe K, Hiratsu E, Suzuki S, Miyauchi-Hara C, Nagoshi N, Sunabori T, Shimmura S, Miyawaki A, Nakagawa T, Suda T, Okano H, Matsuzaki Y. Prospective identification, isolation, and systemic transplantation of multipotent mesenchymal stem cells in murine bone marrow. The Journal of experimental medicine. 2009;206:2483-2496

91. Park JS, Na K, Woo DG, Yang HN, Kim JM, Kim JH, Chung HM, Park KH. Non-viral gene delivery of DNA polyplexed with nanoparticles transfected into human mesenchymal stem cells. Biomaterials. 2010;31:124-132

92. Schrepfer S, Deuse T, Lange C, Katzenberg R, Reichenspurner H, Robbins R, Pelletier M. Simplified protocol to isolate, purify, and culture expand mesenchymal stem cells. Stem cells and development. 2007;16:105-108

93. Toegel F, Yang Y, Zhang P, Hu Z, Westenfelder C. Bioluminescence imaging to monitor the in vivo distribution of administered mesenchymal stem cells in acute kidney injury. American journal of physiology. 2008

94. Tolar J, Nauta AJ, Osborn MJ, Panoskaltsis Mortari A, McElmurry RT, Bell S, Xia L, Zhou N, Riddle M, Schroeder TM, Westendorf JJ, McIvor RS, Hogendoom PCW, Szuhai K, Oseth L, Hirsch B, Yant SR, Kay MA, Peister A, Prockop DJ, Fibbe WE, Blazar BR. Sarcoma derived from cultured mesenchymal stem cells. Stem Cells. 2006:2005-0620

95. U chibori R, Okada T, Ito T, Urabe M, Mizukami H, Kume A, Ozawa K. Retroviral vector-producing mesenchymal stem cells for targeted suicide cancer gene therapy. The journal of gene medicine. 2009;11:373-381

96. van der Bogt KE, Schrepfer S, Yu J, Sheikh AY, Hoyt G, Govaert JA, Velotta JB, Contag CH, Robbins RC, Wu JC. Comparison of transplantation of adipose tissue- and bone marrow-derived mesenchymal stem cells in the infarcted heart. Transplantation. 2009;87:642-652

97. Wang F, Dennis JE, Awadallah A, Solchaga LA, Molter J, Kuang Y, Salem N, Lin Y, Tian H, Kolthammer JA, Kim Y, Love ZB, Gerson SL, Lee Z. Transcriptional profiling of human mesenchymal stem cells transduced with reporter genes for imaging. Physiological genomics. 2008

98. Wang H, Cao F, De A, Cao Y, Contag C, Gambhir SS, Wu JC, Chen X. Trafficking mesenchymal stem cell engraftment and differentiation intumor-bearing mice by bioluminescence imaging. Stem Cells. 2009;27:1548-1558

99. Yeh SP, Lo WJ, Chang YC, Tsai WJ, Lin CL, Liao YM. Tumor homing activity of bone marrow-derived mesenchymal stem cell is highly various among different tumors on syngeneic mouse model using real-time in vivo imaging technique. Blood. 2009;114

100. Yong RL, Shinojima N, Fueyo J, Gumin J, Vecil GG, Marini FC, Bogler O, Andreeff M, Lang FF. Human bone marrow-derived mesenchymal stem cells for intravascular delivery of oncolytic adenovirus delta24-rgd to human gliomas. Cancer research. 2009;69:8932-8940

101. Zachos T, Diggs A, Weisbrode S, Bartlett J, Bertone A. Mesenchymal stem cell-mediated gene delivery of bone morphogenetic protein-2 in an articular fracture model. Mol Ther. 2007;15:1543-1550

102. Bastianutto C, Mian A, Symes J, Mocanu J, Alajez N, Sleep G, Shi W, Keating A, Crump M, Gospodarowicz M, Medin J, Minden M, Liu FF. Local radiotherapy induces homing of hematopoietic stem cells to the irradiated bone marrow. Cancer research. 2007;67:10112-10116

103. BitMansour A, Burns SM, Traver D, Akashi K, Contag CH, Weissman IL, Brown JM. Myeloid progenitors protect against invasive aspergillosis and pseudomonas aeruginosa infection following hematopoietic stem celltransplantation. Blood. 2002;100:4660-4667

104. G ao J, Li Y, Lu S, Wang M, Yang Z, Yan X, Zheng Y. Enhanced in vivo motility of human umbilical cord blood hematopoietic stem/progenitor cells introduced via intra-bone marrow injection into xenotransplantednod/scid mouse. Experimental hematology. 2009;37:990-997

105. Lin Y, Molter J, Lee Z, Gerson SL. Bioluminescence imaging of hematopoietic stem cell repopulation in murine models. Methods in molecular biology (Clifton, N.J. 2008;430:295-306

106. Wang X, Rosol M, Ge S, Petersen D, Kohn DB, Nelson MD, Crooks GM. Vivo bioluminescence imaging reveals the kinetics of human hematopoietic stem cell engraftment. Blood. 2003;102:939a

107. Wang X, Rosol M, Ge S, Peterson D, McNamara G, Pollack H, Kohn DB, Nelson MD, Crooks GM. Dynamic tracking of human hematopoietic stem cell engraftment using in vivo bioluminescence imaging. Blood. 2003;102:3478-3482

108. Zakrzewski JL, Kochman AA, Lu SX, Terwey TH, Kim TD, Hubbard VM, Muriglan SJ, Suh D, Smith OM, Grubin J, Patel N, Chow A, Cabrera-Perez J, Radhakrishnan R, Diab A, Perales MA, Rizzuto G, Menet E, Pamer EG, Heller G, Zuniga-Pflucker JC, Alpdogan O, van den Brink MR. Adoptive transfer of tcell precursors enhances t-cell reconstitution after allogeneic hematopoietic stem cell transplantation. Nat Med. 2006;12:1039-1047

109. Asakura A, Hirai H, Kablar B, Morita S, Ishibashi J, Piras BA, Christ AJ, Verma M, Vineretsky KA, Rudnicki MA. Increased survival of muscle stem cells lacking the myod gene after transplantation into regenerating skeletal muscle. Proceedings of the National Academy of Sciences of the United States of America. 2007;104:16552-16557

110. Nishijo K, Hosoyama T, Bjornson CR, Schaffer BS, Prajapati SI, Bahadur AN, Hansen MS, Blandford MC, McCleish AT, Rubin BP, Epstein JA, Rando TA, Capecchi MR, Keller C. Biomarker system for studying muscle, stem cells, and cancer in vivo. Faseb J. 2009

111. Sacco A, Doyonnas R, Kraft P, Vitorovic S, Blau HM. Selfrenewal and expansion of single transplanted muscle stem cells. Nature. 2008;456:502-506

112. Bai X, Yan Y, Song YH, Seidensticker M, Rabinovich B, Metzele R, Bankson JA, Vykoukal D, Alt E. Both cultured and freshly isolated adipose tissue-derived stem cells enhance cardiac function after acute myocardial infarction. European heart journal. 2009

113. Chang EI, Bonillas RG, El-Ftesi S, Chang EI, Ceradini DJ, Vial IN, Chan DA, Michaels Jt, Gurtner GC. Tissue engineering using autologous microcirculatory beds as vascularized bioscaffolds. Faseb J. 2008

114. D ickson PV, Hamner JB, Burger RA, Garcia E, Ouma AA, Kim SU, Ng CY, Gray JT, Aboody KS, Danks MK, Davidoff AM. Intravascular administration of tumor tropic neural progenitor cells permits targeted delivery of interferon-beta and restricts tumor growth in a murine model of disseminated neuroblastoma. J Pediatr Surg. 2007;42:48-53

115. Sims TL, Jr., Hamner JB, Bush RA, Williams RF, Zhou J, Kim SU, Aboody KS, Danks MK, Davidoff AM. Neural progenitor cell-mediated delivery of interferon beta improves neuroblastoma response to cyclophosphamide. Annals of surgical oncology. 2008;15:3259-3267

116. Kim KL, Han DK, Park K, Song SH, Kim JY, Kim JM, Ki HY, Yie SW, Roh CR, Jeon ES, Kim DK, Suh W. Enhanced dermal wound neovascularization by targeted delivery of endothelial progenitor cells using an rgd-g-plla scaffold. Biomaterials. 2009;30:3742-3748

117. Nguyen Huu S, Oster M, Uzan S, Chareyre F, Aractingi S, Khosrotehrani K. Maternal neoangiogenesis during pregnancy partly derives from fetal endothelial progenitor cells. Proceedings of the National Academy of Sciences of the United States of America. 2007;104:1871-1876

118. Highfill SL, Kelly RM, O'Shaughnessy MJ, Zhou Q, Xia L, Panoskaltsis-Mortari A, Taylor PA, Tolar J, Blazar BR. Multipotent adult progenitor cells can suppress graft-versus-host disease via prostaglandin e2 synthesis and only if localized to sites of allopriming. Blood. 2009;114:693-701

119. Tolar J, O'Shaughnessy MJ, Panoskaltsis-Mortari A, McElmurry RT, Bell S, Riddle M, McIvor RS, Yant SR, Kay MA, Krause D, Verfaillie CM, Blazar BR. Host factors that impact the biodistribution and persistence of multipotent adult progenitor cells. Blood. 2006:2005-2008-3289

120. Tolar J, Wang X, Braunlin E, McElmurry RT, Nakamura Y, Bell S, Xia L, Zhang J, Hu Q, Panoskaltsis-Mortari A, Zhang J, Blazar BR. The host immune response is essential for the beneficial effect of adult stem cells after myocardial ischemia. Experimental hematology. 2007;35:682-690

121. Li S, Tu Q, Zhang J, Stein G, Lian J, Yang PS, Chen J. Systemically transplanted bone marrow stromal cells contributing to bone tissue regeneration. Journal of cellular physiology. 2008;215:204-209

122. Abdel-Azim H, Zhu Y, Hollis R, Wang X, Ge S, Hao QL, Smbatyan G, Kohn DB, Rosol M, Crooks GM. Expansion of multipotent and lymphoidcommitted human progenitors through intracellular dimerization of mpl. Blood. 2008;111:4064-4074

123. Cao YA, Wagers AJ, Karsunky H, Zhao H, Reeves R, Wong RJ, Stevenson DK, Weissman IL, Contag CH. Heme oxygenase-1 deficiency leads to disrupted response to acute stress in stem cells and progenitors. Blood. 2008;112:4494-4502

124. Cheng JC, Kinjo K, Judelson D, Chang J, Wu WS, Schmid I, Shankar DB, Kasahara N, Stripecke R, Bhatia R, Landaw EM, Sakamoto KM. Creb is a critical regulator of normal hematopoiesis and leukemogenesis. Blood. 2007

125. Kim WI, Wiesner SM, Largaespada DA. Vav promoter-tta conditionaltransgene expression system for hematopoietic cells drives high level expression in developing b and t cells. Experimental hematology. 2007;35:1231-1239

126. Calabrese C, Poppleton H, Kocak M, Hogg TL, Fuller C, Hamner B, Oh EY, Gaber MW, Finklestein D, Allen M, Frank A, Bayazitov IT, Zakharenko SS, Gajjar A, Davidoff A, Gilbertson RJ. A perivascular niche for brain tumor stem cells. Cancer cell. 2007;11:69-82

127. Charafe-Jauffret E, Ginestier C, Iovino F, Tarpin C, Diebel M, Esterni B, Houvenaeghel G, Extra JM, Bertucci F, Jacquemier J, Xerri L, Dontu G, Stassi G, Xiao Y, Barsky SH, Birnbaum D, Viens P, Wicha MS. Aldehyde dehydrogenase 1-positive cancer stem cells mediate metastasis and poor clinical outcome in inflammatory breast cancer. Clin Cancer Res. 2010;16:45-55

128. Charafe-Jauffret E, Ginestier C, Iovino F, Wicinski J, Cervera N, Finetti P, Hur MH, Diebel ME, Monville F, Dutcher J, Brown M, Viens P, Xerri L, Bertucci F, Stassi G, Dontu G, Birnbaum D, Wicha MS. Breast cancer cell lines contain functional cancer stem cells with metastatic capacity and a distinct molecular signature. Cancer research. 2009;69:1302-1313

129. Chen L, Shen R, Ye Y, Pu XA, Liu X, Duan W, Wen J, Zimmerer J, Wang Y, Liu Y, Lasky LC, Heerema NA, Perrotti D, Ozato K, Kuramochi-Miyagawa S, Nakano T, Yates AJ, Carson IW, Lin H, Barsky SH, Gao JX. Precancerous stem cells have the potential for both benign and malignant differentiation. PLoS ONE. 2007;2

130. Conway AE, Lindgren A, Galic Z, Pyle AD, Wu H, Zack JA, Pelligrini M, Teitell MA, Clark A. A pluripotency and self-renewal program controls the expansion of genetically unstable cancer stem cells in pluripotent stem cell derived tumors. Stem Cells. 2008

131. E yler CE, Wu Q, Yan K, Macswords JM, Chandler-Militello D, Misuraca KL, Lathia JD, Forrester MT, Lee J, Stamler JS, Goldman SA, Bredel M, McLendon RE, Sloan AE, Hjelmeland AB, Rich JN. Glioma stem cell proliferation and tumor growth are promoted by nitric oxide synthase-2. Cell. 2011;146:53-66

132. G arzia L, Andolfo I, Cusanelli E, Marino N, Petrosino G, De Martino D, Esposito V, Galeone A, Navas L, Esposito S, Gargiulo S, Fattet S, Donofrio V, Cinalli G, Brunetti A, Vecchio LD, Northcott PA, Delattre O, Taylor MD, Iolascon A, Zollo M. Microrna-199b-5p impairs cancer stem cells through negative regulation of hes1 in medulloblastoma. PLoS ONE. 2009;4:e4998

133. G hods AJ, Irvin D, Liu G, Yuan X, Abdulkadir IR, Tunici P, Konda B, Wachsmann-Hogiu S, Black KL, Yu JS. Spheres isolated from 9l gliosarcoma rat cell line possess chemoresistant and aggressive cancer stem-like cells.Stem Cells. 2007;25:1645-1653

134. Hart LS, El-Deiry WS. Invincible, but not invisible: Imaging approaches toward in vivo detection of cancer stem cells. J Clin Oncol. 2008;26:2901-2910

135. Kang Y. Analysis of cancer stem cell metastasis in xenograft animal models. Cancer stem cells. 2008:7-19.

136. Kang Y. Analysis of cancer stem cell metastasis in xenograft animal models. Methods in molecular biology (Clifton, N.J. 2009;568:7-19

137. Murohashi M, Hinohara K, Kuroda M, Isagawa T, Tsuji S, Kobayashi S, Umezawa K, Tojo A, Aburatani H, Gotoh N. Gene set enrichment analysis provides insight into novel signalling pathways in breast cancer stem cells. British journal of cancer. 2010;102:206-212

138. Thorne SH, Contag CH. Integrating the biological characteristics of oncolytic viruses and immune cells can optimize therapeutic benefits of cell-based delivery. Gene therapy. 2008

139. Reumers V, Deroose CM, Krylyshkina O, Nuyts J, Geraerts M, Mortelmans L, Gijsbers R, Van den Haute C, Debyser Z, Baekelandt V. Noninvasive and quantitative monitoring of adult neuronal stem cell migration in mouse brain using bioluminescence imaging. Stem Cells. 2008;26:2382-2390

140. Steiner D, Gelovani J, Savoldo B, Robinson SN, Decker WK, Brouard N, Najjar A, Xing D, Yang H, Li S, Marini F, Zweidler-McKay PA, Bollard CM, Shpall EJ, Dotti G, Simmons PJ. Noninvasive bioluminescent imaging demonstrates long-term multilineage engraftment of ex vivo-expanded cd34-selected umbilical cord blood cells. Stem Cells. 2009

141. Pollack A. F.D.A. Approves a stem cell trial. New York Times. 2009

142. Cheng K, Li TS, Malliaras K, Davis DR, Zhang Y, Marban E. Magnetic targeting enhances engraftment and functional benefit of iron-labeled cardiosphere-derived cells in myocardial infarction. Circulation research. 2010;106:1570-1581

143. Lee SH, Hao E, Savinov AY, Geron I, Strongin AY, Itkin-Ansari P. Human beta-cell precursors mature into functional insulin-producing cells in an immunoisolation device: Implications for diabetes cell therapies.Transplantation. 2009;87:983-991

144. Levenberg S, Rouwkema J, Macdonald M, Garfein ES, Kohane DS, Darland DC, Marini R, van Blitterswijk CA, Mulligan RC, D'Amore PA, Langer R. Engineering vascularized skeletal muscle tissue. Nat Biotechnol. 2005;23:879-884

145. Martinez-Fernandez A, Nelson TJ, Yamada S, Reyes S, Alekseev AE, Perez-Terzic C, Ikeda Y, Terzic A. Ips programmed without c-myc yield proficient cardiogenesis for functional heart chimerism. Circulation research. 2009;105:648-656

146. Ransohoff KJ, Wu JC. Advances in cardiovascular molecular imaging for tracking stem cell therapy. Thromb Haemost. 2010;104:13-22

147. Tsuji O, Miura K, Okada Y, Fujiyoshi K, Mukaino M, Nagoshi N, Kitamura K, Kumagai G, Nishino M, Tomisato S, Higashi H, Nagai T, Katoh H, Kohda K, Matsuzaki Y, Yuzaki M, Ikeda E, Toyama Y, Nakamura M, Yamanaka S, Okano H. Therapeutic potential of appropriately evaluated safe-induced pluripotent stem cells for spinal cord injury. Proceedings of the National Academy of Sciences of the United States of America. 2010;107:12704-12709

148. van der Bogt KE, Sheikh AY, Schrepfer S, Hoyt G, Cao F, Ransohoff KJ, Swijnenburg RJ, Pearl J, Lee A, Fischbein M, Contag CH, Robbins RC, Wu JC. Comparison of different adult stem cell types for treatment of myocardial ischemia. Circulation. 2008;118:S121-129

149. Chimenti I, Smith RR, Li TS, Gerstenblith G, Messina E, Giacomello A, Marban E. Relative roles of direct regeneration versus paracrine effects of human cardiosphere-derived cells transplanted into infarcted mice. Circulation research. 2010

150. Leucht P, Kim JB, Amasha R, James AW, Girod S, Helms JA. Embryonic origin and hox status determine progenitor cell fate during adult bone regeneration. Development (Cambridge, England). 2008;135:2845-2854

151. Cao F, Sadrzadeh Rafie AH, Abilez OJ, Wang H, Blundo JT, Pruitt B, Zarins C, Wu JC. In vivo imaging and evaluation of different biomatrices for improvement of stem cell survival. J Tissue Eng Regen Med. 2007;1:465-468

152. F ujita A, Migita M, Ueda T, Ogawa R, Fukunaga Y, Shimada T. Hematopoiesis in regenerated bone marrow within hydroxyapatite scafold. Pediatric research. 2010;68:35-40

153. G iannoni P, Scaglione S, Daga A, Ilengo C, Cilli M, Quarto R. Short-time survival and engraftment of bone marrow stromal cells in an ectopic model of bone regeneration. Tissue Eng Part A. 2009

154. Hwang DW, Jang SJ, Kim YH, Kim HJ, Shim IK, Jeong JM, Chung JK, Lee MC, Lee SJ, Kim SU, Kim S, Lee DS. Real-time in vivo monitoring of viable stem cells implanted on biocompatible scaffolds. European journal of nuclear medicine and molecular imaging. 2008

155. Logeart-Avramoglou D, Oudina K, Bourguignon M, Delpierre L, Nicola MA, Bensidhoum M, Arnaud E, Petite H. In vitro and in vivo bioluminescent quantification of viable stem cells in engineered constructs. Tissue engineering. 2009

156. Martinez EC, Wang J, Gan SU, Singh R, Lee CN, Kofidis T. Ascorbic acid improves embryonic cardiomyoblast cell survival and promotes vascularizationin potential myocardial grafts in vivo. Tissue Eng Part A. 2010

PerkinElmer, Inc.
940 Winter Street
Waltham, MA 02451 USA
P: (800) 762-4000 or
(+1) 203-925-4602
www.perkinelmer.com

PerkinElmer®

For a complete listing of our global offices, visit www.perkinelmer.com/ContactUs

Copyright ©2013, PerkinElmer, Inc. All rights reserved. PerkinElmer® is a registered trademark of PerkinElmer, Inc. All other trademarks are the property of their respective owners.

011152_01

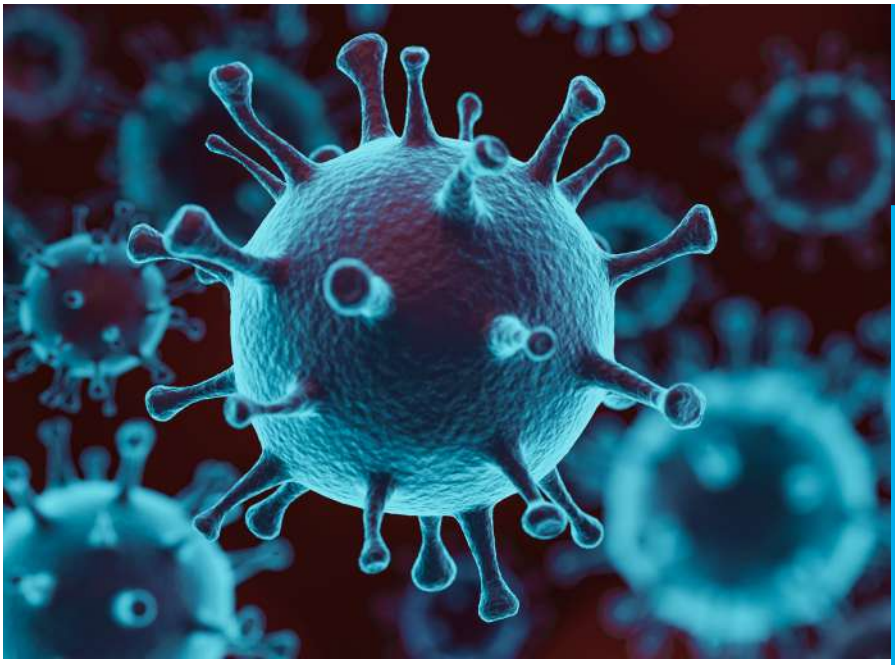

APPLICATION NOTE

Preclinical *In Vivo* Imaging

Author:

Jen-Chieh Tseng, Ph.D.

PerkinElmer, Inc.
Hopkinton, MA

Imaging Oncolytic Virus Infection in Cancer Cells

Abstract

The ultimate goal of a successful cancer treatment is to achieve selective targeting and effective killing of cancer cells without undesired harm to the surrounding normal tissues. Aside from the traditional small-molecule chemotherapeutics or targeted therapy agents that have been widely used in the clinic for decades, a new type of cancer therapeutics based on oncolytic viruses has recently gained attention in the field of research. Oncolytic viruses are genetically modified viruses capable of delivering therapeutic gene payload to cancer cells. A critical step for oncolytic virus development is to evaluate effectiveness against cancer and address safety concerns in living subjects. To illustrate this point, this application note provides an overview on using IVIS® optical imaging to assess and quantify oncolytic viral infection in living tumors and the subsequent virus-host interactions in real-time.

Although there are many different types of oncolytic viruses each having a different tumor-targeting mechanism, this application note highlights pre-clinical imaging results of Sindbis oncolytic virus to present a general approach when designing IVIS imaging studies for oncolytic virus research. Bioluminescent Sindbis pseudovirus (Sindbis/Fluc) was used to show successful tumor delivery and infection in several mouse tumor models. Since Sindbis/Fluc carries a bioluminescent firefly luciferase reporter gene, its infection and anti-cancer efficacy can be readily assessed by light production in tumors. The non-invasive aspect of IVIS imaging enables whole body imaging of viral infection and makes longitudinal imaging possible. Further, by imaging infection in transgenic/knockout mice with immune defects, this approach can be extended to study the immune/molecular aspect of viral-host interactions and thus address its potential safety concerns. Of note, this IVIS imaging strategy is not limited to Sindbis research and can be easily applied to other virus species. The latter part of this application note discusses potential IVIS fluorescent imaging applications to visualize host biological changes in response to viral infection.

PerkinElmer®
For the Better

Introduction

Viruses are infectious agents of small size and simple composition, consisting of genetic material (DNA or RNA) packaged within a protein or membrane enclosure. They are naturally evolved gene delivery vehicles, and their survival depends on using viral genetic information to hijack host cell molecular machinery and exploit its resources for viral particle reproduction. Based on a variety of wildtype viruses, oncolytic viruses are man-made pseudoviruses capable of delivering non-viral genes. In particular, they are engineered to achieve specific targeting and killing of cancer cells. This concept first emerged at the beginning of the twentieth century after a patient with myelogenous leukemia underwent complete tumor remission following influenza infection. This led to the investigation of a wide range of human virus species for their oncolytic potential, including adenoviruses, herpes simplex virus (type 1), measles virus, vascular stomatitis virus and Sindbis virus. After decades of cancer research and advances in molecular virology, many types of pseudoviruses have been developed to ensure selective infection and/or replication in cancer cells.

Although almost all human viruses can cause pathogenic conditions and can be considered harmful, there is a general strategy to convert them into much safer pseudoviruses for gene therapy. A typical viral genome, regardless of DNA or RNA, contains two types of gene cluster: structural and non-structural genes. As the name implies, structural genes encode proteins such as the capsid and envelope proteins that are building blocks of virion particles. Conversely, non-structural genes encode virus-specific enzymes such as replicase and protease required for genomic DNA or RNA replication and viral protein production, respectively. Taking advantage of this unique arrangement, researchers can produce a pseudovirus by replacing the structural gene cluster with a payload gene of interest. Thus, the resulting pseudovirus is capable of infecting cells and expressing the payload gene after infection, but it lacks essential structural genes for subsequent virion production.

This general strategy has been successfully applied to several virus species, and many types of oncolytic pseudoviruses have been developed for exogenous gene delivery. Nevertheless, it still remains a challenge to study their performance in living animal models. As viruses are infinitesimally small, direct and non-invasive detection in real-time is very difficult.

Fortunately, with a proper reporter gene as a payload, *in vivo* detection of a pseudovirus infection can be observed using a suitable molecular imaging techniques. For example, a firefly luciferase gene (Fluc) can be used as the reporter gene payload for detecting live infection events: Fluc expression resulting in efficient light production that can be detected through bioluminescence imaging. This approach makes it possible to longitudinally detect and quantify virus infection of host/tumor cells throughout the course of study in living subjects.

This application note shows how IVIS optical imaging was used to non-invasively study viral infection and virus-host interaction in real-time. In particular, oncolytic Sindbis virus was chosen for this purpose, since it has several unique features that make it an attractive oncolytic agent for cancer gene therapy and treatment. Originally identified in 1952, Sindbis virus is an arbovirus naturally transmitted via mosquito bites. Thus, Sindbis virus is capable of circulating in the blood stream for systemic delivery. For selective tumor targeting, Sindbis infection in mammalian cells is mediated by binding to the 67-Kda laminin receptor (LAMR) on plasma membrane. LAMR is known to be over-expressed in cancer cells and higher expression levels have been associated with poor prognosis in several human cancers. This particular fact gives Sindbis virus specific affinity to tumors. In mammalian cells, Sindbis infection is known to induce apoptosis, suggesting the virus could be used for eradicating cancer cells. For efficient gene delivery, a Sindbis pseudovirus system has been developed by replacing its structural genes. In this note, successful tumor delivery and infection were illustrated using a bioluminescent Sindbis pseudovirus carrying a firefly luciferase gene (Sindbis/Fluc). Several different types of mouse tumor models were used to demonstrate Sindbis' tumor targeting capability. Tumor bioluminescence closely correlates with viral infection levels and thus allows convenient and accurate assessment of Sindbis-related infection in living animals.

Results

In Vivo Imaging of Oncolytic Virus Infection in Tumors

Figure 1 summarizes the study design to evaluate Sindbis virus' tumor targeting capability in living animals. The goal was to demonstrate specific tumor targeting in living animals. To achieve this, a Sindbis pseudovirus carrying a firefly luciferase gene was used for IVIS imaging. Figure 1A illustrates a typical pseudoviral design of Sindbis virus. Wild type Sindbis virus has a positive-strand RNA genome with a 5′ cap and a 3′ poly-A tail. Its non-structural genes are on the 5′ side, followed by a subgenomic promoter (PSG) which is responsible for driving the structural genes downstream on the 3′ side. By replacing the structural gene cluster with a reporter gene, the resulting pseudovirus particle can be used to deliver a desired gene payload as its expression will be driven by a potent viral promoter. When a bioluminescent firefly luciferase gene (Fluc) is used, its successful infection and subsequent light production can be readily detected by the IVIS camera after concomitant luciferase substrate luciferin delivery.

Figure 1B outlines a simple study design to visualize Sindbis/Fluc infection in tumors. In this example, baby hamster kidney (BHK) cells were inoculated onto the mammary fat pads in immunocompromised SCID mice. BHK cells have a high level of LAMR expression and are highly sensitive to Sindbis infection. After tumor was established, mice received daily i.v. injections of Sindbis/Fluc starting on Day 0. Figure 1C shows longitudinal imaging results on a tumor-bearing mouse. Tumor-specific bioluminescence was observed as early as Day 1 and gradually increased during the first nine days of imaging. Luciferin was injected prior to each *in vivo* bioluminescence imaging (BLI) timepoint.

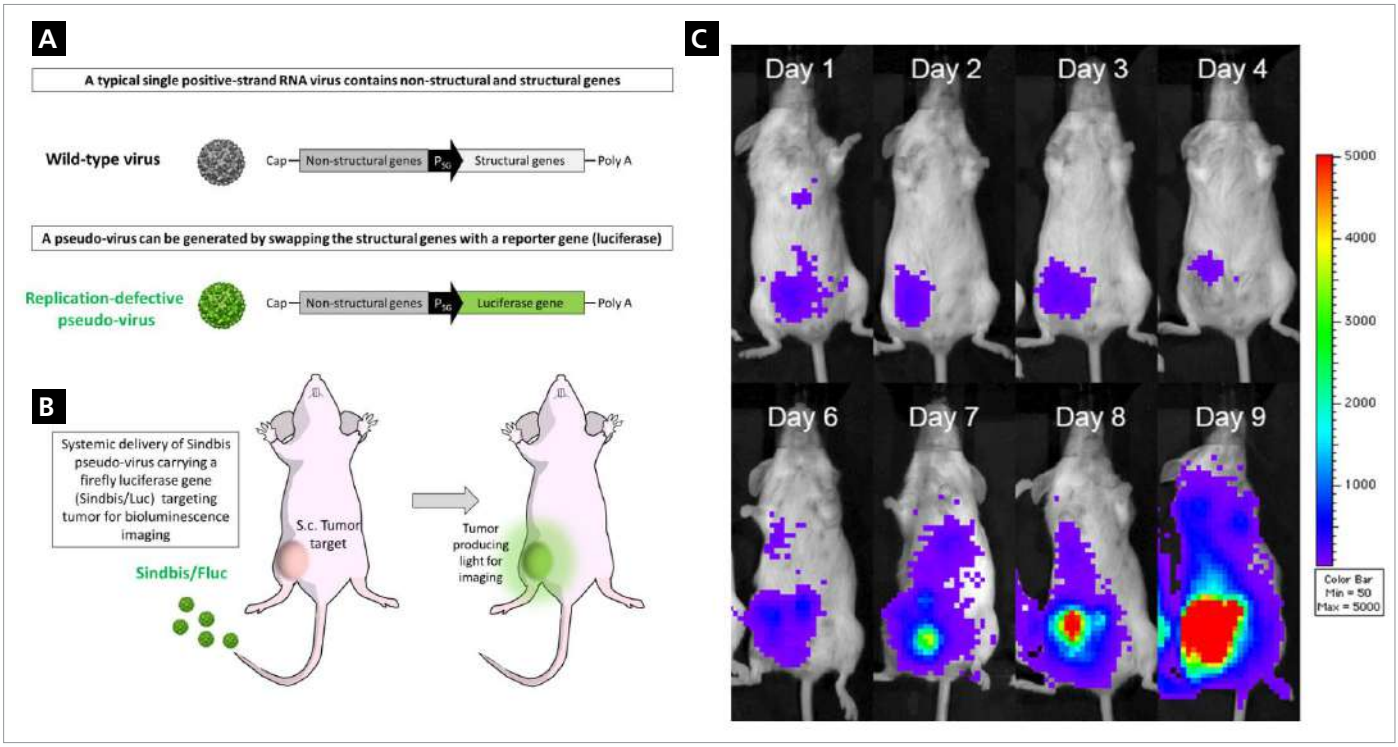

Figure 1. Study design and bioluminescence imaging using IVIS to visualize Sindbis infection in tumors.

Specific Targeting and Infection in Spontaneous Tumors

Although the previous results shows strong affinity of Sindbis virus to BHK tumors, its preferential tumor infection may be due to underlying species difference between hamster (BHK tumor) and mouse (host). As discussed, BHK cells have a high level of LAMR expression and thus it is not surprising that the tumors are highly susceptible to Sindbis infection. To ensure the virus' selective affinity is truly due to their preference to cancer cells, a spontaneous and immunocompetent mouse tumor model was tested.

Figure 2A illustrates such imaging study design. In particular, the MSV-*RGR/p15*$^{+/-}$ transgenic mice are heterozygous for the *Rgr* oncogene and for the *Cdkn2b* gene, also known as *p15(Ink4b)*. These mice typically develop spontaneous fibrosarcoma in the paws or tails. Because these tumor are not artificially implanted or injected, they closely mimic the physiological development of cancer. In this particular example, a mouse with a tumor growing on its right hind foot received daily i.p. treatments of Sindbis/Fluc for three consecutive days prior to bioluminescence imaging. All viral injections were done in the peritoneal cavity to be as distant as possible from the tumor site.

Figure 2B shows the imaging results after three consecutive Sindbis daily treatments. The photograph image shows a fibrosarcoma tumor on the right hind foot, while the image overlay with bioluminescence signals clearly shows tumor-specific targeting. As the Sindbis/Fluc pseoduvirus particles accumulated in the fibrosarcoma tumor, specific bioluminescence signals in the foot tumor indicated the virus is capable of targeting tumors that arise spontaneously while avoid normal tissues. Notably, in this particular model, only mouse cells are involved whether they are normal or tumor. Of note, the immune system seems not to diminish its ability to reach and infect tumor cells during the first couple days of treatments.

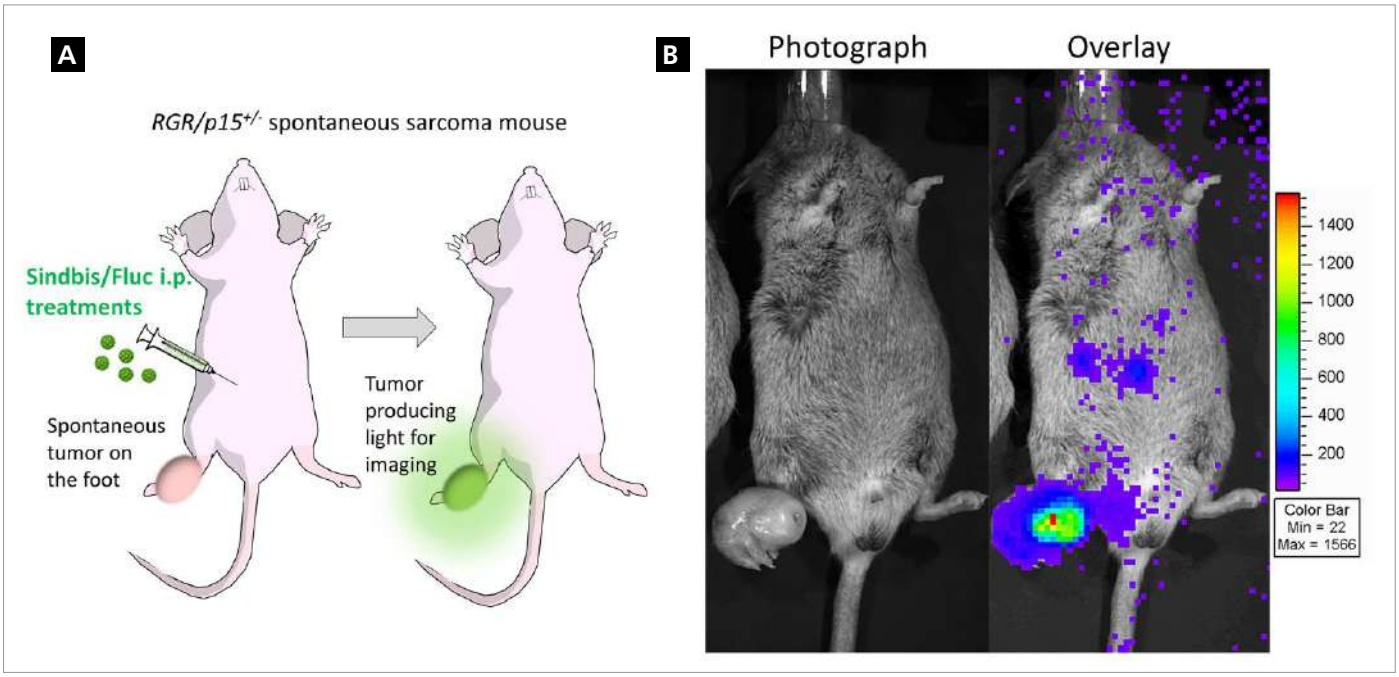

Figure 2. Sindbis virus specifically infects spontaneous fibrosarcoma in a transgenic mouse. Imaged on the IVIS system.

Specific Targeting of Metastatic Ovarian Cancer in the Peritoneal Cavity

With the success of targeting localized solid tumors, the researchers then turned their attention to metastatic cancers. In the following example (Figure 3), an advanced mouse ovarian cancer model was used to evaluate Sindbis' capability to target small, disseminated, and microscopic ovarian cancer nodules in the peritoneal cavity. The model was established by i.p. inoculation of mouse MOSEC ovarian cancer cells into C57BL/6 mice (Figure 3A). Four weeks after cancer cell inoculation, tumor-bearing mice received a single Sindbis/Fluc i.p. treatment. As reference, a tumor-free control mouse was also i.p. treated with Sindbis/Fluc and imaged the day after. Figure 3B shows the imaging results. Interestingly, tumor-free control mouse (left panel) showed no detectable Sindbis/Fluc infection while the tumor-bearing mouse (right panel) showed significant and wide-spread infection BLI signals in the peritoneal cavity. To validate specific Sindbis/Fluc tumor infection, various organs in the peritoneal cavity were harvested and imaged *ex vivo*. A good correlation of positive Sindbis infection and presence of tumor nodule was observed (Figure 3B, red arrows). This result was further validated by conventional histological, microscopic imaging (data shown in the original publication Ref 2).

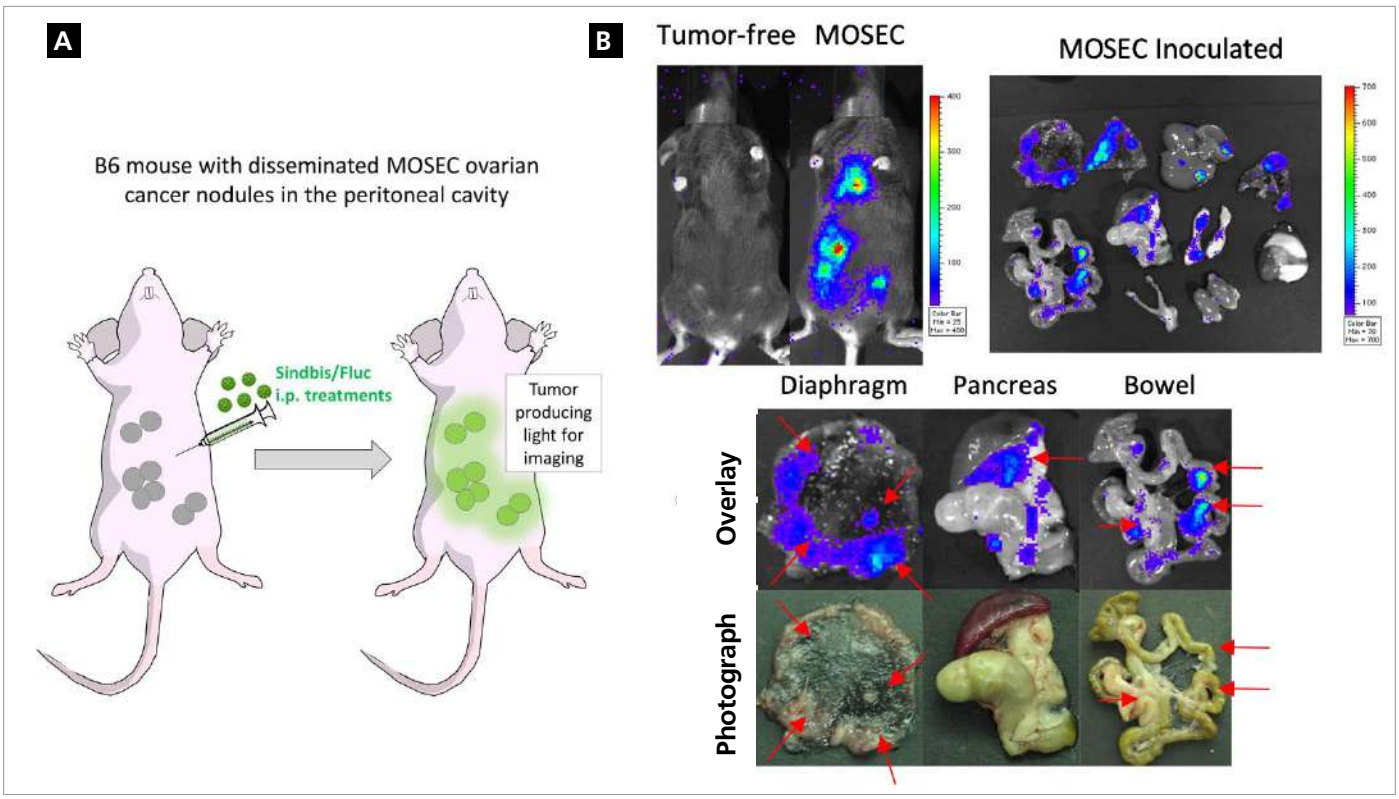

Figure 3. Sindbis specifically targets small, metastatic ovarian cancer in the peritoneal cavity.

Quantitative Imaging of Sindbis Treatment Efficacy

As Sindbis infection is known to induce apoptosis and kill the infected mammalian cells, the next step was to determine if repeated Sindbis treatments have any anti-cancer efficacy. Figure 4A illustrates a study design using the human ES-2/Fluc ovarian cancer cells which, after i.p. inoculation, were capable of establishing tumor nodules on the surface of various organs in the peritoneal cavity. As the cell carries the reporter firefly luciferase gene, its growth and spreading can be easily monitored using IVIS imaging. The bioluminescence imaging (BLI) signal levels directly correlated with tumor burden in the peritoneal cavity. In addition, to enhance its tumor suppression capability, immune-stimulating IL-12 or IL-15 gene was introduced into the Sindbis pseudovirus construct. As a reference, a pseudovirus carrying the bacterial β-galactosidase LacZ gene was used. In this particular study, ES2/Fluc cells ($1.5x10^6$) were i.p. inoculated into female SCID mice on Day 0 and daily i.p. Sindbis treatments began the Day after (Day 1).

Figure 4B shows the BLI imaging results of ES2/Fluc tumor load on Day 13 (after 12 consecutive treatments) and quantitative representation of BLI tumor signals for up to Day 20. Control mice did not receive any pseudovirus treatment. Total whole body photon counts were determined by IVIS imaging on days 1, 5, 13 and 20 to assess disease progression of ES2/Fluc metastases. Without any anti-cancer cytokine, the Sindbis/LacZ pseudovirus is sufficient to suppressed cancer growth when compared with the untreated control mice. The use of either IL-12 or IL-15 cytokine gene further enhanced the tumor-suppressing activity of Sindbis virus. In both cases, more than 95% growth suppression was observed in cytokine viruses within five days of treatment.

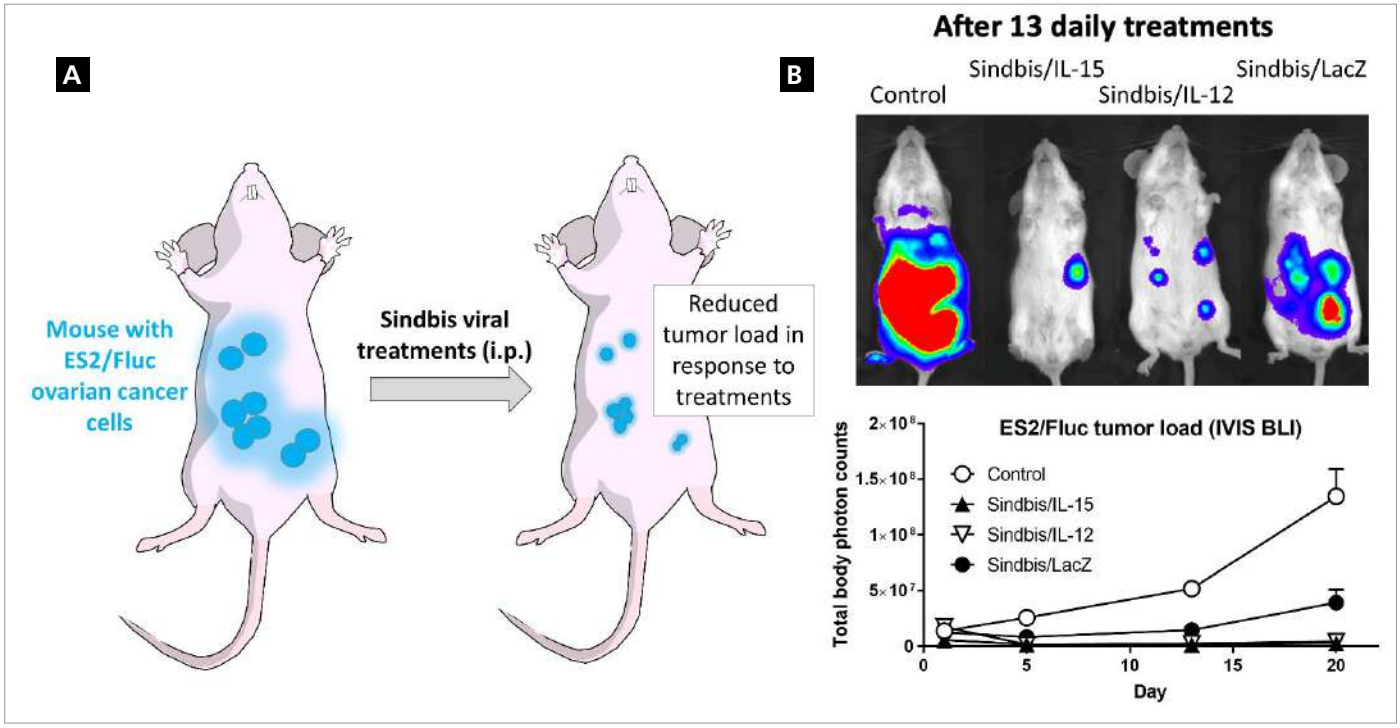

Figure 4. Repeated Sindbis treatments suppress ovarian cancer growth.

Type I Interferons Protect Liver From Sindbis Infection

For downstream clinical development, safety is of great importance and therefore warranted further investigation. In particular, the viral interaction with the host immune systems during repeated treatments was an important consideration. The data suggest that consecutive and repeated treatments of replication-defective Sindbis pseudovirus are safe for animals, and part of the reason could be the innate anti-viral immunity which protects normal tissue from infection. Since mammalian interferons (IFNs) play pivotal roles in antiviral responses, mice with genetic defects in either Type 1 (alpha/beta) or Type 2 (gamma) IFN pathways were used to determine if IFNs play any roles in protecting normal tissues from Sindbis infection.

The BLI imaging results in Figure 5 clearly indicates that the type 1 IFNs protect normal tissues from Sindbis infection. When Sindbis/Fluc was i.p. delivered into mice lacking either functional type 1 IFN-α/β receptor or its downstream transducer STAT1, significant liver infection was observed within 24 hours (Figure 5A). The liver infection was confirmed when the peritoneal organs were exposed and examined by IVIS BLI imaging (Figure 5B, red arrow). In some cases, a lower infection level present in the abdomen fat (Figure 5B, yellow arrow), irrelevant to its IFN-γ status. The imaging data indicate that type 2 IFN does not confer protection against Sindbis infection since no BLI signal was observed in the liver of IFN-γ knock-out mice (Figure 5C).

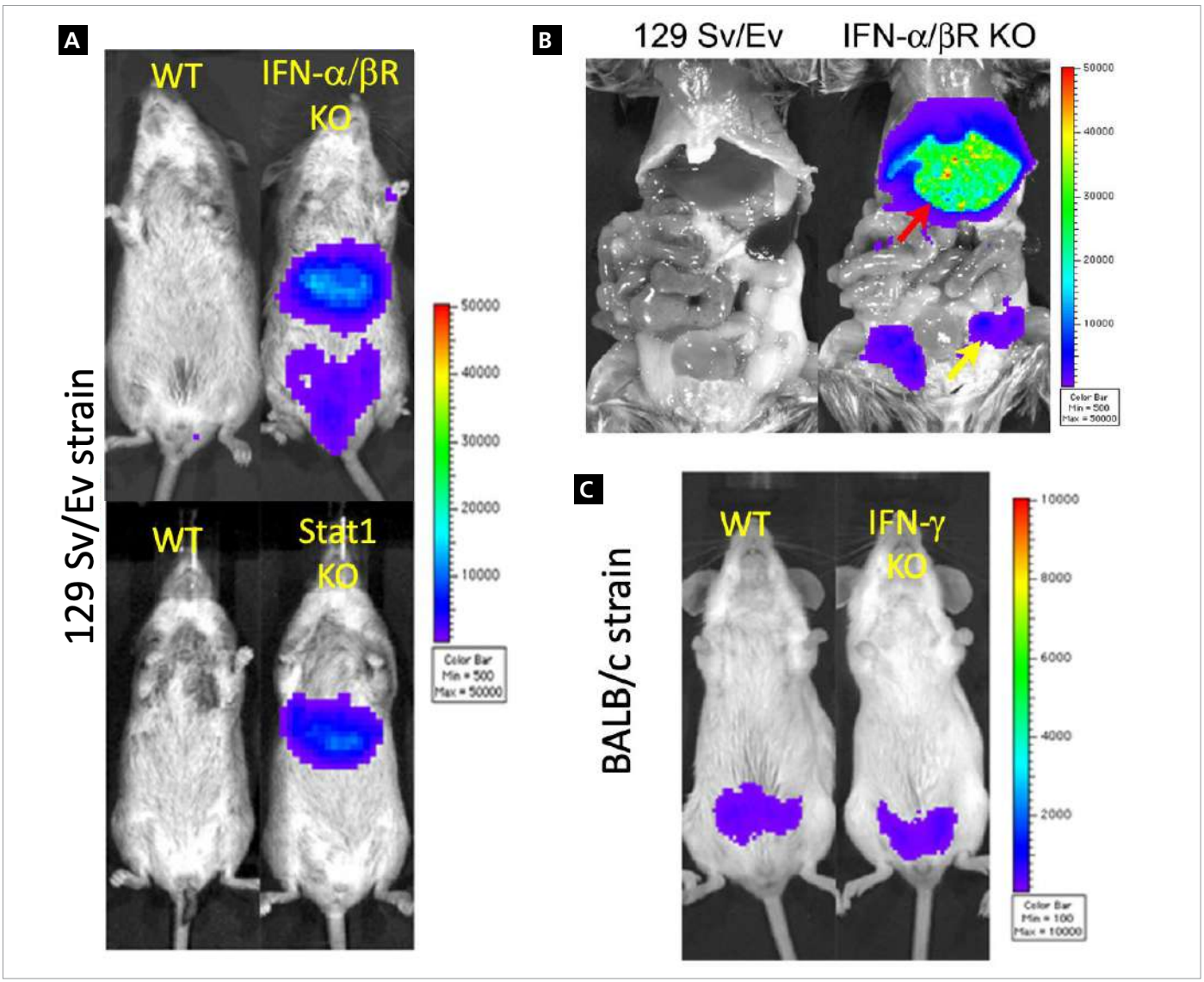

Figure 5. Type 1 interferon protect mouse liver from Sindbis infection.

Discussion

The imaging results presented in this application note demonstrate the value of optical imaging using the IVIS platform for visualizing virus infection non-invasively in living subjects. By imaging different types of tumor models and animals with well-characterized immune defects, these *in vivo* observations provide important insights into Sindbis' virus-host interaction and its therapeutic implications. Importantly, the bioluminescent imaging strategy illustrated here can easily be translated to other types of viruses, given most viruses' small genome sizes and recent advancements in genetic modification techniques. Furthermore, the IVIS imaging platform is versatile, and researchers are not limited to bioluminescent reporter genes when designing a pesudovirus imaging strategy. As most IVIS imaging systems are equipped with red and near-infrared (NIR) fluorescence imaging capability, they can also be used to visualize fluorescent reporter expression in living animals. One advantage of fluorescence protein imaging is that it does not require any substrate to produce imaging signals. By choosing a suitable fluorescent reporter gene, specific viral infection and fluorescent protein expression in tumors can be readily visualized using the IVIS imaging system in study designs similar to those demonstrated in this application note. Table 1 lists the bioluminescent and fluorescent reporter genes that are compatible with the IVIS platform.

In addition to direct imaging of viral infection using bioluminescence imaging, IVIS systems can be used to study viral-host interaction by using a variety of NIR fluorescent imaging agents. Table 2 lists several NIR fluorescent imaging agents developed by PerkinElmer that can be used in conjunction for imaging physiological changes and host responses during/after viral infection. In addition to complimenting bioluminescence imaging, a unique advantage of fluorescence imaging is the ability to multiplex more than one fluorescent probe providing a wealth of information on host's biological responses to viruses.

Table 1. Reporter genes suitable for IVIS imaging of infection/replication events.

Bioluminescence	Firefly luciferase; Renilla luciferase; click beetle luciferase.	Highly sensitivity and with low background, but all require corresponding substrates for light production.
Fluorescence	Red fluorescent protein (RFP); DsRed and its variants (e.g. mFruits: mCherry, mOrange, mRaspberry).	Less sensitive and with higher background, but with no need for substrate to establish signals.

Table 2. NIR fluorescent imaging agents for imaging host responses to viral infection

Angiogenesis and vascular leakiness for virus delivery.	AngioSense 680 EX or 750 EX; AngioSpark 750; Superhance 750; TLectinSense 680.
Inflammation caused by virus or secondary infection.	ProSense 680, 750 EX or 750 FAST; MMPSense 680, 645 FAST or750 FAST; Cat B 680 FAST or 750 FAST; Cat K 680 FAST.
Apoptosis induced by viral infection or tissue damage.	Annexin *Vivo* 750.

References

1. Tseng JC, Levin B et al. Systemic tumor targeting and killing by Sindbis viral vectors. *Nat Biotechnol.* 2004 Jan;22(1):70-7.
2. Tseng JC, Hurtado A et al. Using Sindbis Viral Vectors for Specific Detection and Suppression of Advanced Ovarian Cancer in Animal Models. *Cancer Res.* 2004 Sep 15;64(18):6684-92.
3. Tseng JC, Zheng Y et al. Restricted Tissue Tropism and Acquired Resistance to Sindbis Viral Vector Expression in the Absence of Innate and Adaptive Immunity. *Gene Ther.* 2007 Aug;14(15):1166-74.

PerkinElmer, Inc.
940 Winter Street
Waltham, MA 02451 USA
P: (800) 762-4000 or
(+1) 203-925-4602
www.perkinelmer.com

PerkinElmer®

For a complete listing of our global offices, visit www.perkinelmer.com/ContactUs

Copyright ©2020, PerkinElmer, Inc. All rights reserved. PerkinElmer® is a registered trademark of PerkinElmer, Inc. All other trademarks are the property of their respective owners.

103134 PKI

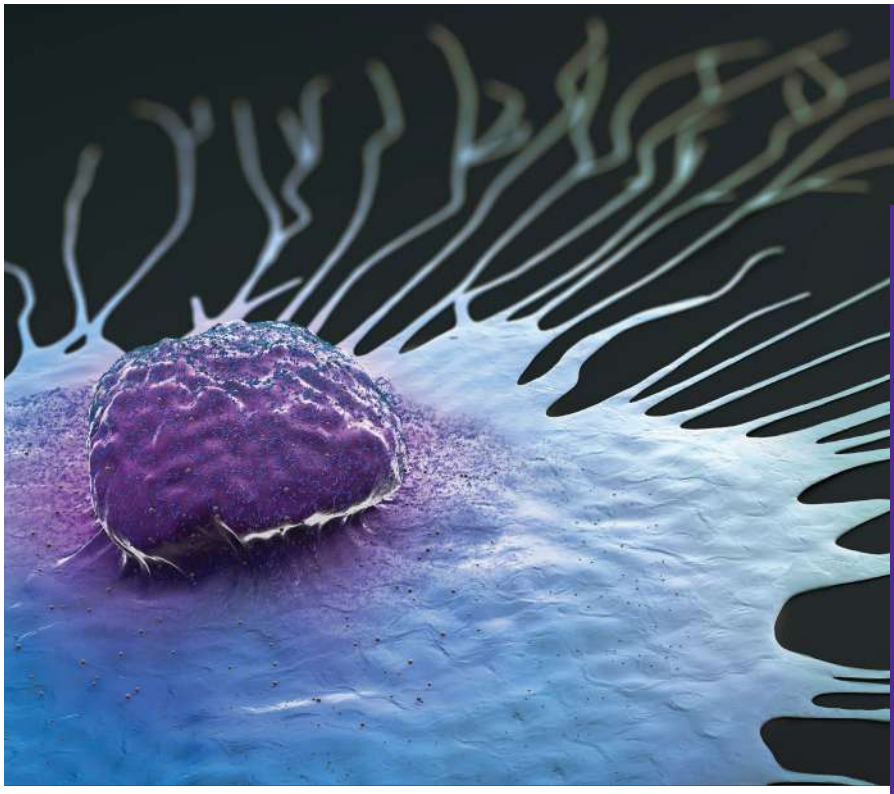

APPLICATION NOTE

AlphaLISA and HTRF Technologies

Author:

Adam Carlson

PerkinElmer, Inc.
Hopkinton, MA

Determination of Cytokines Present in a CAR-T Co-Culture Environment by AlphaLISA and HTRF Technologies

Introduction

Cancer immunotherapy is a treatment option that exploits the body's own immune system to fight against cancer. T-cells protect the human body from infection by pathogens and clear mutant cells through specific recognition by T-cell receptors. Those same T-cells can be genetically modified to contain chimeric antigen receptors (CARs) targeting surface antigens on tumors to help identify and eradicate tumors.[1] CAR design consists of an extracellular domain, typically an scFv from a monoclonal antibody, to recognize the tumor antigen, then a linker or spacer followed by a transmembrane domain (ex CD3ζ) and an intracellular signaling domain that acts in a stimulatory fashion to the T-cell (ex CD28, or 4-1BB). Original CAR-T designs contained only one intracellular signaling domain, later generations contain multiple domains to augment T-cell proliferation and survival and increase cytokine production.[2]

CAR-T therapy involves collection and isolation of a patient's T-cells followed by genetic modification to include a CAR targeting a tumor antigen. The CAR-T cells are then expanded *ex vivo* and re-infused to the patient for treatment. CAR-T cells have been tested in a wide variety of cancer types but have been most effective against hematological malignancies. The FDA has approved anti-CD19 CAR-T therapy for refractory acute lymphocytic leukemia (ALL) and diffuse large B-cell lymphoma (DLBCL).[2,3]

PerkinElmer®
For the Better

T-cells are able to directly trigger apoptosis of cancer cells through granule exocytosis (perforin, granzyme) or death ligand-death receptor (Fas-FasL, TRAIL) systems.[4] Additionally, after binding to the tumor antigen, T-cells become active and release a mixture of Th1 cytokines (e.g. TNFα, IFNγ), pro-inflammatory cytokines (e.g. IL-6, IL-8, IL-12, IL-18, IL-1β), survival cytokines (e.g. IL-2), and granulocyte macrophage colony stimulating factor (GM-CSF).[5] Cytokine secretion results in stromal cell sensitization in the tumor microenvironment.[6] These cytokines and lytic molecules can be detected *in vitro* in co-culture cell-based models by several detection methods including ELISA,[7] MesoScale,[8] AlphaLISA,[9] or HTRF[10] technologies. This application note will focus on detection by two orthogonal no-wash immunoassays: AlphaLISA and HTRF in an *in vitro* co-culture model with CAR-T cells and tumor targeted CD19 positive Raji cells.

Materials and Methods

Reagents and Consumables

- Raji cells (ATCC, #CCL-86)
- RPMI media (ATCC, #30-2001)
- Fetal bovine serum (FBS), heat inactivated (Thermo Fisher, #10082-147)
- CD19 CAR-T cells, CD19scFv-CD28-4-1BB-CD3z (Promab, #PM-CAR1003)
- CAR-T Complete Growth Media (Promab, #PM-CAR2001)
- CellCarrier Spheroid ULA 96-well Microplates (PerkinElmer, #6055330)
- 0.5 mL Eppendorf Tubes (VWR, #89166-278)
- AlphaPlate-384, light gray (PerkinElmer, #6005350)
- Proxiplate-384 plus, shallow well (PerkinElmer, #6008280)
- AlphaLISA kit – IL-8 (PerkinElmer, #AL224C)
- AlphaLISA kit – IFNγ (PerkinElmer, #AL217C)
- AlphaLISA kit – TNFα (PerkinElmer, #AL208C)
- AlphaLISA kit – IL-1β (PerkinElmer, #AL220C)
- AlphaLISA kit – IL-18 (PerkinElmer, #AL241C)
- AlphaLISA kit – IL-2 (PerkinElmer, #AL221C)
- AlphaLISA kit – IL-6 (PerkinElmer, #AL223C)
- AlphaLISA kit – IL-12 (PerkinElmer, #AL3116C)
- AlphaLISA kit – GM-CSF (PerkinElmer, #AL216C)
- HTRF Kit – TNFα (Cisbio, #62HTNFAPEG)
- HTRF Kit – IFNγ (Cisbio, #62HIFNGPEG)
- HTRF Kit - IL-8 (Cisbio, #62HIL08PEG)
- HTRF Kit – GM-CSF (Cisbio, #62HGMCSFPEG)

Assay Technologies

AlphaLISA® is a bead-based immunoassay technology used to study biomolecular interactions in a microplate format. The acronym "Alpha" stands for amplified luminescent proximity homogeneous assay. Some of the key features are that it is a non-radioactive, no-wash, homogeneous proximity assay. Binding of molecules captured on the beads and excitation of the donor leads to an energy transfer from the donor bead to the acceptor bead, ultimately producing a luminescent/fluorescent signal (Figure 1).

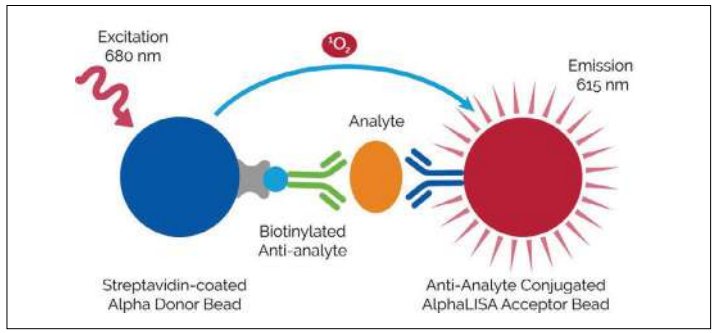

Figure 1. AlphaLISA Assay Principle. A biotinylated anti-analyte antibody is bound by the Streptavidin-coated Alpha Donor beads, while another anti-analyte antibody is conjugated directly to AlphaLISA Acceptor beads. In the presence of analyte, the donor and acceptor beads come into proximity. Excitation of the donor beads at 680 nm provokes the release of singlet oxygen molecules that trigger a cascade of energy transfer in the nearby acceptor beads, resulting in maximum emission at 615 nm. AlphaLISA signal is proportional to the amount of analyte present in the sample.

HTRF® is a TR-FRET based technology and stands for homogeneous time resolved fluorescence. It is based on the fluorescence resonance energy transfer (FRET) between two fluorophores, a donor and an acceptor. These fluorophores can be coupled to antibodies targeting an analyte such that once bound they come in proximity to one another. Excitation of the donor by an energy source (e.g. a flash lamp or a laser) triggers an energy transfer towards the nearby acceptor, which in turn emits specific fluorescence at a given wavelength (Figure 2).

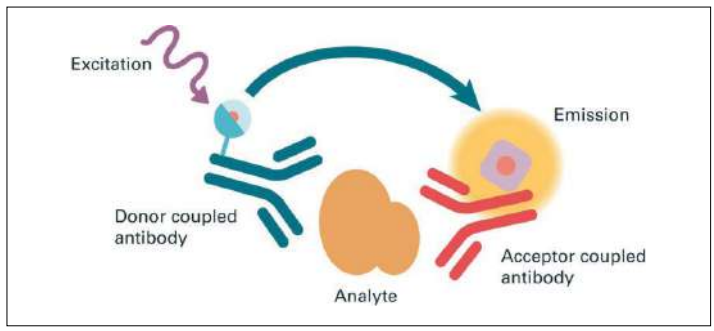

Figure 2. HTRF Assay Principle. When the labelled antibodies bind to the same antigen, the excitation of the donor with a light source (laser or flash lamp) triggers a fluorescence resonance energy transfer (FRET) to the nearby acceptor, which in turn fluoresces at a specific wavelength. The two antibodies bind to the analyte present in the sample, thereby generating FRET. Signal intensity is proportional to the number of antigen-antibody complexes formed and therefore to the analyte concentration.

CAR-T Co-culture Protocol

CAR-T cells were rapidly thawed and allowed to recover overnight in 5 mL of CAR-T media in a T-25 flask before setting up the co-culture assay. Raji cells grown in RPMI media were harvested and counted on the day of the assay. Effector to target cell ratio was set to 10:1 with 100,000 CD-19 CAR-T to 10,000 Raji cells in each well following Promab's experiment design for CAR-T co-culture with their product. Controls included target cells alone and CAR-T cells alone to determine any baseline level of cytokine release from each independent cell population. 100 µL of target or effector cells was added to each appropriate well. Final assay volume was 200 µL and consisted of a 50:50 mixture of RPMI media and Promab's CAR-T media. Separate wells were setup for supernatant collection at 6 hours and 24 hours. Once plated, cell populations were gently mixed then briefly centrifuged to encourage settling as a cell pellet in the U-bottom assay plate to increase cell to cell contact between the two cell types.

Data Collection and Analysis

Cell supernatant was carefully sampled from the assay plate so as not to disturb the cell pellet at 6 and 24 hours post cell plating. Collected supernatant was centrifuged to remove any unwanted cell carryover. Supernatant was split into aliquots in 0.5 mL tubes and kept frozen at -20 °C prior to testing to avoid unwanted freeze thaw cycles.

All AlphaLISA assays were performed following the recommended protocol for each kit. Each assay required 5 µL of sample in a 50 µL reaction in a 384-well AlphaLISA plate. A fresh aliquot for each test condition (target cell alone, CAR-T cell alone, and co-culture well) was thawed on the day of testing. AlphaLISA signal was measured on a PerkinElmer EnVision® 2105 Multimode plate reader using default values for Alpha detection of the fluorescence label. Data was analyzed in GraphPad Prism using non-linear 4 parameter logistic regression for standard curve fitting with $1/Y^2$ weighting.

All HTRF assays were performed following each kit's recommended protocol. Each assay required 16 µL of sample in a 20 µl reaction in a 384-well shallow well Proxiplate. A fresh aliquot for each test condition (target cell alone, CAR-T cell alone, and co-culture well) was thawed on the day of testing. HTRF signal was measured on a PerkinElmer EnVision® 2105 Multimode Plate Reader using HTRF settings. Excitation with laser followed emission at 620 nm (europium donor reference signal) and 665 nm (d2 or XL acceptor signal) was recorded. Data is reported as the HTRF ratio of acceptor to donor signal = (665/620)*10,000. Data was analyzed in GraphPad Prism using non-linear four parameter logistic regression for standard curve fitting with $1/Y^2$ weighting.

Results

Nine cytokine targets, mentioned above, were selected for testing using AlphaLISA technology on the collected supernatants: TNFα, IFNγ, IL-1β, IL-2, IL-6, IL-8, IL-12, IL-18 and GM-CSF. From this set of targets IL-6, IL-12, IL-18 and IL-1β were not detected at levels higher than the calculated lower limit of quantification (LLOQ) under any treatment condition. IL-2 however was determined to be present in the Promab CAR-T media to a high level and therefore additional IL-2 expression in the supernatant could not be accurately determined. Three targets, TNFα, IFNγ and IL-8, were detected in the co-culture supernatant at both 6 h and 24 h (Figure 3) but were not detected in the single cell type control wells (Raji or CD19 CAR-T alone, data not shown) suggesting they are only released from the activated CD19 CAR-T cells in the co-culture condition. GM-CSF had a mild level of release in the non-stimulated CAR-T cells (data not shown) which increased significantly with the co-culture condition (Figure 3).

As an orthogonal assay approach, the four positive targets were tested by HTRF as confirmation of the activity seen in the AlphaLISA assays. Absolute values detected (Figure 4) are not the same as the AlphaLISA values possibly due to different antibodies used for detection in the kits, however the trends over time match (mild accumulation of TNFα at 24 h and much more pronounced increase of IFNγ, IL-8 and GM-CSF) which is shown in Figure 5 as the fold increase in target (pg/mL) over time.

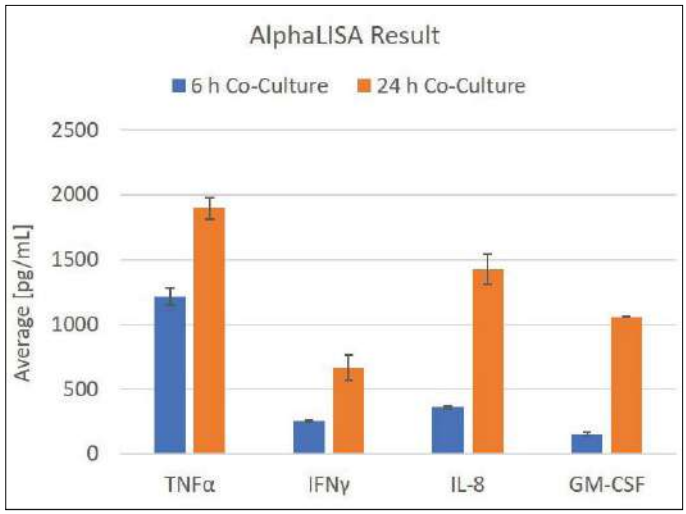

Figure 3. Detection of cytokines by AlphaLISA. Expression level was detected at 6 hs and continued to accumulate in the 24 h time point. Results are shown as average pg/mL in a 5 µL sample as interpolated from the standard curve.

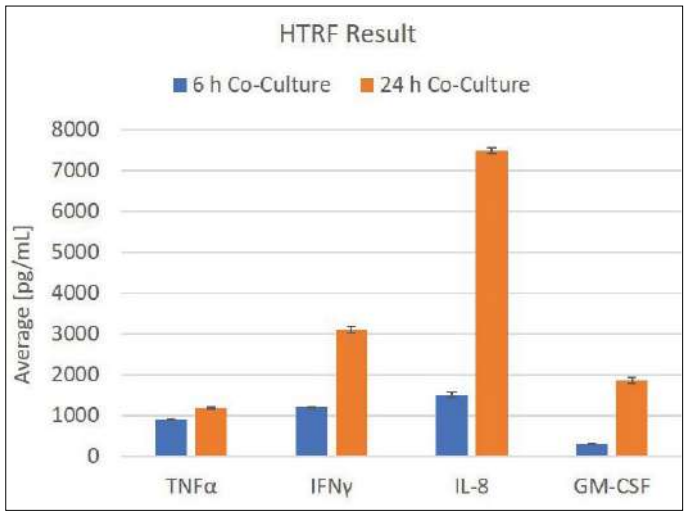

Figure 4. Detection of cytokines by HTRF. Expression level was detected at 6 hs and continued to accumulate in the 24 h time point. Results are shown as average pg/mL in a 16 µL sample as interpolated from the standard curve.

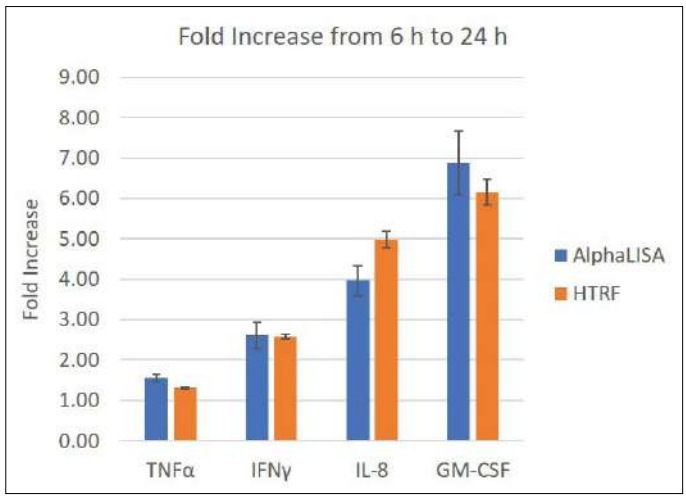

Figure 5. Fold increase in target (pg/mL) over time. 6 h data set to 1.

Summary

In the current application note, we demonstrate an orthogonal approach by using AlphaLISA detection and HTRF to probe the landscape of cytokines and chemokines present in the cell supernatant from a CAR-T/Raji cells co-culture model. Cytokine panning from AlphaLISA yielded four targets (TNFα, IFNγ, IL-8, and GM-CSF) which were elevated in the supernatants of the co-culture wells and confirmed in the HTRF assay with quantitated levels correlating well to each other between the two technologies. Fold increase in the targets over time matched between AlphaLISA and HTRF assays. Both technologies offer rapid, no wash homogeneous detection of cytokines in a 384-well format that is amenable to screening efforts as well as automation, in contrast with a traditional ELISA format also commonly used to detect cytokines.

References

1. Li, D. et al. (2019). Genetically Engineered T cells for Cancer Immunotherapy. Signal Transduction and Targeted Therapy, 4:35
2. Androulla and Lefkothea (2018). CAR T-cell Therapy. A New Era in Cancer Immunotherapy. Current Pharmaceutical Biotechnology, 19 p5-18
3. Tokarew, N. et al. (2018). Teaching and old dog new tricks: next-generation CAR T cells. British Journal of Cancer, 120 p26-37
4. Martinez-Lostao, L. et al. (2015). How do cytotoxic lymphocytes kill cancer cells? Clin. Cancer Res, 21 p5047-5056
5. Xue Q, et al. (2017). Single-cell multiplexed cytokine profiling of CD19 CAR-T cells reveals a diverse landscape of polyfunctional antigen-specific response. Journal of ImmunoTherapy of Cancer. 5:85
6. Benmebarek, MR. et al. (2019). Killing Mechanisms of Chimeric Antigen Receptor (CAR) T Cells. International Journal of Molecular Sciences. 20:1283
7. Castella M. et al. (2019). Development of a Novel Anti-CD19 Chimeric Antigen Receptor: A Paradigm for an Affordable CAR T Cell Production at Academic Institutions. Molecular Therapy: Methods and Clinical Development. 12:134-144
8. Zhang W. et al. (2018). Characterization of clinical grade CD19 chimeric antigen receptor T cells produced using automated CliniMACS Prodigy system. Drug Design, Development and Therapy. 12:3343-356
9. Wang Z. et al. (2020). Galunisertib enhances chimeric antigen receptor-modified T cell function. European Journal of Histochemistry. 64(s2):3122
10. Dextras C. et al (2020). Identification of Small Molecule Enhancers of Immunotherapy for Melanoma. Nature Scientific Reports. 10:5688
11. Hu B. et al. (2017). Augmentation of Antitumor Immunity by Human and Mouse CAR T Cells Secreting IL-18. Cell Reports. 20:13

PerkinElmer, Inc.
940 Winter Street
Waltham, MA 02451 USA
P: (800) 762-4000 or
(+1) 203-925-4602
www.perkinelmer.com

PerkinElmer®

For a complete listing of our global offices, visit www.perkinelmer.com/ContactUs

Copyright ©2020, PerkinElmer, Inc. All rights reserved. PerkinElmer® is a registered trademark of PerkinElmer, Inc. All other trademarks are the property of their respective owners.

146383 PKI

To find out more visit:
https://www.perkinelmer.com/category/biologics

PerkinElmer, Inc.
940 Winter Street
Waltham, MA 02451 USA
P: (800) 762-4000 or
(+1) 203-925-4602
www.perkinelmer.com

PerkinElmer®

For a complete listing of our global offices, visit www.perkinelmer.com/ContactUs

Copyright ©2021, PerkinElmer, Inc. All rights reserved. PerkinElmer® is a registered trademark of PerkinElmer, Inc. All other trademarks are the property of their respective owners.

180515 PKI